DISSERTATION

DEVELOPMENT OF A HYBRID ELECTRIC ORGANIC RANKINE VAPOR COMPRESSION COOLING SYSTEM FOR ENERGY SYSTEM RESILIENCY

Submitted by

Bennett Parker Platt

Department of Mechanical Engineering

In partial fulfillment of the requirements

For the Degree of Doctor of Philosophy

Colorado State University

Fort Collins, Colorado

Summer 2025

Doctoral Committee:

Advisor: Todd M. Bandhauer

Daniel Wise
Jason Quinn
James Cale

ABSTRACT

DEVELOPMENT OF A HYBRID ELECTRIC ORGANIC RANKINE VAPOR COMPRESSION COOLING SYSTEM FOR ENERGY SYSTEM RESILIENCY

Thermally activated chillers, like absorption and organic Rankine vapor compression (ORVC) systems, are solutions to improve efficiency, reduce costs, and meet decarbonization goals in the heating, ventilation, and air-conditioning (HVAC) industry. However, technical limitations prevent these chillers from providing steady cooling power under variable operating conditions. This work presents an extensive investigation of a novel, electrified ORVC system, an innovative approach designed to combine the efficiency and emissions benefits of thermally driven cooling with the on-demand reliability of conventional electric systems. By utilizing both electric and thermally driven compressors in an integrated system, this research addresses the fundamental limitations of purely thermal cooling systems while maximizing the benefits of thermal energy utilization.

A thermodynamic and turbomachinery model was developed to evaluate three distinct compressor configurations across diverse operating scenarios. Simulation results revealed that positioning the thermal compressor before the electric compressor (TC1 configuration) provided optimal performance by mitigating the choking limitations of the electric compressor. This configuration demonstrated exceptional performance flexibility, operating effectively across heat inputs from 100 kW to 327 kW while achieving thermal coefficient of performance (COP) values up to 1.6 and electric COP values reaching 18.2—significantly outperforming both purely thermal (COP_{th} = 0.44) and purely electric (COP_e = 5.86) baseline operations. To validate the simulation

findings, a large-scale prototype test facility was constructed and subjected to extensive experimental evaluation. The experiments confirmed the simulation predictions regarding compressor configuration performance, with only the TC1 arrangement successfully achieving the target 175 kW cooling capacity. Under design conditions, the prototype delivered 176 kW of cooling utilizing 257 kW of thermal input and 20.1 kW of electric input.

Parametric studies examined system response to variations in heat supply (85-110°C), cooling delivery temperature (2-14°C), heat rejection temperature (25-39°C), and electric compressor power (19.2-33.9 kW). These investigations revealed substantial operating flexibility but also identified critical limitations, particularly regarding compressor isentropic efficiency and operating map constraints. Part-load performance evaluation yielded integrated part-load values of 7.40 and 0.56 for electric and thermal COP, respectively, though performance at lower capacities was constrained by electric compressor lift limitations.

This research demonstrates that hybrid ORVC technology can successfully expand the operational flexibility of cooling systems while maintaining high efficiency across diverse conditions. The findings highlight the critical importance of properly matched compression equipment and identify compressor efficiency as a fundamental determinant of both system performance and operational range. These insights provide a foundation for further research and development surrounding hybrid ORVC technology that can contribute to more cost-effective and sustainable cooling solutions.

ACKNOWLEDGMENTS

As my time as a graduate student at CSU draws to close, I would like to acknowledge that I would not be where I am today without the support of the many amazing people that are a part of my life. I feel truly lucky to have crossed paths with each of you and I'd like to thank you all for the various parts you played in my journey through graduate school.

I'd like to begin by thanking Dr. Todd Bandhauer for his guidance over the past 5+ years. Dr. Bandhauer gave me an opportunity as an undergraduate student to get involved with research in a field that I am very passionate about and has challenged me to turn that passion into real results. Throughout my time as a PhD student, Dr. Bandhauer's guidance has helped me develop the skills and initiative necessary to translate curiosity and good ideas into real impact. These are skills I will value for the rest of my life. I'd also like to thank Derek Young for his massive role in my graduate education. As the lead research scientist on CSU's ORVC research projects, Derek has been my first point of contact for anything relating to my research since before I even began graduate school. From helping me uninstall a broken 800lb pump for the 5th time to reading pages and pages of my bad writing in first drafts of research papers, Derek has been in my corner every step of the way.

In relation to this research effort, there are a couple key parties to thank. First, this research was made possible with support from the U.S. Navy's Naval Air Warfare Center Aircraft Division under contract N68335-20-C-0630. I'd also like to thank project partners John Simon and Mike Cushman at Mantel Technologies. Their support with project administration, design, analysis, and equipment made this research possible.

I'd also like to thank all of the friends and coworkers that I've met through the lab for making graduate school a truly positive experience: Taylor Stoll, thanks for all of your support on TCCS work over the years – I would not have been able complete this work without your help building and troubleshooting the test facility, running experiments, and talking through challenges. Also, thanks for being a good friend outside of the lab – your powder skiing skills, dance moves, and amazing art have made my time in the lab that much better. Bella Amyx, thank you for helping me run the endless and sometimes stressful experiments that make up a large part of this dissertation. Thanks for being a friendly ear when I came to bother you in the basement and thanks for always being down for an outdoor adventure – hopefully there are many more. Fred Schmid, thanks for all the chairlift beers, marketplace links, and general shenanigans – the last few years would have been far less entertaining without you sitting a few chairs away. Maddy Seigel, thanks for showing me what it actually means to be a good skier and thanks for always being down for a bike ride, game of pool, or trip to the mountains. Victor Reyes Flores, thanks for bringing your passion and humor to the powerhouse everyday – you helped to bring some much-appreciated energy to the lab. Katie Plese, thank you for the friendship over the past 5+ years. All of the ski trips, train adventures, and general fun have helped make the past few years pretty special. Brandi Grauberger and Caleb Anderson, thanks for being a friend to me from the very beginning – being able to chat with you both about the challenges of being a PhD student helped me push through some of the more challenging times in the last five years.

I'd also like to thank some friends that I connected with from outside of the lab. John Flynn, thank you for being an amazing friend for the past five years and for being in this program for the long haul with me. Your bagels, garage nights, and level-headed perspective on life have helped me through this program. Dylan Giardina, thanks for bringing your humor, spades skills, and the

lichen rock into my life. Ethan Markey, thanks for being one of the most fun guys I know and always being down to get rowdy on a bike, a pair of skis, or a river raft. Danielle Bartholet, thank you for being a steadfast friend that has kept my life a little more fun since the very beginning of my time as a researcher. Robi Vercellino, thank you for being a truly kindhearted friend and for all of the pasta Mondays and mountain adventures over the years. Brye Windell, thanks for being a great friend all of these years. The river trips, PBLs, and general rowdiness that you have brought into my life have made grad school that much better. Abe Dearden, thanks for the countless mountain adventures, garage beers, song recommendations, bike rides, detailed maps, and weather reports. Your general stoke for life has made the past five years that much better. You are all a special group of people and the best friends anyone could ask for. I would not have been able to do this without your support over the years.

Finally, I'd like to thank my parents for all of their support every step of the way. Mom and Dad, thank you for supporting all of my efforts from day one. I truly could not have done this without you. I hope I can use everything that you have given me to help make the world a better place.

TABLE OF CONTENTS

LIST OF TABLES

LIST OF FIGURES

NOMENCLATURE

Nomenclature

AHRI	Air-Conditioning, Heating and Refrigeration Institute
COP	Coefficient of performance
EC	Electric compressor
EC1	Series compressor configuration (electric compressor as stage 1)
HFO	Hydrofluoroolefin
HVAC	Heating, ventilation, and air-conditioning
HX	Heat exchanger
IPLV	Integrated part-load value
ORC	Organic Rankine cycle
ORVC	Organic Rankine vapor-compression cycle
PC	Parallel compressor configuration
SC	Subcooled liquid region
SH	Superheated vapor region
SP	Single-phase region
TC	Turbocompressor
TC1	Series compressor configuration (turbocompressor as stage 1)
TDC	Thermally-driven chiller
TP	Two-phase region
VCC	Vapor-compression cycle

Variables

C	Heat capacity rate [kW K^{-1}]
COP	Coefficient of performance [-]
c_p	Specific heat capacity [kJ kg^{-1} K^{-1}]
ε	Heat exchanger effectiveness [-]
ϵ	Specific heat correction factor [-]
g_c	Gravitational constant [m s^{-2}]
γ	Ratio of specific heats [-]
i	Enthalpy [kJ kg^{-1}]
$\dot{m}$	Mass flowrate [kg s^{-1}]
η	Efficiency [-]
PR	Pressure ratio [-]
θ	Velocity correction factor [-]
$\dot{Q}$	Rate of heat transfer [kW]
R	Specific gas constant [J kg^{-1} K^{-1}]
V	Velocity [m s^{-1}]
$\dot{W}$	Rate of work transfer [kW]
Z	Compressibility factor [-]

Subscripts

a	Actual
boil	Boiler
comp	Compressor
cr	Critical
e	Electric
ec	Electric compressor
eg	Ethylene Glycol
eq	Equivalent
evap	Evaporator
ext	External
i	Inlet
min	Minimum
mech	Mechanical
o	Outlet
pg	Propylene Glycol
pump	Pump
r	Refrigerant
ref	Reference
s	Isentropic property
th	Thermal
turb	Turbine

CHAPTER 1. Introduction

1.1. Climate Change and Global Cooling Demand

The efficiency of current air conditioning technology will make it impossible to meet the goals of the Paris Agreement unless transformative technologies are developed [1]. Advanced, efficient cooling technologies must be developed to meet these goals and avoid catastrophic outcomes from irreversible climate change.

The demand for global cooling is growing rapidly, primarily because of increasing worldwide development and a warming climate. The International Energy Agency (IEA) predicts that cooling energy use will more than triple 2016 levels by 2050 [2]. Although this growth is ubiquitous across the globe, much of this growth comes from the proliferation of air conditioning in large nations with warm climates. According to IEA projections, energy for space cooling will be the fastest-growing use of energy in buildings, responsible for 37% of the total increase in worldwide energy demand for the building sector. These metrics are all based on IEA's baseline, business-as-usual, scenario. However, the agency also developed a projection that assumes a transition to efficient cooling technology based on much tighter minimum energy performance standards. The efficient cooling scenario estimates that the growth in global cooling energy demand between 2016 and 2050 can be dramatically reduced with the effective utilization of more efficient technology. The baseline scenario projects growth from about 2000 TWh in 2016 to over 6000 TWh consumed for cooling in 2050. The efficient cooling scenario keeps consumption in 2050 below 3500 TWh. This represents 75% growth compared to the 200% growth projected in the baseline scenario.

It is estimated that cooling was responsible for over 12% of the total emissions from buildings, nearly 700 million metric tons of CO2 equivalent emissions, in 2016 [2,3]. This comes from direct refrigerant emissions and indirect greenhouse gas emissions associated with electricity consumption in cooling systems. Indirect emissions from power generation make up 74% of these emissions, while the remaining 26% are direct emissions associated with leaks of the working refrigerants. Both categories are significant, highlighting the need to consider both efficiency improvements as well as transitioning to low-impact refrigerants. Direct emissions from refrigerants have a disproportionately high climate impact on a mass basis. Common refrigerants, such as R410a, can have global warming impacts over 2,000 times higher than carbon dioxide [4]. The high impact of these refrigerants has attracted the attention of the international community, with the United Nations choosing to phase out their use in favor of low-impact refrigerants [5].

Inefficient cooling also poses a significant economic cost. Most of the life cycle cost associated with cooling technology is attributed to the energy costs of running the system [3]. Air conditioning is the largest end-use of electricity in residential buildings in the U.S., according to the EIA [6,7]. As such, efficiency improvements can yield significant economic benefits in the form of reduced energy costs. Lawrence Berkeley National Lab highlights that pursuing high energy efficiency in concert with the transition to modern, low-impact refrigerants can deliver the greatest cost savings and emissions reduction [8].

1.2. Thermally Driven Chillers

An alternative cooling technology that can improve cooling system efficiency and utilize low-impact refrigerants is thermally driven chillers or TDCs. These chillers absorb thermal energy and transform it into useful cooling power. Unlike traditional cooling technologies, these systems do not consume significant amounts of electrical energy. Thermally driven chillers can be

especially beneficial when used in applications with waste heat recovery or combined heat and power.

Waste heat is a largely underutilized energy resource. As shown in Figure 1-1, over 65% of the energy produced in the U.S. ends up as rejected energy and does not provide useful energy services [9]. Much of this rejected energy is in the form of relatively low-temperature waste heat, which is traditionally challenging to utilize efficiently and economically. This waste heat often takes the form of hot engine coolant or exhaust gasses. A significant portion of this comes from electricity generation, which is typically less than 40% efficient [10,11]. Waste heat can be recovered and reused in industrial processes or captured and utilized to produce electricity [12]. These strategies enable cost savings and emissions reductions by generating electricity or reducing fuel demand, which are promising methods to meet decarbonization goals [13]. Waste heat can also be utilized to drive a thermally driven chiller and provide cooling without additional electricity consumption.

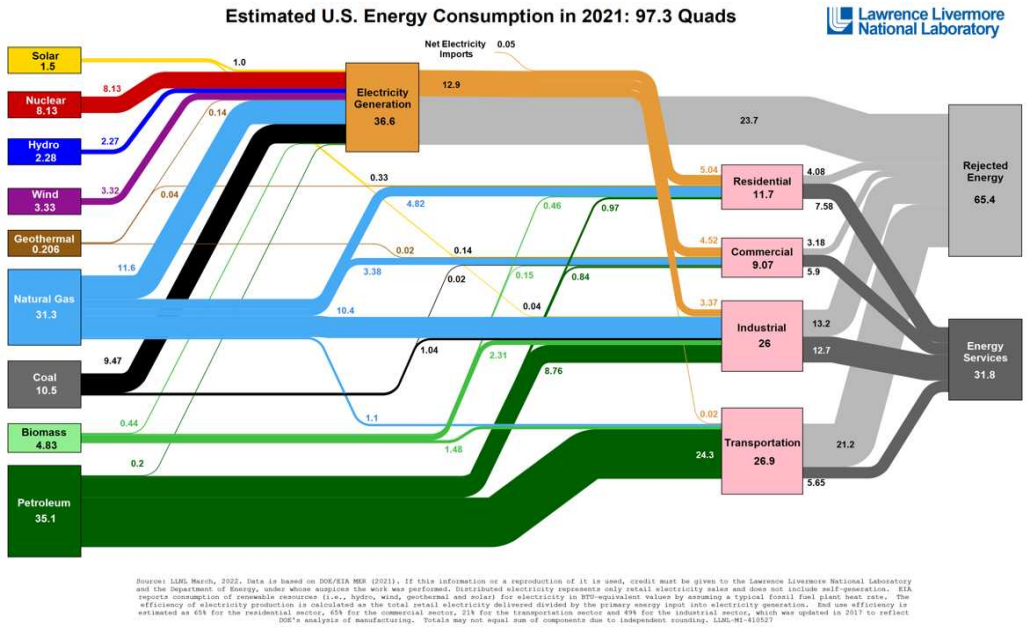

Figure 1-1: U.S energy consumption flowchart for 2021. Over 65% of produced energy is rejected, much of it as waste heat. Waste heat can be utilized in thermally driven chillers. Sourced from [9].

Another potential application for thermally driven chillers is alongside combined heat and power (or CHP) systems. CHP co-locates electricity production and heat generation, allowing these energy outputs to be sourced from the same fuel. This enables system efficiencies significantly higher than those achieved by traditional heat and power systems [14]. Figure 1-2 provides an illustration of how CHP systems work and describes their benefits. CHP systems can realize system efficiency improvements from around 40% to upwards of 90% [15].

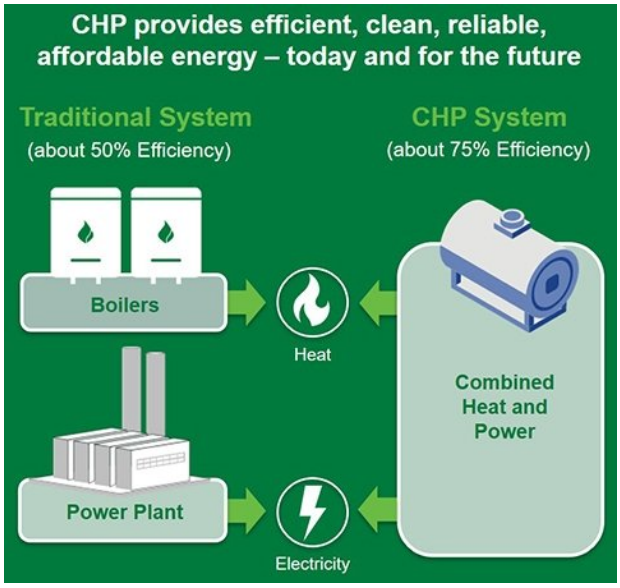

Figure 1-2: CHP offers significantly improved efficiency over traditional energy systems. Pairing thermally driven chillers with CHP systems can improve CHP utilization and efficiency. Sourced from [16].

Thermally driven chillers work with combined heat and power systems by enabling the production of useful cooling power from the system as well. The chiller can absorb thermal energy from the CHP unit to meet cooling demands. This becomes especially useful in warmer seasons when CHP heat is often underutilized. Converting this excess heat to cooling power offers an opportunity to improve CHP system utilization and efficiently meet summer cooling demands.

While both CHP and waste heat recovery offer promising applications for thermally driven chillers, adoption of the technology has been slow. In the United States, there is over 80 GW of

installed combined heat and power. Currently, only about 10% of those CHP systems are paired with a thermally activated chiller [16]. This data shows that this application opportunity for thermally activated chillers is currently not being realized. This indicates that there are shortcomings that are inhibiting the widespread adoption of the technology despite its potential.

1.3. Absorption Chillers

Absorption chillers are the most developed and only commercially available thermally driven cooling technology currently on the market [17]. These chillers utilize specialized sorption agent–refrigerant solutions to deliver useful cooling. These systems consist of four main components: an absorber, a generator, a condenser, and an evaporator. A concentrated absorbing solution absorbs refrigerant vapor in the absorber. The diluted solution travels to the generator where supplied heat desorbs the refrigerant vapor. This vapor moves to the condenser while the concentrated absorbing solution returns to the absorber. After refrigerant vapor is condensed, it is throttled to an evaporator. The evaporating refrigerant provides the desired cooling effect.

The efficiency of these chillers (and all other chillers) is often measured using the coefficient of performance, or COP. COP is defined in Equation (1-1):

$$COP = \frac{\dot{Q}_{\text{cool}}}{\dot{E}_{\text{in}}} \tag{1-1}$$

Q_{cool} is the produced cooling power, in kW, and $\dot{E}_{\text{in}}$ is the input power, in kW. In this work, COP can be COP_{th} where $\dot{E}_{\text{in}}$ is the thermal input, or COP_{elec} where $\dot{E}_{\text{in}}$ is the electrical input.

Absorption chillers primarily utilize either Lithium-bromide (LiBr) or water as the sorption agent and water or ammonia as the refrigerant. LiBr-water absorption chillers are typically able to deliver chilled water at 7°C from heat at about 95°C with a COP_{th} of 0.7 to 0.8 [17]. However,

these systems struggle with crystallization under certain operating conditions which leads to heat exchanger fouling and reduced performance [18]. These systems also require operation at vacuum pressures which adds cost and complexity. [19] Water-ammonia absorption chillers offer similar performance without crystallization concerns or vacuum operation [20]. However, they rely on ammonia as a working fluid, which is a highly toxic fluid and can be a concern for many applications. Absorption chillers can also be very capitally expensive with installed costs reaching $1700/kW [21]. In comparison, electric centrifugal chillers can be installed for as little as $135/kW [22]. Absorption chillers also tend to be quite large, having much larger footprints compared to traditional chillers. Due to these high costs and operational concerns, absorption chillers have not seen significant market penetration in the United States [16].

1.4. Organic Rankine Vapor Compression Chillers

Another thermally activated chiller technology is the organic Rankine vapor compression (ORVC) system. ORVC chillers consist of an organic Rankine cycle (ORC) that is mechanically coupled to a vapor compression cycle (VCC). The mechanical work produced by the ORC is used to drive the compressor in the VCC. In the ORC (also referred to as the power cycle in this work), low-grade heat evaporates an organic working refrigerant in a boiling heat exchanger. This high-pressure refrigerant vapor is then expanded in a turbine, producing mechanical work. The vapor is then condensed, rejecting heat at a lower temperature. The liquid refrigerant is pressurized by a pump, returning it to the boiler pressure. The mechanical work from the turbine is used in a compressor to pressurize low-pressure refrigerant vapor in the VCC (or cooling cycle in this work). The high-pressure vapor is then condensed, rejecting heat. The high-pressure liquid is then expanded and evaporated, generating a cooling effect. The low-pressure vapor then returns to the compressor to complete the cycle.

ORVC technology offers a few unique benefits. Flexibility in working fluid selection is a key advantage of ORVC technology. This flexibility allows the working fluid to be optimized for the application and avoids working fluid challenges like those discussed with absorption technology [23]. ORVC systems are relatively flexible with heat input, accepting driving temperatures well below 100°C. This allows the system to operate even when there is only very low-temperature heat available, helping to boost overall system performance. The technology also offers efficiencies approaching those of commercial absorption chillers while being more cost-effective [24]. ORVC systems also offer a footprint advantage over absorption systems. ORVC systems have been shown to have similar footprint requirements as conventional electric chillers, which at the designed capacity of 264 kW, is approximately 7.9 m^3 [25]. A similar capacity, commercially available, absorption system would require 11.2 m^3 of space [26].

The focus of this work is a variant of ORVC technology that has been in development at Colorado State University since 2015 [27–31]. This variant adds a few improvements over other forms of ORVC technology. A custom turbomachine integrates the turbine and compressor into one device with a common shaft. Three modes of heat recuperation are also included in the technology. A power cycle recuperator preheats fluid entering the boiler with excess heat from the turbine discharge. A suction line heat exchanger (SLHX) adds heat to the compressor suction from residual heat in the discharge of the cooling cycle condenser. Finally, a cross-cycle economizer preheats fluid entering the power cycle boiler with additional sensible heat from the cooling cycle compressor discharge. The recuperative heat exchangers and the waste heat boilers are compact, high-effectiveness, aluminum-brazed plate heat exchangers. The custom turbomachine and heat recuperation give this system favorable performance over other forms of ORVC technology

[30,31]. A process flow diagram of the technology can be seen in Figure 1-3 and the technologies unique to the system can be seen in Figure 1-4.

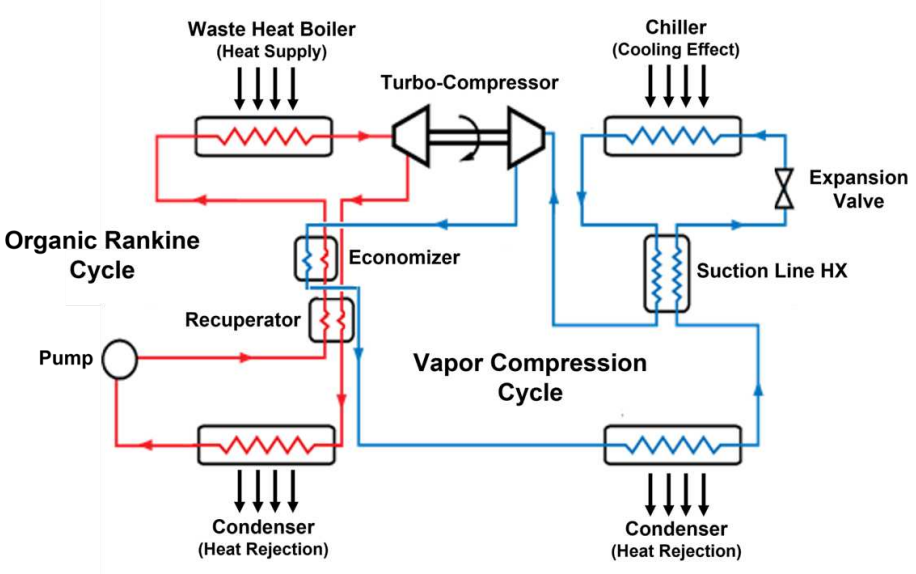

Figure 1-3: Process flow diagram of Colorado State University's ORVC technology. The power cycle, in red, absorbs thermal energy and produces mechanical work in the turbine. The cooling cycle, in blue, consumes the mechanical work in the compressor and generates a cooling effect.

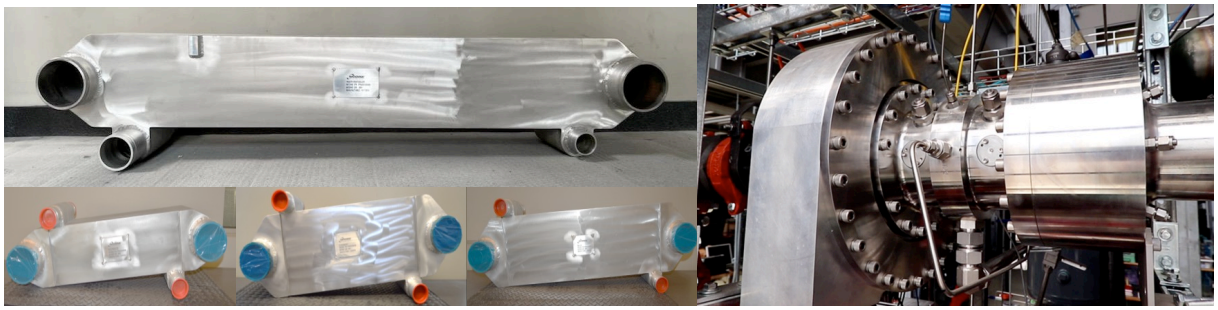

Figure 1-4: Custom fabricated heat exchangers and turbomachinery utilized in the ORVC system. Highly effective heat exchange and efficient turbomachinery help to give the technology uniquely high performance.

Despite the advantages of this system, and thermally driven chillers in general, there are drawbacks associated with the systems. One key issue is the inconsistent cooling output when the heat supply varies [30,32]. Since TDCs are driven solely by thermal input, if the amount of heat input fluctuates, the cooling performance of the system also necessarily fluctuates. This leads to challenges in utilizing thermal cooling systems as the technology is often unable to deliver

consistent cooling power [30,33–35]. Additionally, as boundary or ambient temperatures change, the operating efficiency of the system also changes. Therefore, without a dispatchable energy source, cooling duty is necessarily impacted as boundary temperatures change. This effect can limit the technology in applications that operate in variable ambient conditions. Both limitations have hindered the development and adoption of thermally activated cooling technologies [16].

A recently proposed modified ORVC concept addresses the limitations of thermally driven chillers by integrating an electric input pathway into the cooling cycle [36–38]. This hybrid ORVC allows the system to operate on heat, electricity, or a combination of both, effectively managing the challenges of variable operating conditions. For instance, adjustments in electric input can compensate for fluctuations in condenser or heat supply temperatures, ensuring steady cooling delivery. Similarly, variations in available heat can be balanced by varying the electric input, enabling consistent system cooling capacity. As a result, the hybrid ORVC concept can deliver stable cooling performance under diverse conditions. This eliminates the need for redundant equipment, improves system economics, and enhances the technology's commercial viability.

Prior to this research effort, the hybrid ORVC concept has seen very little investigation. This work will greatly expand the body of research on the topic and develop critical understandings that will enable further development and adoption of the technology. Specifically, this study will:

- Present a new configuration of the hybrid ORVC concept.
- Develop a new simulation methodology to evaluate the operation and performance of a hybrid ORVC system.
- Model the system across a range of relevant operating conditions and compressor configurations to determine the optimal system configuration and predict performance.

- Design and fabricate an industrial scale test facility to experimentally evaluate system performance at a scale relevant to real-world applications.
- Experimentally evaluate three compressor configurations and demonstrate the performance of the system.
- Characterize cooling performance across a range of off-design operating conditions to understand the benefits of the hybrid configuration.

1.5. Thesis Organization

The following chapters present the individual research activities that were undertaken to further the understanding of hybrid ORVC technology in this work. Chapter 2 provides a discussion of previous literature relevant to the hybrid ORVC concept. The literature review will discuss studies that have characterized the limitations of traditional thermally activated cooling technologies and provide a review of the limited experimental studies that have evaluated ORVC technology. A review of the literature surrounding the hybrid ORVC concept is also presented. Chapter 3 details the development of the test facility that is central to this work. Specific configuration details are presented, hardware components are discussed, and data acquisition methods are provided. Chapter 4 focuses on the simulation activities performed as a part of this work. Simulation methodology is developed and simulated performance results are presented for design and off-design operating conditions. The implications of the simulation results on the performance experiments are also discussed. Chapter 5 presents the performance experiments conducted at design point operating conditions. Experimental evaluation of three compressor configurations is also discussed in Chapter 5. Chapter 6 details the results of experiments performed on the test facility at off-design operating conditions. Finally, Chapter 7 synthesizes core findings and provides recommendations for further work.

CHAPTER 2. Literature Review

As demand for cooling increases globally and greater emphasis is placed on energy efficiency in the face of climate change, demand for alternative cooling technologies has increased significantly. Thermally driven cooling technologies offer a promising alternative to traditional cooling technology. These technologies utilize thermal energy to provide cooling power without consuming significant amounts of electricity. Reduced reliance on electricity and improved cooling system efficiency are key benefits of these systems. Thermally driven chillers can also utilize available waste heat to further improve the efficiency and emission reduction benefits of the technology.

Absorption chillers are the most developed and only commercially available thermally driven cooling technology currently on the market [17]. Challenges associated with LiBr-water and ammonia-based absorption chillers are well-documented in literature and industry: poor tolerance for variable operating conditions, low/vacuum working pressures, high cost due to corrosive working fluids or exotic heat exchanger alloys, large footprint requirements, and poisonous/toxic working fluids [18–22]. Due to these concerns, absorption chillers have not seen significant market penetration in the United States [16]. Organic Rankine vapor compression systems are an alternative thermally driven cooling technology that offers a few critical benefits over absorption chillers while achieving similar levels of efficiency. Critically, ORVC systems offer working fluid flexibility, reduced costs, low toxicity, and smaller footprint requirements.

Despite the advantages of ORVC technology over other thermally driven chillers, a few challenges remain that limit the applicability and impact of the technology. Namely, ORVC systems, like all other thermally driven chillers, struggle to provide consistent cooling performance

when operating with variable levels of heat input or changing boundary temperatures. A hybrid thermal-electric ORVC concept presents a solution by enabling on-demand electric input to balance operational variability and deliver consistent cooling power. The following sections provide an in-depth survey of literature relevant to the novel hybrid ORVC chiller concept. A review of experimental studies on ORVC technology is presented to establish the status of the experimental development of the technology. This is followed by a discussion of studies detailing the challenges of operating TDCs under variable conditions. Finally, a detailed discussion of the existing research efforts surrounding the hybrid ORVC concept is presented. The specific aims of this work are discussed within the context of the gaps in this existing literature.

2.1. Experimental ORVC Development

Research on ORVC systems has been limited, especially experimental studies. Development began with a focus on solar-powered heating and cooling of buildings. Thermal energy from solar collectors was used as the driving energy for these early studies. More recently, waste heat applications have been the focus of experimental ORVC research, with industrial waste heat streams being used to drive the technology.

Prigmore and Barber provided one of the first demonstrations of the technology for an air conditioning application in 1975. They utilized a radial expander coupled to a piston compressor via a belt and gearbox system. This system used R12 and R113 and included a power cycle recuperator. The system cooling output was slightly above 10 kW and the system achieved an electric COP of 7.43 at design point operating conditions. While target performance was not achieved, their work shows the feasibility of coupling the two cycles together and underscores the benefits of a power cycle recuperator, which is utilized in the present work [39]. This study also

aligns with the trends discussed in Section 2.1, with decreased performance and capacity as heat supply temperature was reduced. This trend is shown in Figure 2-1.

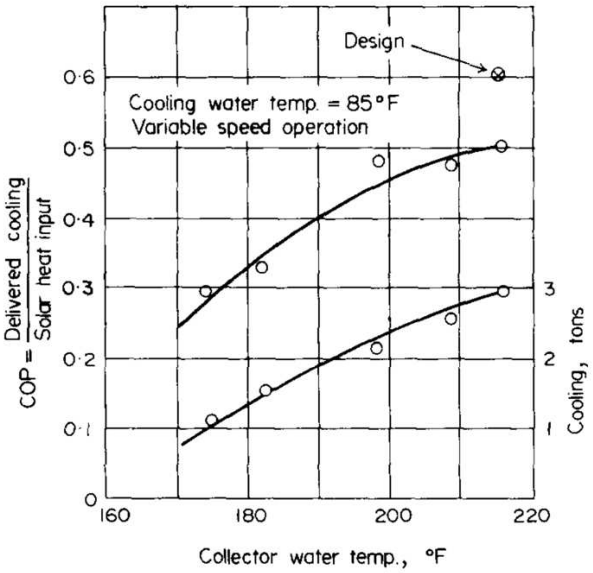

Figure 2-1: Early prototype capacity and performance across a range of heat input temperatures. From [39].

Demierre et al. provided another experimental evaluation of ORVC technology [40] using an ORVC system as a thermally driven heat pump. Their prototype system was configured to deliver a larger capacity of about 40 kW and was one of the earlier instances of a radial turbine being directly coupled to a centrifugal compressor for an ORVC system. Their design utilized gas bearings to enable oil-free operation of the system. This study was an early validation of directly coupled radial turbomachinery for application in an ORVC system. Directly coupled, oil-free, radial turbomachinery designs have been adopted for many subsequent studies including the present research. Figure 2-2 shows the radial turbine used by Demierre et al.

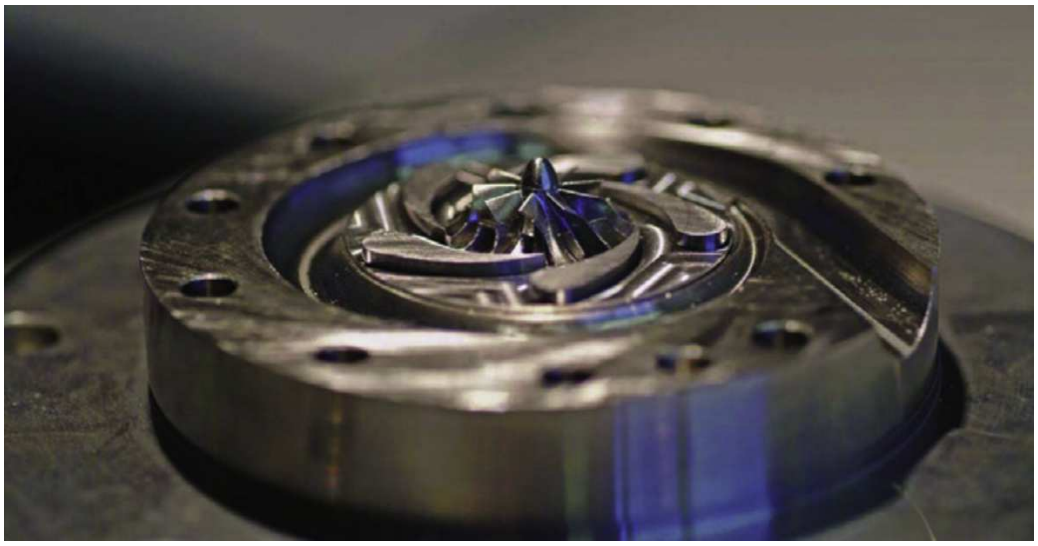

Figure 2-2: Example of a radial turbine that has been proven to be effective in ORVC applications. From [40].

The application of ORVC technology for waste heat recovery was investigated by Liang et al. [41]. They demonstrated the potential of waste heat with ORVC using a prototype designed for mobile applications. The system could deliver cooling at refrigeration temperatures from engine coolant waste heat. When operating at design point conditions, the prototype operated with a cooling capacity of 1.8 kW. While the scale of the system was small, it effectively demonstrated the feasibility of the concept in an engine coolant waste heat application.

Biancardi et al. developed an early prototype, designed to function as a solar-powered heat pump or chiller [42]. This system served as an early validation of ORVC technology on a larger scale by generating 63 kW of cooling at 7^{o}C, utilizing a radial turbine directly coupled to a centrifugal compressor. Notably, this system achieved a coefficient of performance (COP) of nearly 0.7 at its peak performance. This demonstrated the scalability of the technology and underscored the fact that its performance remained consistent even when scaled up to larger capacities. This study also developed the technology for use as both a heat pump and a chiller as seen in Figure 2-3.

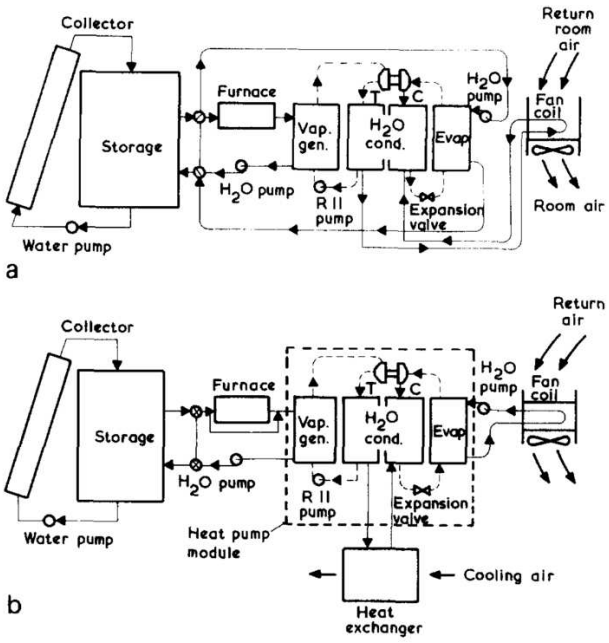

Figure 2-3: Process flow diagram of an ORVC system configured as a heat pump (a) and a chiller (b). From [42].

An experimental study by Garland et al. evaluated an ORVC system for powerplant cooling applications [29]. They developed a large-scale (250 kW) prototype that recovered waste heat from power plant flue gas to provide additional cooling to the plant's cooling water. Variable operating conditions were evaluated but the range was limited due to the air-coupled nature of the prototype. This work demonstrated the potential for achieving very large capacities as well as the benefits of heat recuperation strategies.

Recently, Grauberger et al. completed two experimental studies on a large-scale liquid-coupled ORVC system designed to recover heat from engine coolant [30,31]. Their system incorporated directly coupled radial turbomachinery and three modes of heat recuperation to achieve high efficiency. When delivering chilled water at 7°C with engine coolant at 91°C, the prototype produced 263 kW of cooling with a thermal COP of 0.56. They tested their prototype with variable boiler, condenser, and evaporator temperatures to capture performance trends and operational limits of the system as operating conditions changed.

Table 2-1 presents key aspects of each of the ORVC studies reviewed in this section and highlights similarities with the current research effort. While most of the studies utilized similar temperature heat sources, there is variation in cooling delivery temperature, fluid, turbomachinery, scale, and heat recuperation methods among the existing literature. The works by Grauberger et al. share many commonalities with the current research effort [30,31]. However, the hybrid configuration investigated in this research sets this effort apart from the works by Grauberger et al. as well as the rest of the studies discussed in this section.

Table 2-1: Attributes of the experimental ORVC studies reviewed in this section and their similarities with the current research.

Study	Heat Source	Cooling Delivery	Fluid	Expander/ Compressor	Scale	Heat Recuperation	Hybrid Configuration	Variable Conditions
[39]	100 °C	7.2 °C	R113/ R12	Radial/ Reciprocating	10.5 kW	Recuperator Only	No	Variable Heat Supply Only
[43]	200 °C	~15 °C	R245fa / R134a	Scroll/Scroll	5 kW	Recuperator Only	No	No
[40]	~100 °C	~10 °C	R134a	Radial/ Centrifugal	40 kW	None	No	Yes
[41]	95 °C	-4 °C	R245fa / R134a	Scroll/Scroll	1.8 kW	None	No	No
[42]	93 °C – 149 °C	7 °C	R11	Radial/ Centrifugal	63 kW	None	No	Heat Source Only
[29]	90 °C	30 °C	HFE-7000/ R134a	Radial/ Centrifugal	250 kW	Recuperator Only	No	Yes –Limited Range
[30,31]	91 °C	6.7 °C	R1234 ze(E)	Radial/ Centrifugal	263 kW	Recuperator/SLHX/Economizer	No	Yes
Present	91 °C	6.7 °C	R1234 ze(E)	Radial/ Centrifugal	175 kW	Recuperator/SLHX/Economizer	Yes	Yes

2.2. Limitations of Thermally Driven Chillers

There are limitations of both absorption and ORVC chillers that are hindering further development and adoption of the technology. Primarily, both systems are unable to produce a fixed chilled water duty during operation with variable heat input or variable source/sink temperatures.

The first critical limitation arises when operating a thermally driven chiller with a variable supply of thermal energy, as highlighted by Shirazi et al. who reviewed solar-powered absorption

chiller literature [32]. Due to the intermittent nature of solar energy, solar-driven absorption chillers must be equipped with a backup system to enable steady operation during periods of low solar irradiation. Shirazi et al. discuss how these backup systems are a challenge for this type of technology due to their negative impact on efficiency and significant added equipment cost. A simplified process flow diagram of an absorption unit installed with a backup chiller is shown in Figure 2-4.

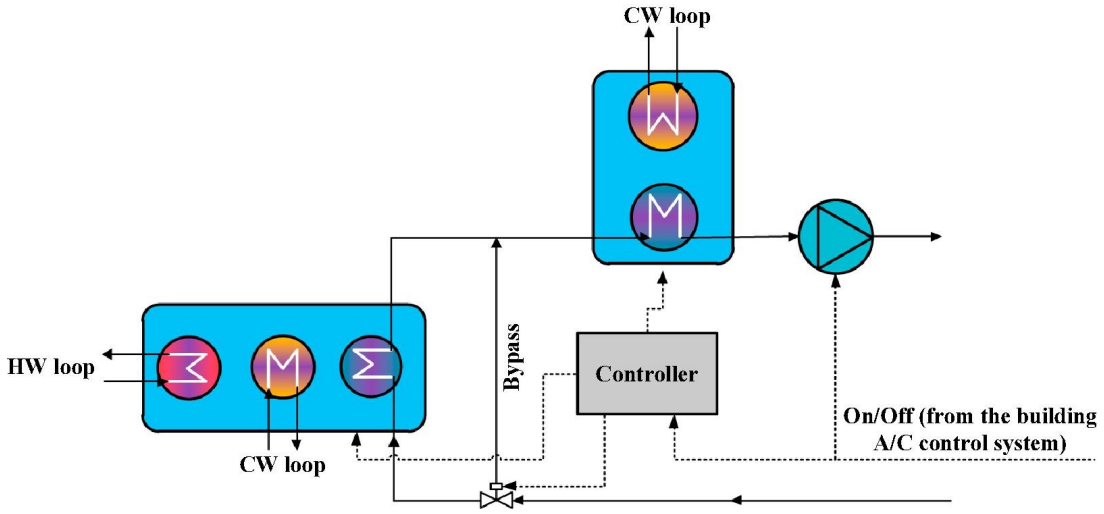

Figure 2-4: A typical configuration of an absorption chiller (left) installed with a backup vapor compression chiller (top). The significant additional capital cost of the backup chiller has proven to be prohibitive for many applications. From [32].

A similar challenge is also identified in ORVC literature. In 2022, Grauberger et al. experimentally evaluated an ORVC system designed for space cooling applications [30]. Their facility was able to deliver 264 kW of cooling when operating at design conditions. However, the amount of chilled water production decreased as heat supply was decreased. This shows that a fixed amount of chilling duty cannot be maintained by an ORVC system while heat input varies. This challenge is limiting further adoption of thermally driven chillers. For many applications, absorption and ORVC systems are unable to meet the application requirements for steady cooling supply, unless paired with electrically driven backup systems.

The second challenge for these technologies, deriving from Carnot limitations on efficiency, is associated with variable operating temperatures that impact all thermally driven cooling technologies. The Carnot maximum theoretical COP for a heat pump is given in Equation 2-1 and the maximum theoretical efficiency of a heat engine is given in Equation 2-2,

$$COP_{\max} = \frac{1}{1 - \frac{T_C}{T_H}} \tag{2-1}$$

$$\eta_{\max} = 1 - \frac{T_C}{T_H} \tag{2-2}$$

where T_C is the temperature of the cold reservoir in Kelvin and T_H is the temperature of the hot reservoir in Kelvin. Given that ORVC technology, and thermally activated chillers as a whole, consist of both a heat engine and a heat pump, it is clear why these technologies are sensitive to changes in reservoir temperature. Boiler temperature, heat rejection temperature (typically linked to ambient temperature), and chilled water delivery temperature all represent reservoir temperatures that have an impact on the efficiency of these systems.

These limitations are discussed by Porumb et al. and Gomri in their evaluations of absorption chillers [33,34]. Porumb et al. investigated the impact of condenser water temperature, chilled water temperature, and generator temperature on the performance of solar absorption chillers. They numerically modeled a solar thermal hot water system coupled to a single effect lithium bromide–water (LiBr) absorption chiller for an HVAC application. They found that the COP of the system decreased with lower chilled water temperature and increased condenser water temperature. The simulations revealed especially high sensitivity to variability in the condenser temperature. Performance impacts associated with cooled water temperature and cooling water temperature on solar-driven absorption systems are shown in Figure 2-5.

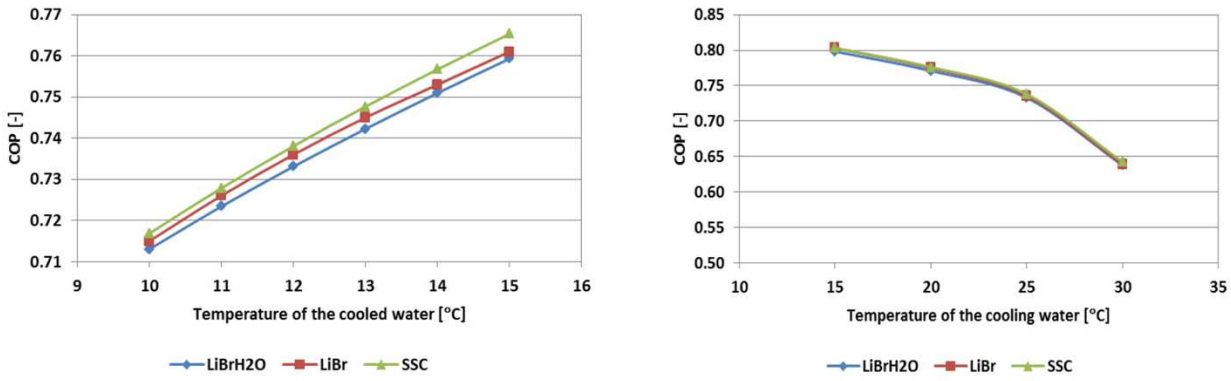

Figure 2-5: Impact of cooled water and cooling water temperature on COP. LiBrH2O, LiBr, and SSC represent alternative fluid property libraries utilized for simulation calculations. From [33].

Gomri evaluated the impact of boundary temperatures on single, double, and triple-effect absorbers [34]. They found a general trend of reduced performance across all three types of absorption systems with decreasing generator (heat input) temperature. Additionally, in a similar result to the Porumb et al. study, Gomri also found a trend of reduced performance with decreasing evaporator temperature. The impact of evaporator temperature became more pronounced in multi-effect systems. The temperature impacts across all three systems are presented in Figure 2-6. Results from both Porumb et al. and Gomri conclusively demonstrate that absorption chillers are unable to provide steady performance when operating under variable conditions.

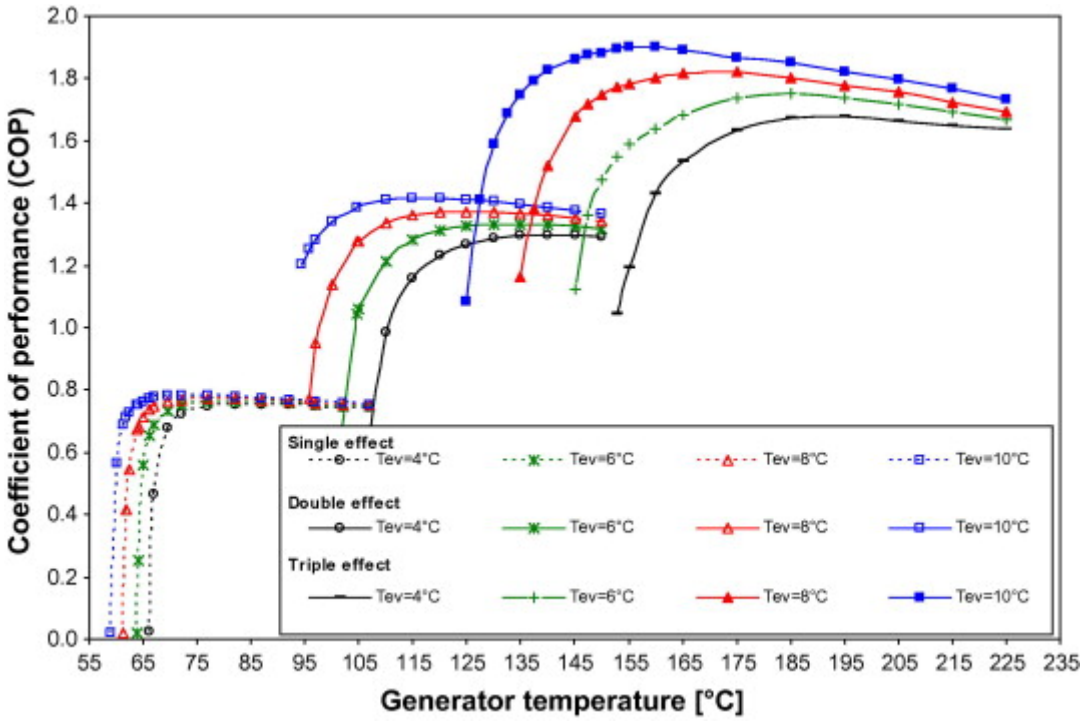

Figure 2-6: Effect of generator and evaporator temperature across single, double, and triple effect absorption systems. From [34].

Similar trends hold true in ORVC literature. Xia et al. developed a multi-layer optimization model for ORVC technology that evaluated various system parameters for thermodynamic, economic, and environmental performance [35]. A selection of 18 potential working fluids was simulated for use in ORVC systems to evaluate system COP across a range of heat supply temperatures. They found that all 18 fluids showed increased COP as heat input temperature increased. Most fluids yielded a COP of between 0.20 and 0.25 when the heat supply temperature was 75°C. The simulated COP for all these fluids increased to between 0.35 and 0.45 when the heat supply temperature was increased to 110°C. This showed that, like absorption chillers, ORVC system performance is variable and linked to changes in heat supply temperature.

Grauberger et al. also investigated the impact of operating temperatures on their experimental ORVC facility [30]. The impact of condenser, heat supply, and chilled water delivery temperature was experimentally quantified. They found that the overall system COP decreased by

about 20% when the condenser temperature was increased by 3°C or when the chilled water delivery temperature was decreased by 3°C. Figure 2-7 presents the COP impacts across the range of chilled water and condenser temperatures evaluated. For heat supply temperature, Grauberger et al. found that the system COP increased with increased temperature, with up to a 10% increase in COP associated with a 30°C increase in heat supply.

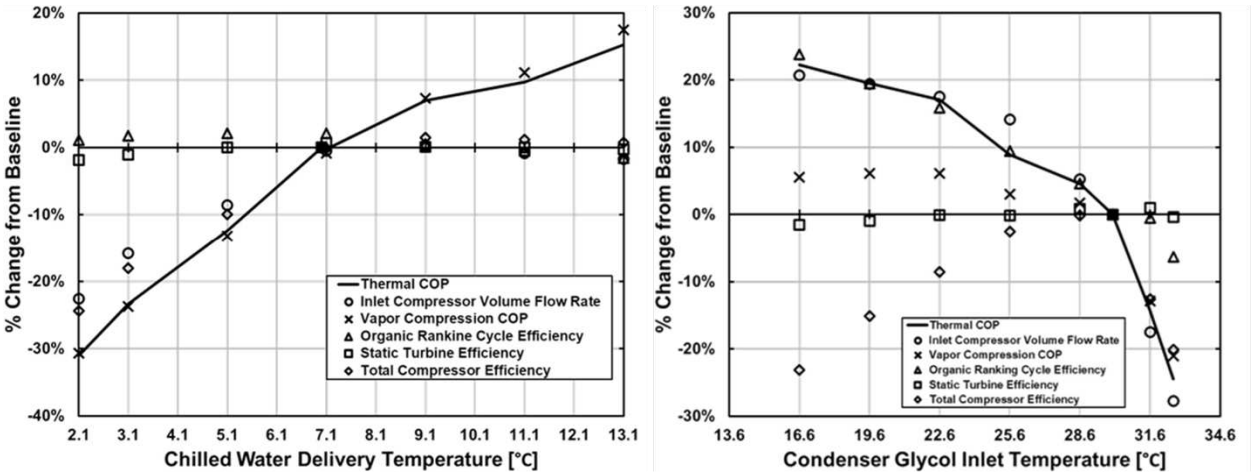

Figure 2-7: Impact of chilled water and condenser temperatures on ORVC system performance. From [30].

In general, this literature shows that variable operating conditions are challenging for absorption and ORVC technology. As these operating conditions change, system performance is impacted, making it challenging for these technologies to deliver a steady supply of cooling power. While traditional vapor-compression chillers suffer from the same performance impacts, the on-demand availability of electricity allows these chillers to overcome this challenge. However, the thermal resources that drive absorption and ORVC technology are typically not dispatchable preventing the required operational flexibility. This can limit the ability of thermally activated chillers to provide a steady chilled water supply and has impacted the adoption and further development of the technologies. The hybrid ORVC configuration offers a potential solution to

these challenges. The novelty of the concept, as well as existing literature on the concept, will be discussed in the next section.

2.3. Hybrid ORVC Technology

As discussed in Section 2.2, the biggest challenge limiting the development and adoption of thermally driven chillers is the inability to overcome capacity or efficiency impacts associated with operating in variable conditions. Recent literature has proposed a variation on ORVC technology as a solution to these challenges. Researchers have presented the concept of integrating a pathway for electric input into the vapor compression cycle of the system. This provides the on-demand benefits of electricity while maintaining the capability to realize the efficiency benefits of ORVC systems. Three studies have investigated the hybrid, electrified version of the ORVC system. Each research effort has taken a different approach and evaluated different aspects of the concept.

Xiao et al. first presented the concept in 2021 [36]. They performed a simulation-based investigation of the concept and applied the results to a case study of an office building in Guangzhou, China. The simulated system was driven by solar heat and integrated a frequency conversion electric motor with the compressor in the vapor compression cycle. In their model, when the cooling duty produced from the solar heat was not sufficient to meet the cooling demand of the building, additional duty was produced from electric input. The required electric work was back-calculated from the computed COP for the cycle. They found that the addition of the electric motor enabled the system to meet the variable cooling demand of the building while adapting to changing levels of solar radiation. The total cooling duty along with the components produced from electric and solar input throughout the simulated day are presented in Figure 2-8. The

simulations resulted in 68% electricity savings for the office building case study when compared with a typical electric chiller system.

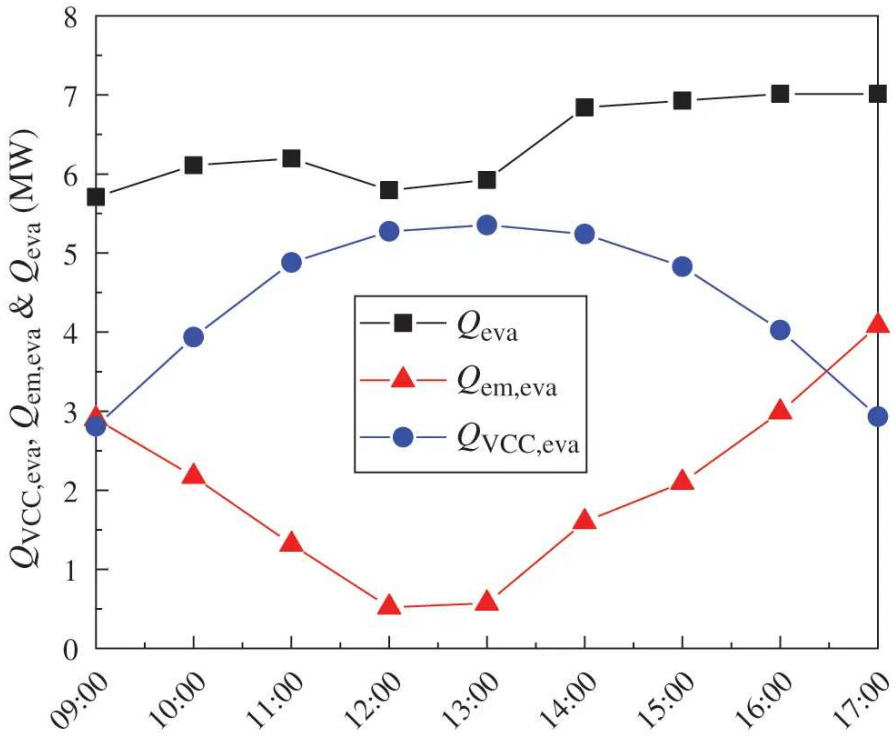

Figure 2-8: Total cooling duty (Q_{eva}) and the fraction supplied by electric ($Q_{\mathrm{em,eva}}$) and solar ($Q_{\mathrm{VCC,eva}}$) input over the simulated day. From [36].

Two experimental research efforts have been performed on the electrified ORVC concept. The first, conducted by Jiang et al., developed an electrified ORVC test facility intended to demonstrate the technology for use in cryogenic air-separation units [37]. The facility was designed to operate with heat supplied at 72°C and produce chilled water at 19°C. The power and cooling cycles were coupled using a combined radial turbine and centrifugal compressor prototype with an integrated motor. The device is shown in Figure 2-9.

Figure 2-9: Prototype expander-compressor with an integrated electric motor. From [37].

The authors found that the facility achieved a COP of 0.63 while delivering 14.2 kW of cooling at design point operating conditions. Throughout the performance test conducted in this study, the electric motor power was held constant at approximately 2.0 kW. Figure 2-10 provides example data from the performance tests with constant motor power. This prevented any evaluation of the influence of electric input on the performance of the system, and therefore the study failed to capture any insights on the benefit of the electrified ORVC configuration. Despite limited scope, the work provided an experimental validation of the hybrid ORVC concept.

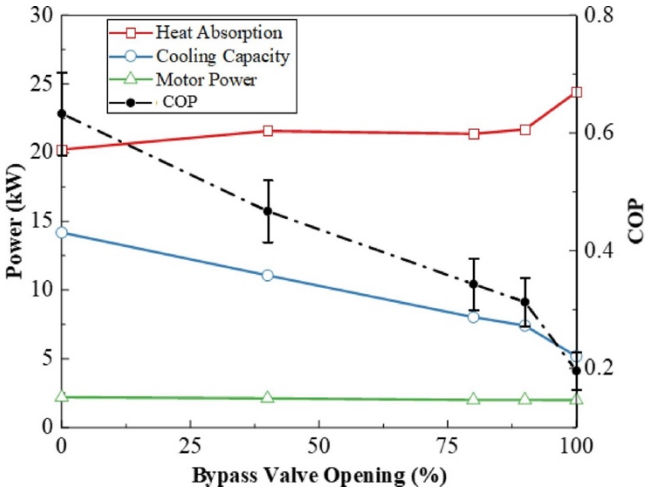

Figure 2-10: Performance data for the hybrid ORVC system across the full range of bypass valve opening conditions presented by Jiang et al. [37]. Motor power (green) was held constant across the range of tests, limiting the scope of the study. From [37].

Zhou et al. performed another experimental study on the same experimental facility designed for air separator applications [38]. Their study was focused on the dynamic response of the system. They investigated off-design point operating conditions and variable electric motor power but only for dynamic response considerations. Step changes in each of the experiments were only held constant for about 100 seconds. The dynamic nature of these tests makes them unreliable for drawing any insights about the performance of the system outside of its dynamic response.

These previous works on electrified ORVC technology have begun to quantify and demonstrate the benefits of the concept. They simulated hybrid ORVC technology at design and off-design conditions for HVAC applications and experimentally evaluated the technology at design conditions and for dynamic response. However, the technology is yet to be experimentally evaluated under steady-state operation across a wide range of conditions. This is a critical gap in the existing literature that has important implications for the development of the technology. Given that operation under variable conditions has been identified as a key limitation of thermally activated cooling technology, developing an understanding of the off-design performance of a hybrid ORVC system is critical. Table 2-2 presents key attributes of the existing hybrid ORVC studies and compares them to the present study. Similarities with the current work are shaded.

Table 2-2: Similarities between hybrid ORVC literature and the current study.

Study	Experimental Study	Off-Design Conditions	Electric Configuration	Heat Source	Cooling Delivery	Heat Rejection	Variable Heat Supply	Scale	Fluid
[36]	No - Simulated Case Study	Yes – Heat Supply Only	Additional Compressor Power	80°C – 140°C	5.0°C	40°C	Yes	7.0 MW	R245fa
[37]	Yes	No	Integrated Motor	71.9°C	19.4°C	30.2°C	No	14.2 kW	R245fa
[38]	Yes	Yes - Dynamic Response Only	Integrated Motor	78°C	20°C	Ambient Air (Temperature Unknown)	Yes – Dynamic Response Only	86.2 kW	R245fa
Present	Yes	Yes	Independent Compressor	85°C – 110°C	2.0°C – 21°C	21°C – 31°C	Yes	175 kW	R1234ze(E)

2.4. Literature Gaps and Specific Aims of this Study

From the literature reviewed in the previous sections, it is clear that scientific investigation into the electrified ORVC concept is just beginning. With only three unique research efforts focused on the hybrid ORVC system, the potential benefits of the technology have been considered but the remaining gaps in literature on the topic are significant. These key research gaps can be summarized as follows:

- Experimental exploration of electrified ORVC for HVAC industry applications has yet to be conducted,
- The effect of electric motor power on the steady-state performance has not been evaluated,
- The capability to adapt to variable heat supply and operating conditions using electric power has not been experimentally tested,
- Steady-state performance at off-design operating conditions has not been assessed,
- Only one electrification configuration—an electric motor integrated into the expander-compressor—has been evaluated. Alternative configurations, such as independent compressors, remain unexplored, and
- The effect of electric input on turbomachinery performance, a key ORVC performance factor, has not been evaluated.

Acknowledging these critical research gaps, the present work seeks to advance understanding of this cooling technology with potential for significant impact. The research presented in the following chapters explores the performance, benefits, and limitations of hybrid electric ORVC technology. The specific aims of the research effort are as follows:

- Present a new configuration of the hybrid ORVC system utilizing independent electric and thermally driven compressors,
- Develop an experimentally based hybrid ORVC model to evaluate compressor configuration options and simulate system performance across a wide range of conditions,
- Design and fabricate a large-scale, fully integrated, hybrid ORVC test facility to enable experimental validation of the technology.
- Experimentally test three new compressor configurations to understand the impact of compressor arrangement on system performance.
- Test the system across a range of heat inputs—from fully thermal to fully electric operation—at AHRI standard operating conditions for HVAC applications.
- Evaluate system performance under off-design conditions to assess performance impacts and operating ranges related to variable heat input, heat rejection, and cooling delivery temperatures.
- Characterize the integrated part-load value (IPLV) of the system to understand the potential of the technology in realistic, part-load HVAC applications.
- Apply turbomachinery analysis to simulation and experimental results to assess the impact of turbomachinery performance, electric input, and compressor arrangement on overall system performance.

The findings of this work will advance the body of research on hybrid ORVC technology. The thorough investigation will pull insights from simulations and experiments across a wide range of conditions and utilize advanced turbomachinery analysis to clarify the potential of the hybrid

ORVC concept as an alternative cooling technology. These insights can be used to further develop the technology and inform future research.

CHAPTER 3. Test Facility Description

This chapter presents a detailed description of the hybrid ORVC experimental facility that was developed for this research. The facility was originally developed by Grauberger et. al for their work on ORVC technology [44]. The test facility has been extensively modified to enable the thorough experimental evaluation of the hybrid ORVC concept. Specific modifications include electric compressor integration, control system improvements, pump health system development, and refrigerant charge optimization. For this chapter, foundational working principles of the ORC and VCC are first discussed to provide necessary background on each cycle. The details of the facility layout are then presented, including a complete system piping and instrumentation diagram. Specifics of the key equipment, including the turbomachinery, heat exchangers, and power cycle pump are examined in detail. The facility also incorporates auxiliary heat transfer systems and operational support systems, and the layout and function of each of these systems is described. The chapter concludes with a discussion of the instrumentation utilized throughout the facility, which was carefully selected to collect high-quality experimental data across various operating conditions.

3.1. Fundamental Working Principles

The core operational principle for the hybrid ORVC test facility was the integration of an organic Rankine power cycle and a vapor compression cooling cycle. In this configuration, thermal energy was absorbed by the organic working fluid in the ORC boiler. The power cycles turbine produced mechanical shaft power that was coupled to a compressor in the VCC. The compressor utilized this shaft power to drive the cycle and produce useful cooling power. In the hybrid configuration, an electric compressor was integrated into the VCC to provide a pathway for electric

input into the system. Figure 3-1 presents a simplified process flow diagram to help illustrate the basic working principles of the facility.

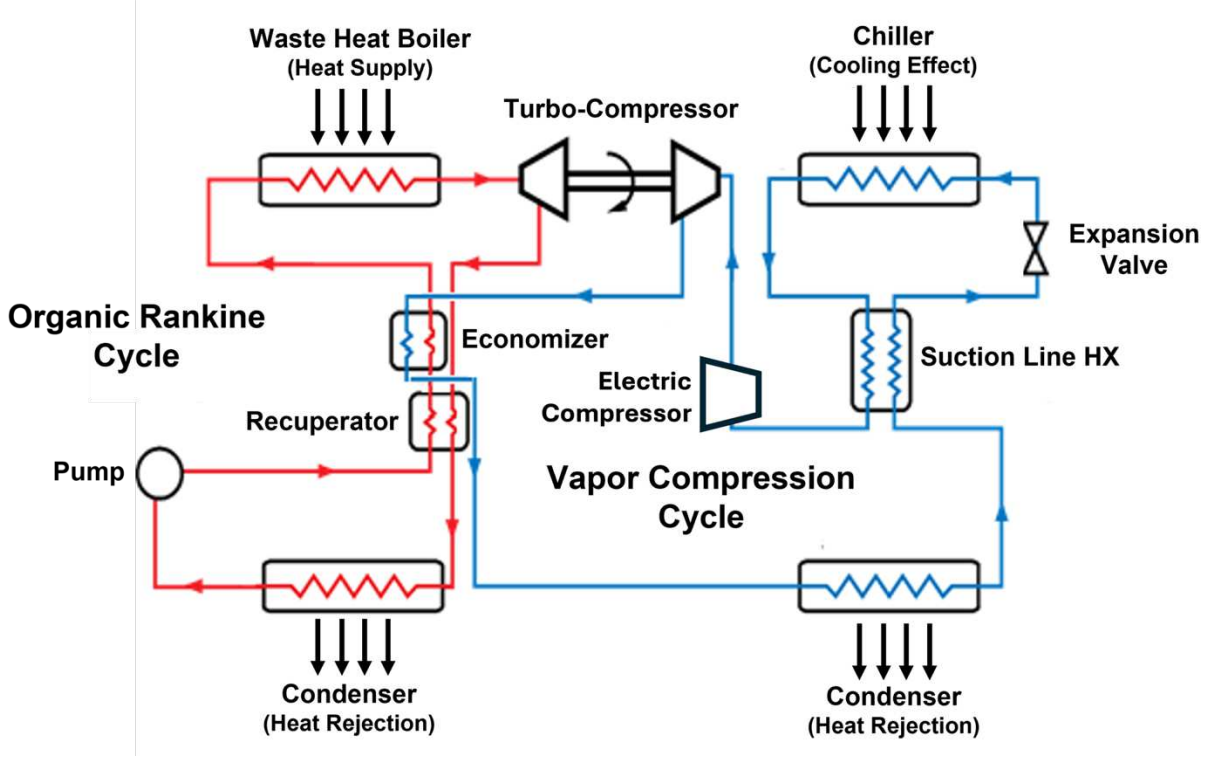

Figure 3-1: Simplified process flow diagram of the hybrid ORVC test facility.

3.1.1. Organic Rankine Power Cycle

The organic Rankine power cycle operated similarly to a traditional Rankine power cycle. However, an organic working fluid was utilized to enable operation at significantly reduced temperatures compared to traditional Rankine steam cycles (~90°C as opposed to ~500°C) [45,46]. In Figure 3-1 the ORC is shown in red. The cycle began with low-pressure liquid refrigerant entering the power cycle pump and being pumped to high pressure. After leaving the pump the fluid passed through the power cycle recuperator. The fluid was heated in the recuperator using residual heat left in the discharge of the turbine. The fluid then passed through the cross-cycle economizer, absorbing residual thermal energy remaining in the discharge of the cooling cycle compressors. Both the recuperator and cross-cycle economizer are heat recuperation strategies that

have been shown to improve system efficiency in existing literature [29–31,39,43]. After being preheated by both recuperative heat exchangers, the high-pressure refrigerant liquid entered the power cycle boiler. In this heat exchanger, heat was absorbed by the working fluid from the heat supply auxiliary loop. The fluid evaporated, leaving the boiler as a high-pressure superheated vapor. This process was the primary input of thermal energy used to drive the system. The high-pressure refrigerant vapor then entered the turbine. The fluid expanded to a low-pressure vapor through the turbine, resulting in the production of mechanical shaft power. The low-pressure vapor passed through the hot side of the power cycle recuperator before entering the power cycle condenser. In this heat exchanger, the working fluid rejected heat to the condenser auxiliary loop and condensed to a low-pressure subcooled liquid. The liquid refrigerant returns to the power cycle pump to complete the cycle. A generalized cycle is presented in Figure 3-2 as visualized on a temperature–entropy diagram.

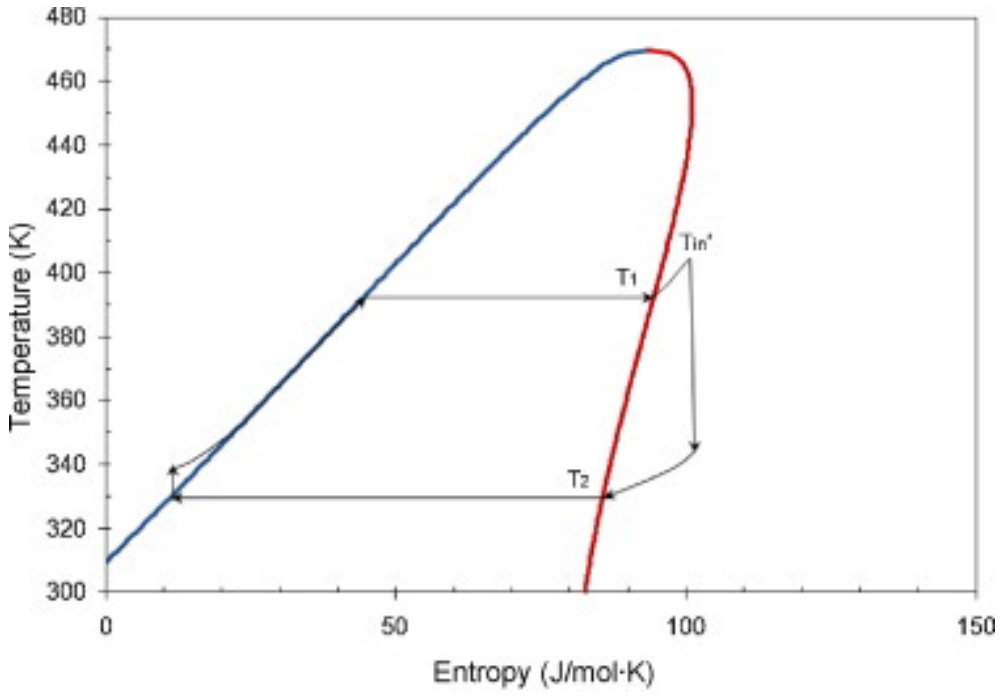

Figure 3-2: Generalized temperature-entropy diagram for an organic Rankine cycle with superheat. From [47].

3.1.2. Vapor Compression Cooling Cycle

The vapor compression cooling cycle is commonly used to provide cooling services [48]. For this work, the working principle for the vapor compression cycle was consistent with traditional systems. However, the addition of a second standalone marked a significant departure from typical configurations. The VCC is shown in blue in Figure 3-1. The cycle began with low-pressure refrigerant vapor entering the compressors. The compressors pressurized the fluid into a high-pressure vapor. This compression process was shared between the electric and thermally driven compressors. Details of the three compressor configurations evaluated will be discussed in Section 3.2.1. After leaving the compressors, the high-pressure refrigerant vapor entered the cross-cycle economizer. The vapor was cooled in this heat exchanger, providing thermal energy to heat the fluid entering the power cycle boiler. The high-pressure vapor then passed through the cooling cycle condenser. In this heat exchanger, heat was rejected from the working fluid, and it condensed to a high-pressure liquid. This high-pressure liquid passed through the hot side of the suction line heat exchanger (SLHX) rejecting energy to heat the discharge of the evaporator. This heat recuperation strategy helped improve performance by ensuring subcooling of the liquid condenser discharge as well as providing heat to guarantee superheat at the compressor suction [49]. After leaving the SLHX the high-pressure liquid passed through the expansion valve. The expansion process that occurred through this valve flashed the fluid into a low-pressure two-phase mixture. The mixture entered the evaporator where it fully evaporated, absorbing heat and generating the cooling effect that is the product of the system. The resulting low-pressure vapor passed through the cold side of the SLHX, absorbing recuperated thermal energy, and then returning to the compressors to complete the cycle. **Figure 3-3** depicts the processes of an idealized vapor compression cycle on a temperature–entropy diagram.

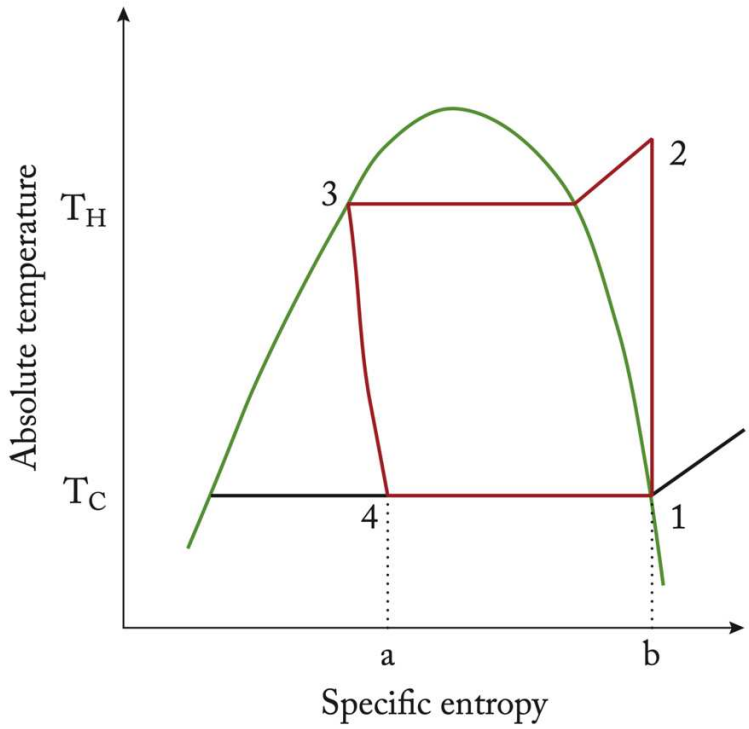

Figure 3-3: An idealized vapor compression cycle shown on a temperature-entropy diagram. Adapted from [50].

3.2. Test Facility Layout

The hybrid ORVC test facility developed for this research consisted of a coupled ORC and VCC and integrated a standalone electric compressor. The facility also included auxiliary heat transfer systems to deliver heat to and from various heat exchangers throughout the hybrid ORVC prototype. Other operational support systems are also integrated into the facility including turbomachinery cooling systems, a cross-cycle charge management system, and a power cycle pump health system. An overview photo of the test facility is shown in Figure 3-4.

Figure 3-4: Overview photo of the hybrid ORVC test facility as configured for this research.

The P&ID in Figure 3-5 includes key auxiliary systems such as compressor bearing cooling and lubrication, cross-cycle refrigerant charge management, and auxiliary heat transfer loops, along with the main flow paths of the core cooling and power cycles. Figure 3-5 also includes state point numbers that will be referenced during the discussion of results. In the power cycle, state points 6 and 7 refer to the saturated vapor and saturated liquid conditions within the condenser. States 16 and 17 represent saturated liquid and saturated vapor conditions in the boiler. In the cooling cycle, state points 7 and 8 identify saturated liquid and vapor conditions in the condenser, and state points 14 and 15 represent the two-phase condition at the inlet to the evaporator and the saturated vapor condition inside the heat exchanger.

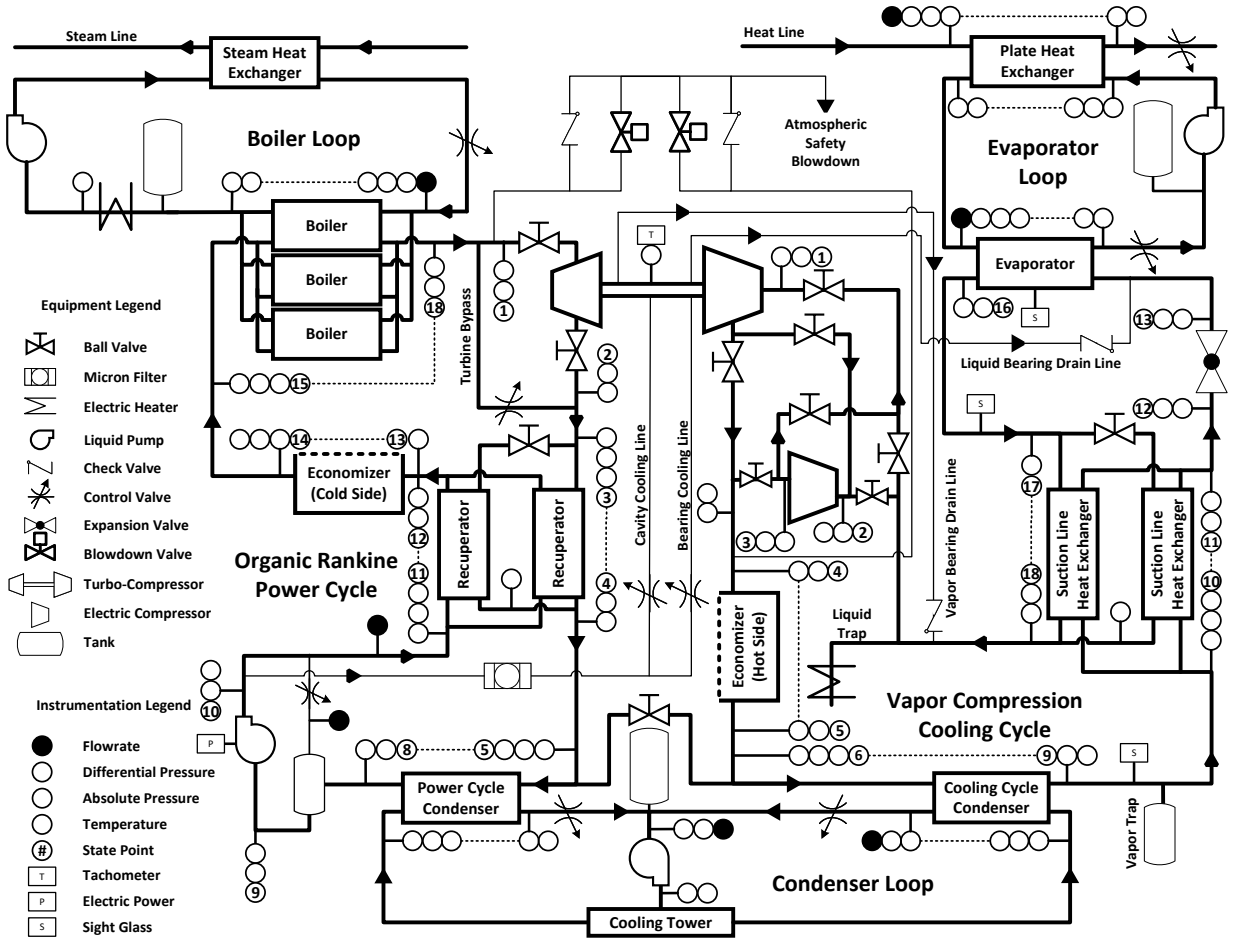

Figure 3-5: Detailed piping and instrumentation diagram of the hybrid ORVC test facility.

Each of the main systems and components depicted in Figure 3-5 are discussed in the following sections. Details of the operating modes and compressor configurations are presented, followed by a description of the key components utilized throughout the ORC and VCC. The auxiliary heat transfer loops and other support systems are also discussed in detail.

3.2.1. System Operating Modes

Integration of the standalone electric compressor into the ORVC system enabled the test facility to be operated in three distinct modes: electric cooling, thermal cooling, and hybrid cooling. Each mode is presented briefly to understand how the test facility operates in each mode.

3.2.1.1. Electric Cooling

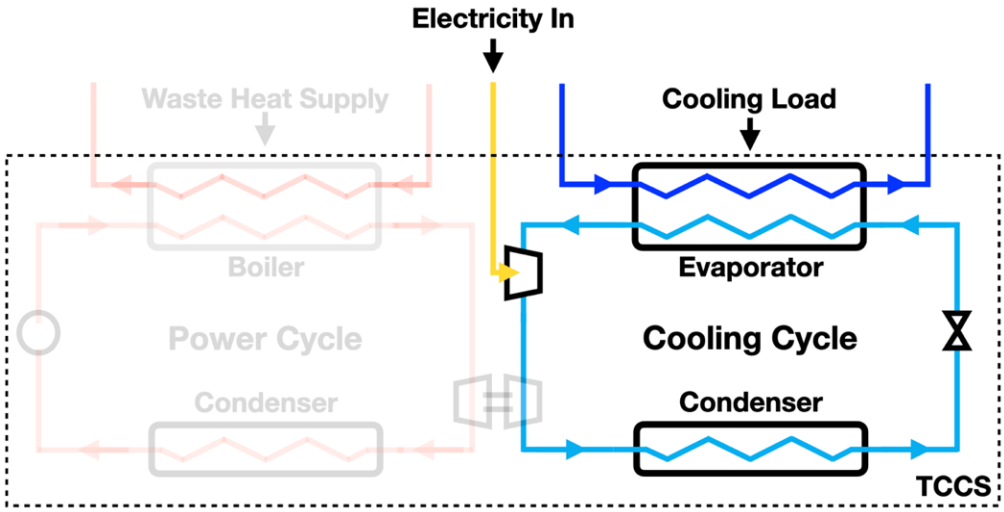

Figure 3-6: Simplified process flow diagram for the test facility operating in electric cooling mode.

In electric cooling mode, the organic Rankine cycle did not operate, as shown in Figure 3-6. The vapor compression cycle was entirely driven by the electric compressor. This operating mode is useful for applications where the availability of thermal energy is variable. When operating without thermal resources, the compression load was provided entirely by the electric compressor, driving the full capacity of the cycle. The flow was bypassed around the thermally driven compressor and the cooling demand was still fulfilled in the evaporator. In this mode, the prototype operated similarly to a traditional electric chiller, with electrical energy being consumed to produce cooling power.

3.2.1.2. Thermal Cooling

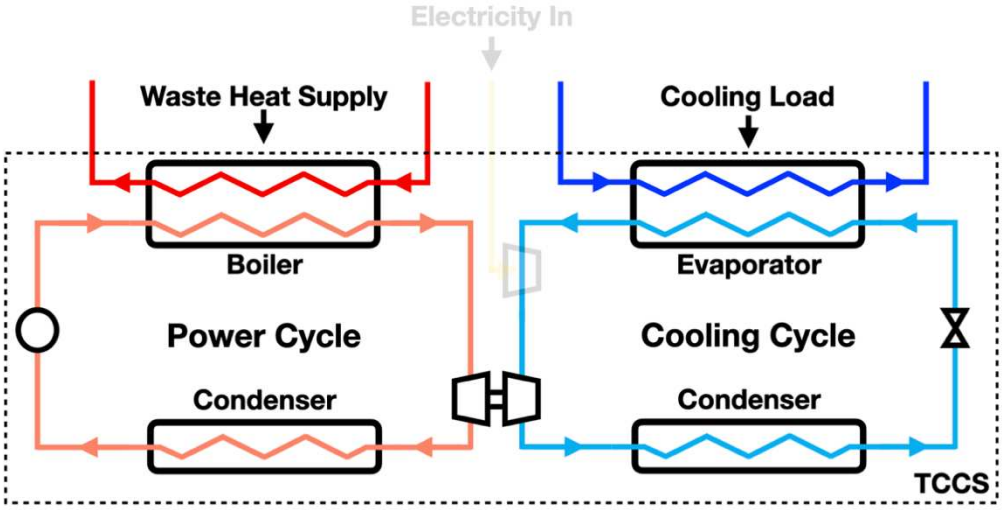

Figure 3-7: Simplified process flow diagram for the facility operating in thermal cooling mode.

Both the ORC and VCC operated in thermal cooling mode. However, as shown in Figure 3-7, the electric compressor did not operate in this mode. The compression load for the cooling cycle was entirely met by the thermally driven compressor using the mechanical work developed by the ORC. In this mode, the prototype operated similarly to a traditional thermally driven chiller. Heat was absorbed to drive the system and produce cooling power. When operating in this mode the facility did not consume significant amounts of electricity. This mode is ideal for applications or conditions when thermal resources are sufficient to meet cooling demands and consuming thermal resources represents cost and/or emissions savings when compared to using electricity.

3.2.1.3. Hybrid Cooling

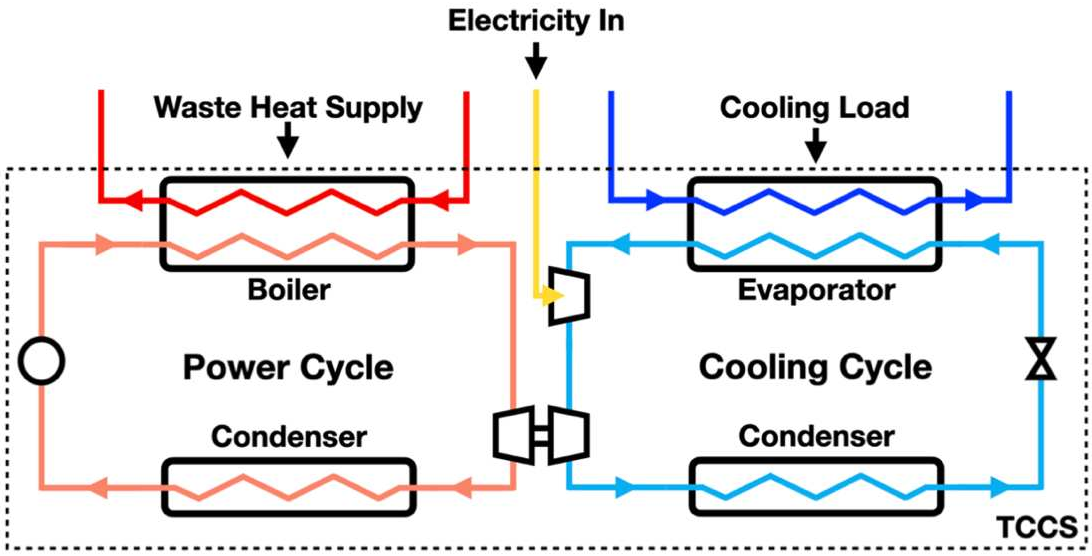

Figure 3-8: Simplified process flow diagram depicting the hybrid cooling operating mode.

Hybrid cooling is the novel operating mode that is the focus of this research. As shown in Figure 3-8, all of the major systems within the facility were operational in hybrid cooling mode. The compression load was shared between the electric and thermally driven compressors. This allowed the facility to deliver cooling power by consuming a combination of thermal and electric energy. In this operating mode, the system maximized the utilization of thermal resources while compensating for variations in heat availability, boundary temperatures, and cooling demand with on-demand electric input. This novel functionality was a key motivator for this investigation.

3.2.2. Compressor Configurations

The test facility was developed to enable multiple compressor configurations when operating in hybrid cooling mode. Figure 3-9 presents an excerpt of the full facility P&ID detailing the piping system that surrounds the two compressors and a photo of the integrated system in the test facility. The system consisted of multiple flow paths and a series of electronic flow control valves. This plumbing system enabled the investigation of three unique compressor configurations: one with the devices in parallel and two with the devices in series.

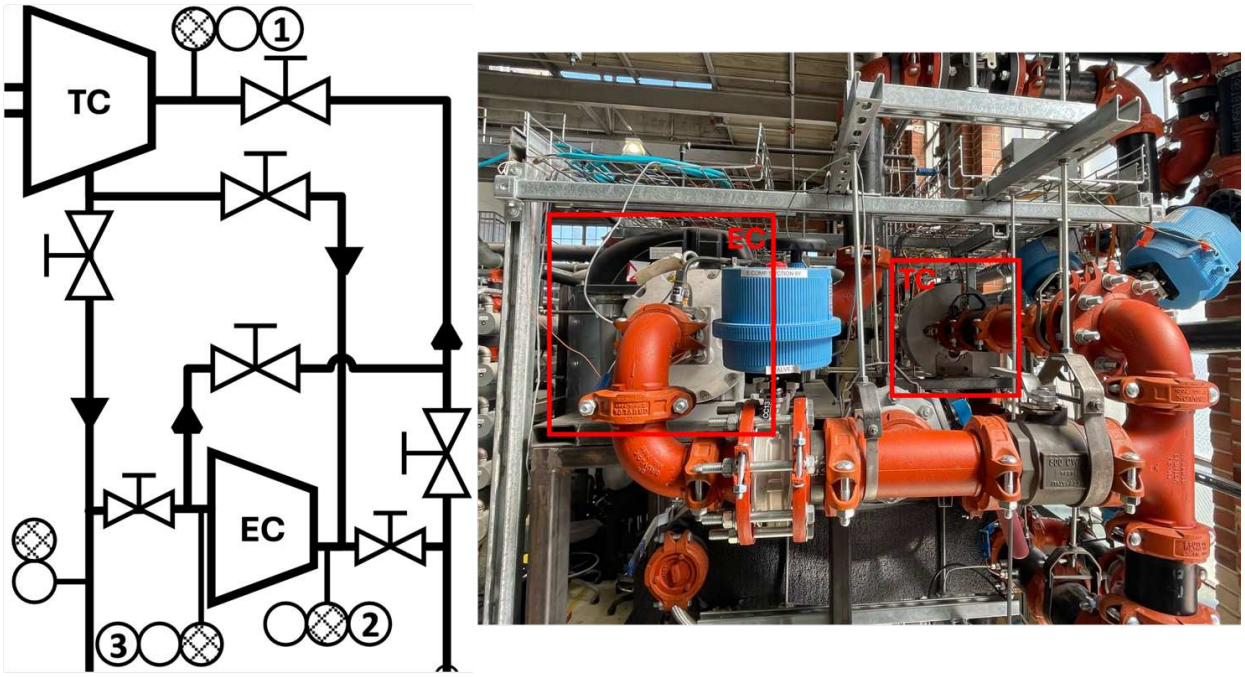

Figure 3-9: P&ID detail and hardware photo of the test facility compressor configuration enabling evaluation of three different arrangements.

Figure 3-10 presents a simplified process flow diagram of the three compressor configurations. The test facility was configurable to any of the three arrangements by adjusting the position of the valves in the plumbing system that surrounded the compressors. In the parallel configuration (PC), the refrigerant flow was split, with one stream passing through the electric compressor and the other passing through the thermally driven device. Each compressor provided full compression to its portion of the total mass flow. In the series configurations, the fluid underwent partial compression in the first stage device and then completed the compression process in the second stage device. In the series configurations, the full flow passed through both machines, but each device only provided a portion of the compression. The two configurations were identical, with only the order of the compressors reversed. Configuration EC1 arranged the electric compressor as the first stage and the turbocompressor as the second stage. Configuration TC1 reversed this order, placing the thermally driven compressor as the first stage and the electric device as the second.

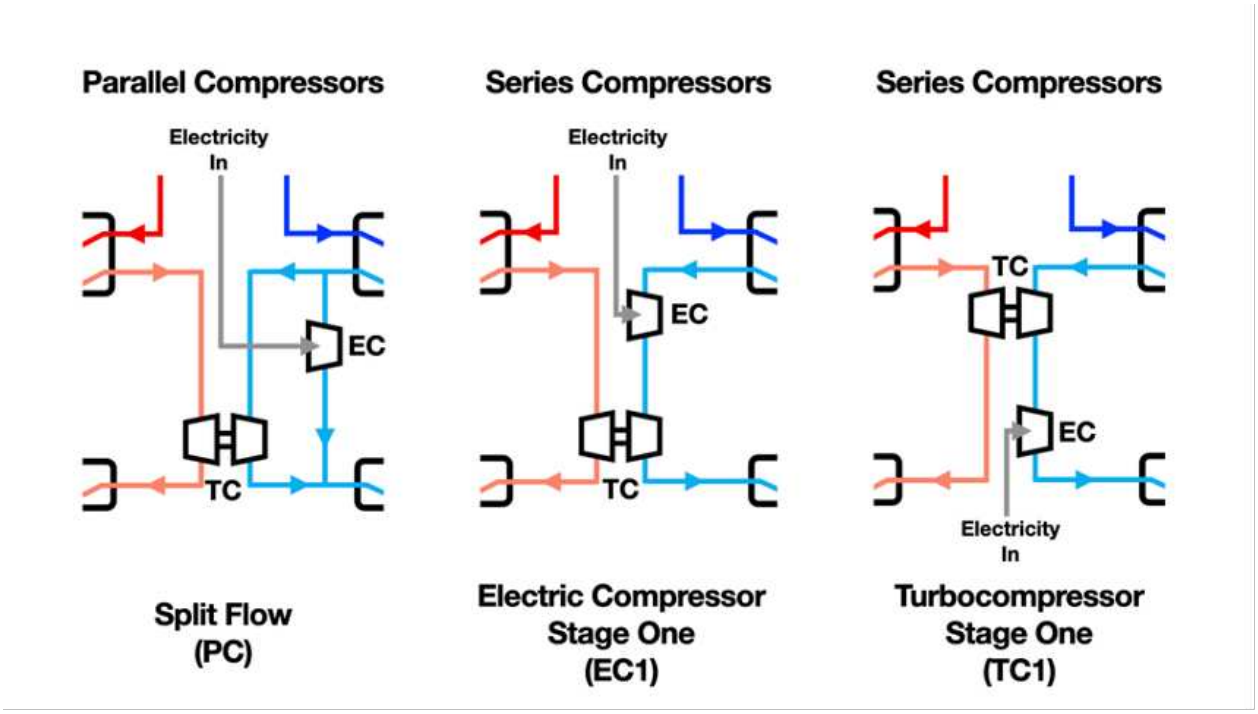

Figure 3-10: Three unique compressor configurations that were evaluated using the hybrid ORVC test facility.

3.3. Key Equipment

Details of some key components of the test facility are presented in the following sections. Certain characteristics of each component had implications for the overall performance of the prototype. Understanding these component details is important for some of the insights drawn from performance results in the following chapters.

3.3.1. Turbocompressor

One of the most important components in the test facility was the turbocompressor. This device coupled the ORC to the VCC and was a critical device in both cycles. The turbocompressor consisted of a radial inflow turbine and a centrifugal compressor mounted on a common shaft. Figure 3-11 presents a photo of the device.

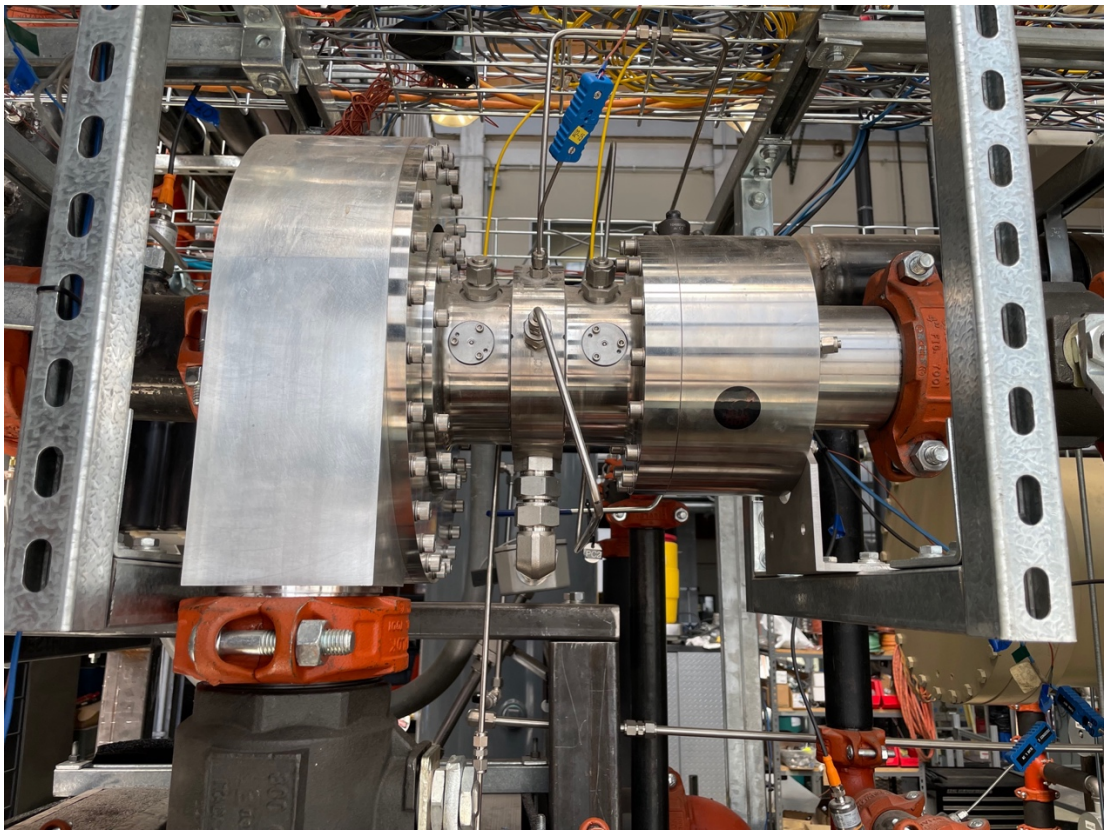

Figure 3-11: Photo of the turbocompressor device. The compressor housing is on the left and the turbine housing is on the right.

In the power cycle, high-pressure vapor entered radially (in the rear of the device in Figure 3-11), expanded through the turbine, and exited axially (to the right in Figure 3-11). In the cooling cycle, low-pressure vapor entered the device from the left, was compressed through the compressor, and exited the device at the bottom. The space between the two housings is called the cavity. Refrigerant-lubricated bearings and labyrinth seals separate the housings from the cavity and provide support for the shaft. Leakage from the shaft seals and bearings was collected in the cavity and drained into the evaporator through the pipe at the bottom of the cavity. The temperature of the cavity was monitored using the thermocouple on the top of the device.

The turbocompressor was a custom machine designed and fabricated by Barber-Nichols, Inc. The machine was designed to deliver 263 kW of cooling capacity while operating with

R1234ze(E). The design rotating speed was ~30 kRPM. Figure 3-12 shows the compressor map for the turbocompressor. This map was developed using computational fluid dynamics and provided by Barber-Nichols. This performance data indicates that the device was capable of high isentropic efficiencies (>80%) when operating in the center region of the map. This compressor map will continue to be discussed extensively in the following chapters.

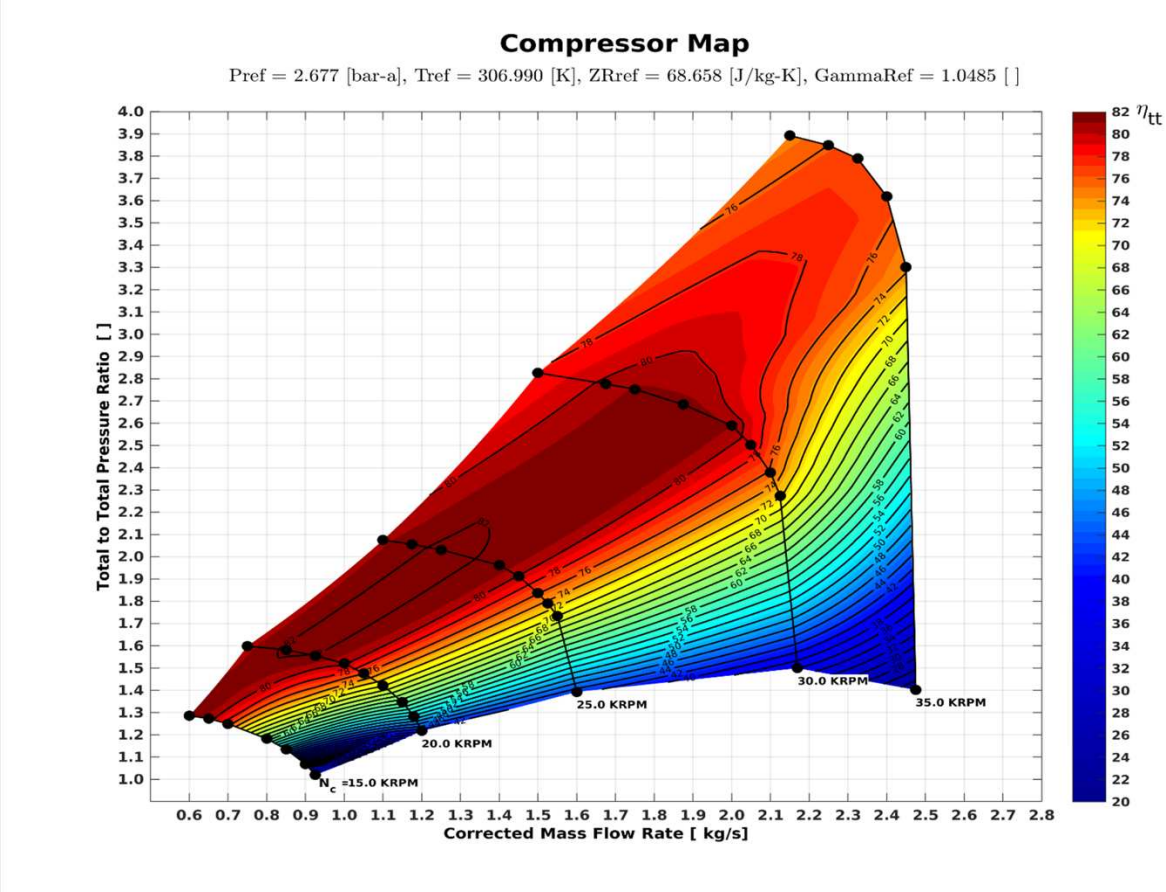

Figure 3-12: Compressor map for the turbocompressor provided by the device manufacturer.

3.3.2. Electric Compressor

The hybrid nature of the hybrid ORVC test facility stems from the inclusion of the electric compressor in the system. As such, the characteristics of the device have significant impact on the overall performance of the system. The electric compressor utilized in this work was a Danfoss

Turbocor TT300 which was generously provided by the funding agency for this project. A photo of the installed device is presented in Figure 3-13.

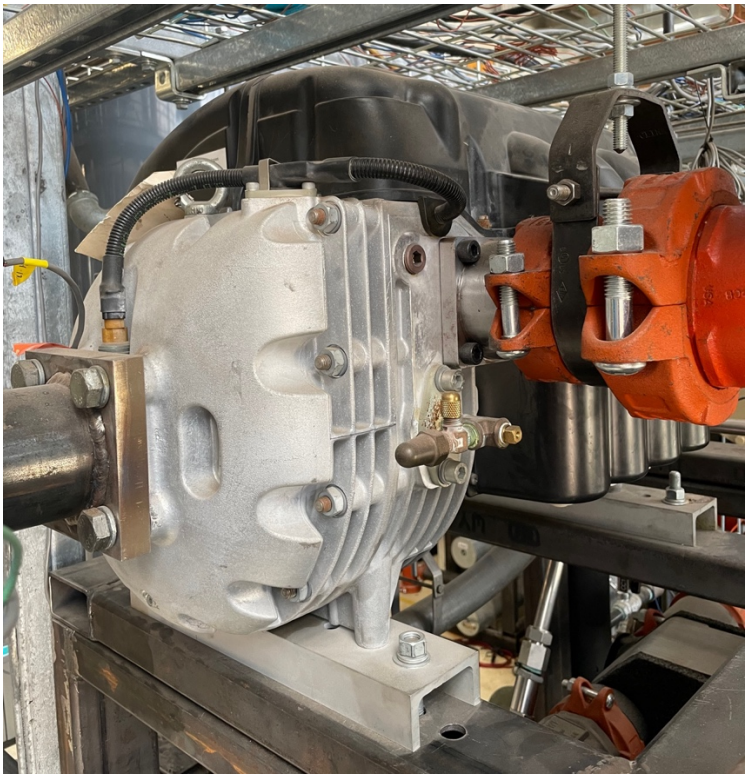

Figure 3-13: Photo of the Danfoss Turbocor TT300 electric compressor installed in the hybrid ORVC test facility.

The Danfoss Turbocor TT300 was a two-stage electric compressor designed for application in the HVAC industry. An integrated electric motor powered the device, driving both compressor stages via a common shaft. The device was also oil-free, using magnetically levitated shaft bearings. Fluid enters the unit at the suction on the left side of Figure 3-13 and leaves at the discharge on the right side of the image. The unit was designed to deliver 211 kW – 317 kW using R134a as a working fluid. The Danfoss TT300 was selected for this work based on the design point cooling capacity matching the designed capacity of the turbocompressor. However, the differing design operating fluids (R1234ze(E) and R134a) led to a capacity mismatch between the two

devices. The performance implications of this mismatch will be discussed in detail in the following chapters.

The TT300 included some additional features that enhanced its performance in typical HVAC applications. The device included variable angle inlet guide vanes (IGVs) and a variable speed drive. IGVs impart a rotating component to the velocity of the fluid in the suction of the compressor. The amount of rotational velocity, or pre-swirl, can be modulated by adjusting the angle of the IGVs. When used in combination with a variable speed drive, the operating range at low load and pressure ratio can be greatly expanded [51]. The TT300 also included soft-start electronics (a system primarily composed of large capacitors) to enable the slow ramp-up of the compressor speed, limiting in-rush current to the electric motor and preventing aerodynamic instability in the compressor. The device also included onboard safety controls that continuously monitored the operating state of the machine. These controls imposed operating limits to maintain operation within the operating map of the compressor. If operating conditions moved beyond the limits of the compressor, the safety control system would fault, triggering a rapid shutdown of the device. Unlike the data provided for the turbocompressor, the limits and characteristics of the compressor map for the TT300 were not available for this project. Instead, an operating map for the TT300 was developed experimentally. This is discussed in depth in Chapter 4.

An electrical and control system was developed to provide power to the compressor. The device required a three-phase electric supply at 480V. This was supplied from the main electric switchgear at the Powerhouse Energy Campus via a 150A circuit breaker, a line reactor, and power conditioning electronics. An overview of the power and control electronics, including this main power supply circuit, is shown in Figure 3-14 (left). The circuit breaker provided overdraw protection for the system. The line reactor limited the inrush current upon motor startup and served

to flatten any voltage spikes coming from the grid. Additional electronic components are contained in the power electronics enclosure shown in Figure 3-14 (right). These components included a secondary circuit breaker, a contactor, a transformer, and a surge protector, and provided further circuit protection, electronic switching, and power conditioning.

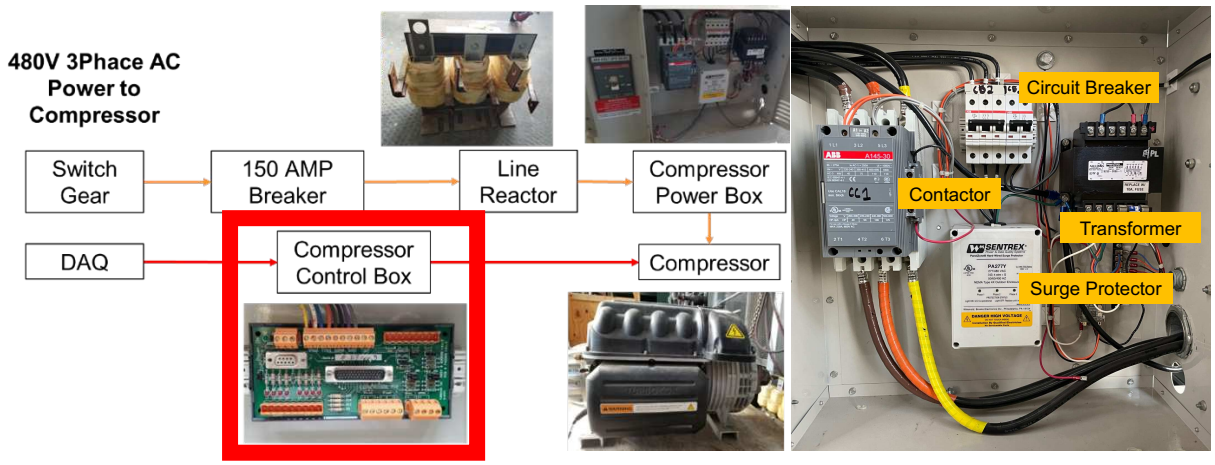

Figure 3-14: Overview of the electric compressor power supply and control system (left) and detail of the power electronics box (right), with the main control interface highlighted in red.

The compressor also needed to interface with an external control system for demand control, and emergency shutdown inputs, and to provide status signal outputs. This is accomplished via the Compressor I/O Board in the Compressor Control Box as shown in Figure 3-14. A standard 4-20 mA signal was used to provide demand input and report compressor speed. Digital circuits provided emergency shutdown control and reported compressor status.

3.3.3. Heat Exchangers

The prototype system was comprised of seven main heat exchangers. The primary power cycle heat exchangers were the boiler and power cycle condenser. The cooling cycle included the evaporator and cooling cycle condenser. The test facility also included three recuperative heat exchangers: a power cycle recuperator, a cross-cycle economizer, and a suction line heat exchanger (SLHX).

3.3.3.1. Power Cycle Boiler

The power cycle boiler, or generator, was one of the most critical components in the hybrid ORVC test facility. Figure 3-15 shows images of a power cycle boiler core prior to installation (bottom) and installed in parallel with two other cores in the test facility (top). The device was a compact, custom-designed, aluminum brazed, plate-fin heat exchanger. It was configured in a cross-counterflow arrangement to vaporize liquid refrigerant coming from the economizer before it enters the turbine. Liquid refrigerant from the economizer entered the device at the bottom right, winding through the device before leaving as a superheated vapor at the bottom left. The glycol mixture of the heat supply circuit entered at the left end of the device, flowed opposite to the refrigerant flow, and exited the device on the right. The power cycle boiler was configured as three independent heat exchanger cores arranged in parallel to enhance heat transfer and reduce pressure losses through the device.

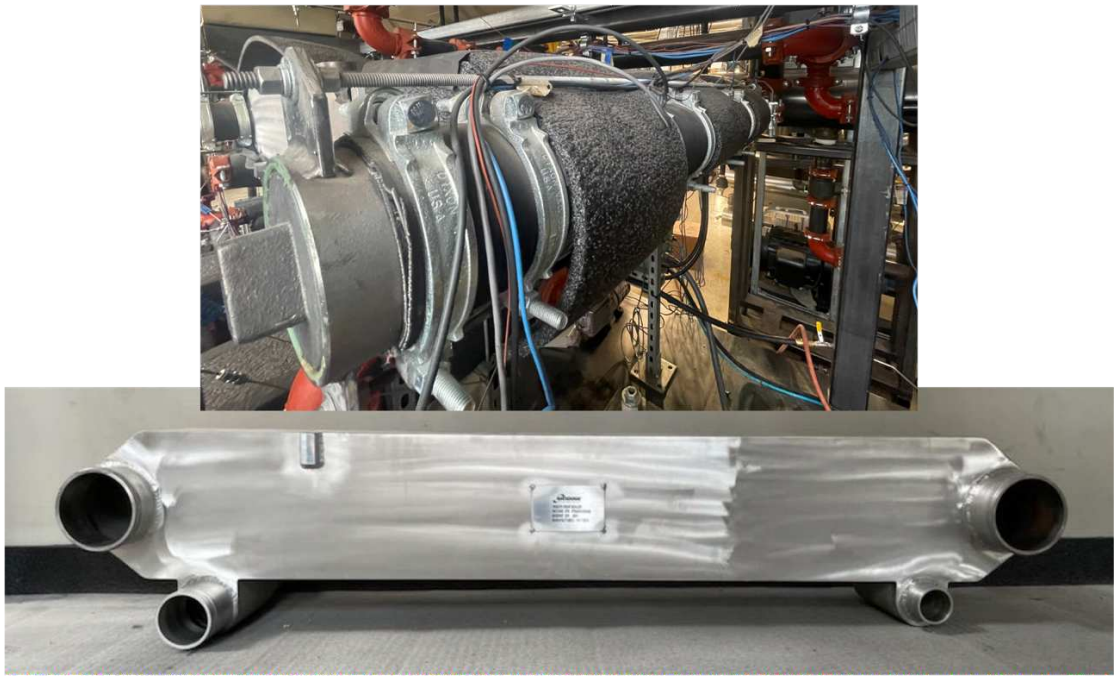

Figure 3-15: Photos of the power cycle boiler uninstalled (bottom) and installed and insulated in the test facility (top).

3.3.3.2. Condensers

The condensers for both cycles were commercially available units sourced from Provides US Inc. The devices are standard four-pass shell and tube units designed to liquefy refrigerant vapor. Superheated vapor from the recuperator entered the top of the power cycle condenser shell, condensed, and then exited the bottom of the device. Superheated vapor from the economizer completed the same process in the cooling cycle condenser. The glycol mixture from the heat rejection circuit flowed in the tubes of both devices, entering and exiting at the same end of the device. The shell geometry is identical between the two devices; however, the tube geometry differs slightly to accommodate the different heat duties associated with each condenser. Figure 3-16 presents a photo of the cooling condenser installed in the facility.

Figure 3-16: Photo of the cooling cycle condenser installed in the hybrid ORVC test facility.

3.3.3.3. Evaporator

The cooling cycle evaporator is the final phase change heat exchanger in the system. This device was another commercially available shell and tube unit from Provides US Inc. The unit was a four-

pass, spray evaporator. The two-phase refrigerant mixture leaving the expansion valve entered the device at the bottom of the shell. The mixture was sprayed through an array of nozzles in the shell onto the tubes. The fluid evaporated and the resulting vapor left the device through the top of the shell. The heated glycol mixture from the simulated cooling load flowed through four tube passes, entering and exiting the unit at the same end. Figure 3-17 presents a photo of the installed unit.

Figure 3-17: The shell and tube spray evaporator installed in the test facility.

3.3.3.4. Recuperative Heat Exchangers

The remaining heat exchangers in the hybrid ORVC system were the three recuperative heat exchangers. All three devices were custom-fabricated brazed aluminum plate heat exchangers operating with single-phase fluids in a counterflow arrangement. The power cycle recuperator and SLHX consisted of two heat exchanger cores arranged in parallel. The cross-cycle economizer consisted of a single core. Figure 3-18 presents images of each of the three recuperative heat exchangers.

Figure 3-18: Power cycle recuperator, cross-cycle economizer, and suction line heat exchanger cores (left to right).

3.3.4. Power Cycle Pump

The final key component within the hybrid ORVC system was the power cycle pump. This pump pressurized liquid refrigerant from the condenser pressure up to the boiler pressure before the fluid entered the cold side of the recuperator. Figure 3-19 shows the unit installed in the test facility. The device utilized in the test facility is a commercially available side channel pump from SERO Pump Systems. Specifically, the machine is an SRZS 446 model that features six stages and a low net-positive suction head (NPSH) first-stage impeller. Liquid refrigerant entered from the right side of the device and was discharged at high pressure from the top of the machine. An electric motor drives the pump at the shaft interface on the left side of the device.

Figure 3-19: SERO SRZS 446 power cycle pump installed in the hybrid ORVC test facility.

There were a few advantages of the SRZS pump that led to it being utilized in the test facility. The low NPSH requirements of the machine were particularly advantageous for this

application. Considering the relatively compact nature of the facility and limited subcooling available at the pump suction, the available NPSH for the pump was relatively low. The SRZS machine was able to deliver the required pumping performance despite the NPSH constraints. The SERO pump was also advantageous for its ability to reach a high-pressure head at a relatively low flow rate. Head and NPSH curves for the device are presented in Figure 3-20.

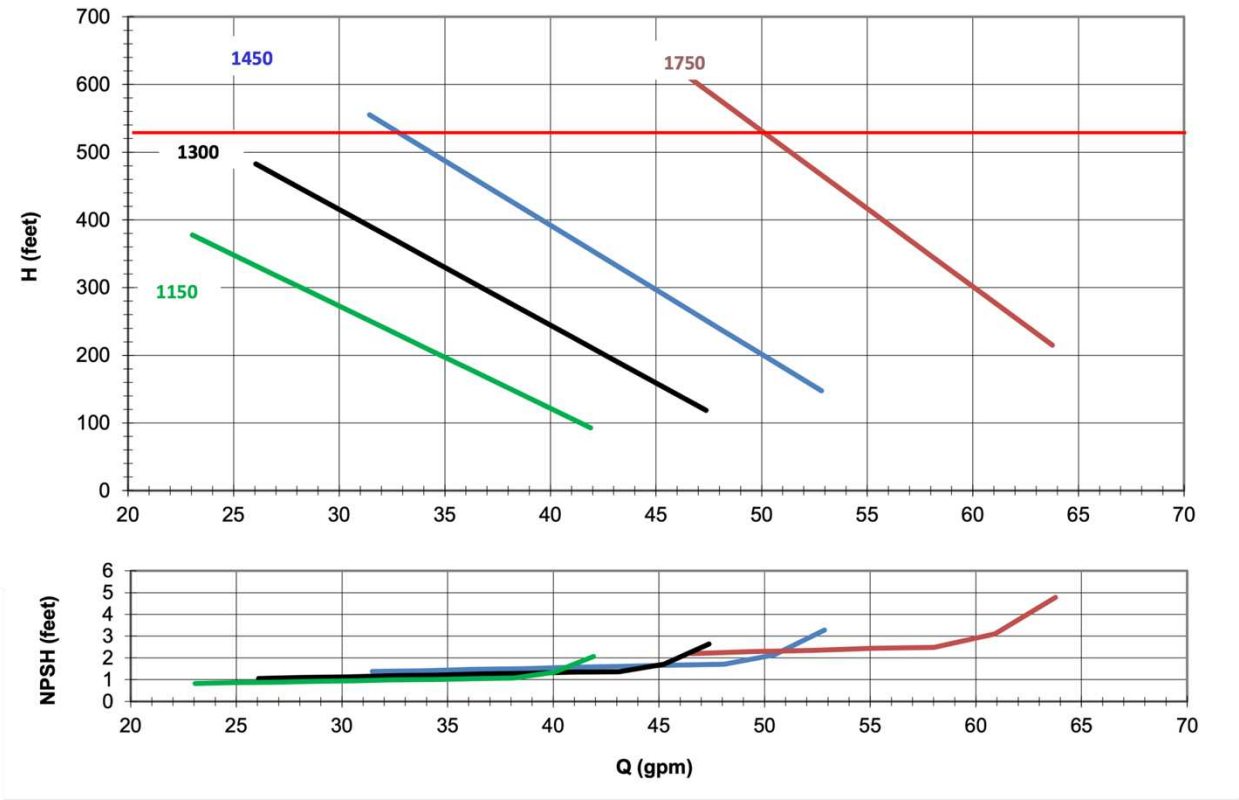

Figure 3-20: Head and NPSH data for the SERO SRZS 446 power cycle pump. The horizontal red line indicates the full load head requirement for the test facility. Adapted from [52].

3.4. Auxiliary Heat Exchange Loops

Outside of the main hybrid ORVC system, the test facility included three critical auxiliary heat transfer systems. These systems supplied heat, rejected heat, and simulated a cooling load for the hybrid ORVC system. The components and configuration of each system are discussed briefly in the following sections.

3.4.1. Heat Supply Circuit

The heat supply circuit or boiler loop provided a stream of thermal energy to the power cycle boiler. The system circulated an ethylene glycol-water mixture through the power cycle boiler to deliver heat to the hybrid ORVC system. The primary heat source for the system was a natural gas-fired steam generator. Figure 3-21 displays an excerpt of Figure 3-5 that details the heat supply circuit.

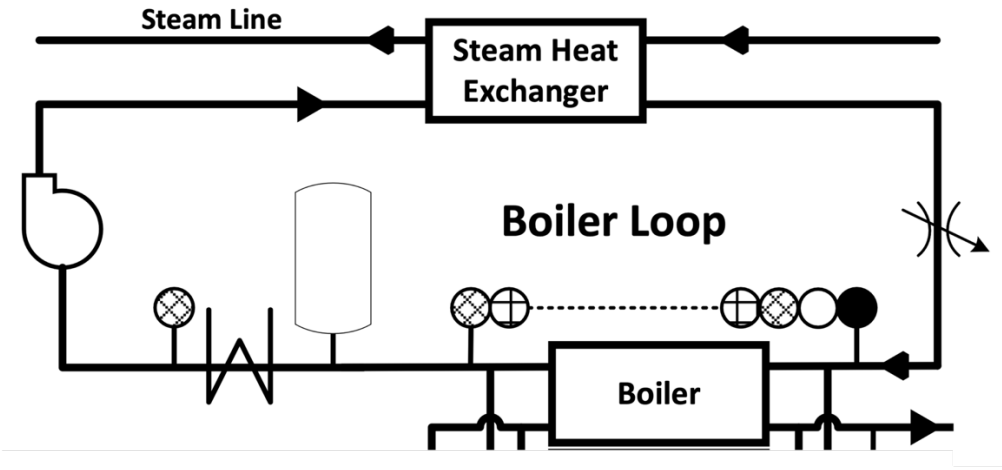

Figure 3-21: Detailed P&ID of the heat supply auxiliary system.

The system is circulated by a centrifugal pump designed to withstand the elevated heat in the system. The natural gas steam generator supplied steam via the steam line to the steam heat exchanger. In this device, the steam condensed and transferred heat to the glycol mixture. The glycol loop included a flow control valve, and six circulation heaters to modulate heat supply and provide additional heat input. A thermal expansion tank was also included in the system to provide a safe amount of expansion volume to prevent strain on the piping system as the glycol was heated and cooled. Photos of the electric heaters and the steam generator that were used to provide heat to the heat supply loop are shown in Figure 3-22.

Figure 3-22: The six circulation heaters (left) and natural gas steam generator (right) that provided heat to the heat supply circuit.

3.4.2. Heat Rejection Loop

The heat rejection, or condenser loop, removed thermal energy from the condensing heat exchangers in the hybrid ORVC system and rejected it to the environment using an evaporative cooling tower. Similarly to the boiler loop, an ethylene glycol and water heat transfer fluid was circulated through the condensers. The heated fluid was then passed through an evaporative cooling tower to reject the energy to the atmosphere. Figure 3-23 displays a section of Figure 3-5 focused on the condenser loop.

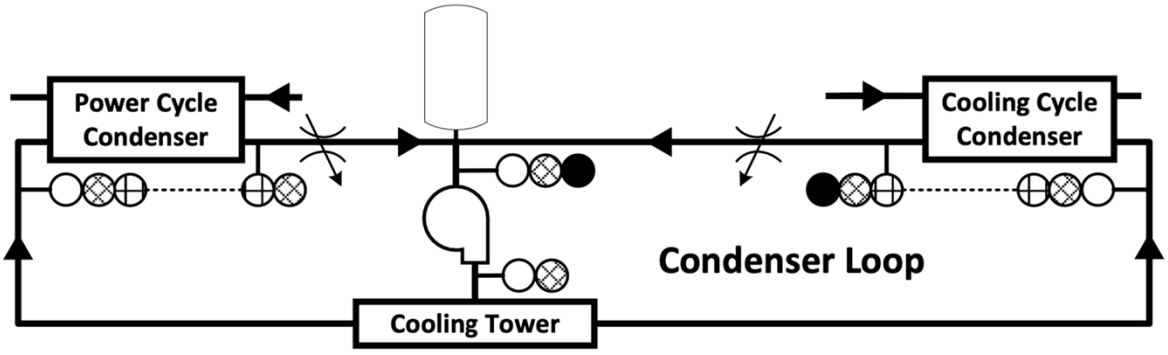

Figure 3-23: Detailed P&ID for the heat rejection loop.

The system arranged the two condensers in parallel with the flow to both heat exchangers coming directly from the cooling tower. One pump circulated the heat transfer fluid to both condensers. The system also incorporated a surge tank to manage thermal expansion and flow control valves for each condenser. Flow meters were also included to measure the flow through each device.

The cooling tower rejected all the heat from the system to the atmosphere. Water was sprayed on the tube bundle inside the cooling tower to cool the heated glycol mixture passing through the tubes. A variable-speed fan also drew air across the tube bundle providing additional heat rejection via evaporative cooling. The variable frequency drive of the fan allowed for modulation of the capacity of the cooling tower. Figure 3-24 shows the cooling tower that was used to reject heat from the hybrid ORVC test facility.

Figure 3-24: Evaporative cooling tower installed outside of the Powerhouse Energy Campus.

3.4.3. Evaporator Loop

The final auxiliary heat transfer system simulated a cooling load for the hybrid ORVC system. Referred to as the evaporator loop, this system supplied heat to the cooling cycle evaporator to simulate a cooling demand on the system. Like the other two auxiliary systems, an ethylene glycol heat transfer fluid was used to transfer heat to the system. Heated glycol was circulated through the evaporator where it was cooled by the evaporating refrigerant. A pump then circulated the fluid to a plate heat exchanger where a secondary heated glycol stream heated the fluid. Figure 3-25 shows the section of Figure 3-5 that is focused on the evaporator loop.

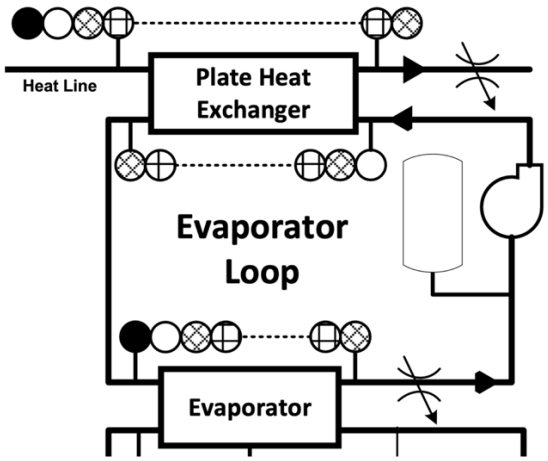

Figure 3-25: Detailed P&ID for the simulated cooling load system.

Like the other auxiliary systems, the evaporator loop included pressure, temperature, and flow rate measurements, as well as a thermal expansion tank and flow control valve. The secondary heated glycol stream also included a flow control valve that effectively modulated the level of input to the evaporator loop. Heat was provided to the secondary glycol heat line by a natural gas-fired circulation heater. Figure 3-26 shows some of the evaporator loop equipment installed in the test facility.

Figure 3-26: Evaporator loop equipment including pump and plate heat exchanger as installed in the test facility.

3.5. Operational Support Systems and Instrumentation

Apart from the core ORC and VCC cycles and the auxiliary heat transfer systems, there are a few systems that ensure the safe and reliable operation of the components within the test facility. Turbomachinery cooling systems are included for both the turbocompressor and the TT300 electric compressor. High-pressure liquid refrigerant was supplied from the discharge of the power cycle pump to the bearings and cavity of the turbocompressor for lubrication and cooling. Similarly, liquid refrigerant was supplied to the TT300 compressor to provide cooling to the electric motor. The test facility included a cross-cycle charge management system to maintain refrigerant charge levels in each cycle. A Liquiflo Max Series M6 cross-cycle gear pump was utilized to move refrigerant charge from the cooling cycle to the power cycle to counteract the collection of charge in the cooling cycle caused by the operation of the bearing cooling system. A pump health system was also integrated into the facility to improve the reliability of the power cycle pump. A pump bypass and receiver tank were installed to ensure that liquid refrigerant was available for the pump during flow instabilities that were experienced upon system startup. An API Plan 13 flush was also utilized to protect the shaft seal of the pump [53]. Figure 3-27 shows the receiver tank integrated into the test facility as part of the pump health system. The API Plan 13 flush can be seen in Figure 3-19.

Figure 3-27: Receiver tank and pump bypass health system.

The test facility was fully instrumented to enable collection of experimental data at all relevant locations to calculate the system performance. Figure 3-5 includes instrument types and locations throughout the test facility. The inlets and outlets of heat exchangers, pumps, compressors, and the turbine were monitored with thermocouples and pressure transducers. Both refrigerant and auxiliary heat transfer streams were fully instrumented. T-type thermocouples were utilized and calibrated against a platinum RTD standard to achieve a high level of accuracy. Pressure transducers included both absolute and differential-type devices and were calibrated against a deadweight pressure standard to maximize instrument accuracy. The maximum bias error for the thermocouples on the system was ± 0.323°C. The maximum bias error for the pressure transducers was ± 10.34 kPa. This higher bias error for the pressure transducers was correlated with the 0-500 psi devices used on the high-pressure side of the ORC. The average bias error for the pressure measurements was ± 2.45 kPa. Mass flow rates were also measured for the external heat transfer loops as well as the refrigerant flow in the power cycle. Auxiliary loop flow rate was

measured using paddle wheel flow meters with a maximum bias error of ± 4.69 GPM. The power cycle refrigerant mass flow rate was measured using a Coriolis mass flow meter with a bias error of ± 0.0023 kg/s. The cooling cycle mass flow rate was determined from an energy balance across the cooling cycle condenser.

3.6. Chapter Summary

This chapter presented a detailed description of the hybrid ORVC test facility that was utilized throughout this work. The fundamental working principles and basic thermodynamic theory for both the organic Rankine cycle and vapor compression cycle were discussed. The layout of the test facility was discussed with the presentation of a detailed P&ID. Electric, thermal, and hybrid operating modes were discussed. The capability of the facility to evaluate three compressor configurations (parallel – PC and series – EC1 and TC1) was also presented. Details of key equipment including the custom turbocompressor, TT300 electric compressor, heat exchangers, and power cycle pump were presented. The layout and components that comprise the auxiliary heat transfer systems that supply or remove heat from the hybrid ORVC system were also described. A discussion of the instrumentation utilized to collect experimental data concluded the description of the test facility provided in the chapter.

CHAPTER 4. Turbomachinery Analysis Methods and Integrated System Simulation

This chapter presents the simulation methodology that was utilized to model the fully integrated hybrid ORVC system. Details of the formulation of the coupled thermodynamic and turbomachinery models are discussed, and key model inputs are established experimentally. The three different compressor configurations were evaluated, and the integrated system was simulated at both design point and off-design operating conditions. Key findings from these simulations are synthesized and utilized to inform experimental design and facility configuration for the experimental studies discussed in Chapter 5 and Chapter 6. The content of this chapter was published in Applied Energy in Platt et al. and most of the images are from that paper [54].

4.1. Simulation Overview

To simulate this system, a model was developed that consisted of three separate components. A thermodynamic model provided the systemwide foundation of the analysis, which had key inputs of operating boundary conditions and system capacity. The model output key parameters like cycle flow rates and required compressor power, along with performance metrics like system COP and cycle efficiencies. The outputs from the thermodynamic model were used in the compressor model, which evaluated the performance of the compressors based on full system performance. The key outputs of the compressor model were the compressor operating points and efficiencies, which were returned to the thermodynamic model and the system was solved iteratively. Finally, a turbine model evaluated the performance of the turbine based on inputs from the thermodynamic model. This modeling structure is shown in the flow diagram presented in Figure 4-1.

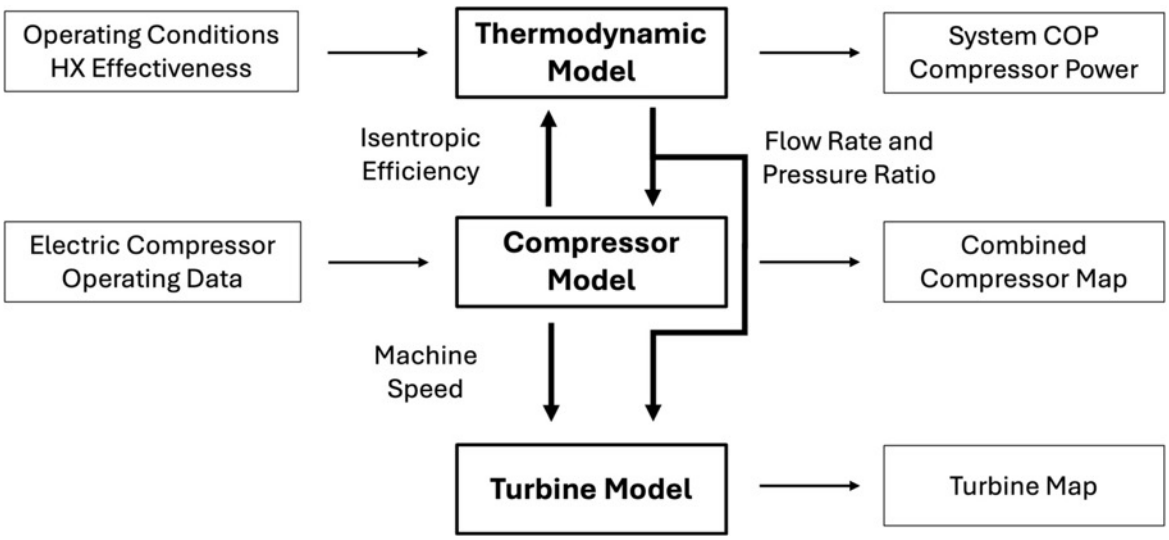

Figure 4-1: Modeling flow diagram with inputs and outputs of the thermodynamic, compressor, and turbine models.

The simulation process began with the thermodynamic model, where operating boundary conditions for the system were selected and input into the analysis. This included parameters such as heat input temperature, chilled water delivery temperature, heat rejection temperature, cooling duty, and heat input duty. Heat exchanger effectiveness values were selected from previous experimental work and input into the model. Fluid state points within the system were calculated and key performance metrics were determined, including system COP and required electric compressor power to meet the specified cooling duty. The thermodynamic model also output system flow rates and pressure ratios that were input to the compressor model. The compressor model was based on operating maps that were created using experimental data. Flow rates and pressure ratios from the thermodynamic model were plotted on the compressor maps to evaluate the operational feasibility and performance of each compressor in the system. Isentropic efficiency from this analysis was returned to the thermodynamic model, and the analysis was iterated until the efficiency used in the thermodynamic analysis converged with the performance predicted by the compressor model. Finally, a turbine model was developed to evaluate the operation of the

expander in the ORC. Power cycle flow rate and pressure ratio from the thermodynamic model were plotted on the turbine operating map. The rotating speed of the turbocompressor device was defined by the compressor map and input to the turbine model to normalize the flow rate to the machine speed. The model output operating points on the turbine map that defined the operating feasibility and performance of the device. At the conclusion of the simulation process, the thermodynamic performance of the system had been quantified along with the operating performance of each individual turbomachine. This provided a complete understanding of the operation of the hybrid ORVC concept. Each of the three components of the analysis are discussed in detail in the following sections.

4.2. Thermodynamic Model

The hybrid ORVC system was thermodynamically modeled by defining state points at the inlet and outlet of all components. Phase change heat exchangers (condensers, boiler, and evaporator) were split into multiple sections, depending on the fluid phase of the refrigerant side. The condensers and waste heat boiler contained three refrigerant phase regions: subcooled liquid (SC), two-phase mixture (TP), and superheated vapor (SH). The evaporator only contained two-phase and superheat regions. The fluids in the recuperative heat exchangers did not undergo phase change and therefore only contained one section, designated single phase (SP). Figure 4-2 displays the system flow diagram with split heat exchangers and external fluid flow directions. All heat exchangers were modeled as counter-flow devices.

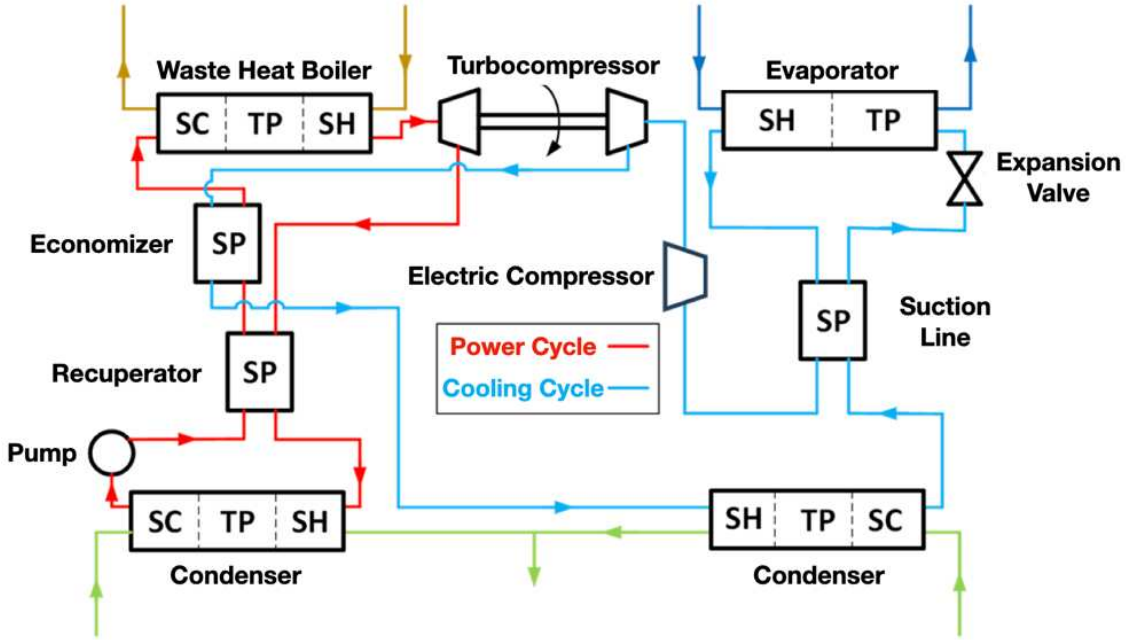

Figure 4-2: Overview of the hybrid ORVC thermodynamic model, where phase change heat exchangers were split into regions based on refrigerant phase: subcooled (SC), two-phase (TP), and superheat (SH). Single-phase heat exchangers are labeled SP.

A set of thermodynamic equations was simultaneously solved in Engineering Equation Solver (EES) [55] to analyze the performance of the ORVC system. Inputs to the model included the operating boundary temperatures (heat supply, heat rejection, and cooling delivery temperatures), heat supply, and cooling duty. Boundary temperatures were derived from Air-Conditioning, Heating, and Refrigeration Institute (AHRI) performance rating standards and are defined in the modeling conditions table or discussion for each series of simulations [56,57]. Heat input ranges were selected for each study to capture the full range of operation from fully thermal to fully electric modes. Cooling duty was defined based on the operating capacities of the compressors. This will be discussed in detail in a following section.

Inputs listed in Table 4-1 were held constant over the range of conditions for the simulations. To simplify the analysis, operation was assumed to be steady state, heat loss from all components and piping was assumed negligible, and the cooling cycle expansion valve was

assumed to be isenthalpic. All auxiliary work and component performance, such as pumping power for auxiliary fluids, was neglected in this study. The system was modeled with R1234ze(E) as the working refrigerant. Condenser water was an ethylene glycol-water mixture with a concentration of 30% glycol. The heat supply loop and chilled water were similar mixtures with glycol concentrations of 50% and 16%, respectively. Thermophysical properties for R1234ze(E) and the heat transfer fluids were determined from the standard databases in Engineering Equation Solver [55,58,59]. The pressure drop across each component and piping run was selected from Grauberger et al. [31] baseline experimental data. Curve fits for the effectiveness of each heat exchanger region were generated using experimental data from Grauberger et al. based on the heat duty of each device. These curves were used to set effectiveness values throughout the range of conditions in the simulation study.

Table 4-1: Key inputs for the hybrid ORVC thermodynamic model. Some inputs were sourced from existing experimental data [31].

Metric	Value
Turbine Isentropic Efficiency	77%
Pump Isentropic Efficiency	36%
Shaft Efficiency	99%
Electric Compressor Isentropic Efficiency	75%
Cooling Cycle Condenser Subcooling [ºC]	0.3
Pressure Drops	From Grauberger et al. [31]
HX Effectiveness	From Grauberger et al. [31]

Heat exchangers were modeled by solving an energy balance in each fluid section. Equation 4-1 is an energy balance on the external stream, either condenser water, heat supply glycol, or chilled water.

$$\dot{Q} = \dot{m}_{\text{ext}} * c_{\text{p}} * \left(T_{\text{ext,o}} - T_{\text{ext,i}}\right) \quad (4\text{-}1)$$

$\dot{Q}$ is the heat transfer between fluid streams in the heat exchanger, $\dot{m}_{\text{ext}}$ is the mass flow rate of the external fluid stream, c_{p} is the specific heat capacity of the external fluid, and $T_{\text{ext,i}}$ and $T_{\text{ext,o}}$ are the fluid temperatures at the inlet and outlet to the heat exchanger, respectively. Constant specific heat, evaluated at the average temperature, was a reasonable assumption for the external streams, as the specific heats do not change significantly in the relatively small operating temperature ranges of the fluids.

Equation 4-2 is an energy balance on the refrigerant side,

$$\dot{Q} = \dot{m}_{\text{r}} * \left(i_{\text{r,i}} - i_{\text{r,o}}\right) \quad (4\text{-}2)$$

where $\dot{m}_{\text{r}}$ is the mass flow rate of the refrigerant and $i_{\text{r,i}}$ and $i_{\text{r,o}}$ are the enthalpies at the inlet and outlet, respectively. For the recuperative heat exchangers, Equation 4-2 was used separately for each refrigerant side.

Equation 4-3 represents the efficiency of the heat transfer process,

$$\dot{Q} = \varepsilon * C_{\text{min}} * \left(T_{r,\text{i}} - T_{ext,\text{i}}\right) \quad (4\text{-}3)$$

where ε is the heat transfer effectiveness, C_{min} is the minimum heat capacity rate between the fluid streams ($\dot{m} * c_p$), and $T_{\text{r,i}}$ and $T_{\text{ext,i}}$ are the inlet temperatures of the refrigerant and external fluid, respectively. Equations 4-1 through 4-3 were used for each heat exchanger section to model system performance with varying external fluid temperatures and flow rates.

Similarly, the performance of turbomachinery was modeled using energy balances and isentropic efficiencies. The isentropic efficiency of the turbine, η_{turb}, was defined with Equation

4-4, where $i_{r,o,s}$ is the isentropic enthalpy at the outlet of the device. Equation 4-5 was used to determine the turbine power, $\dot{W}_{turb}$.

$$\eta_{turb} = \frac{i_{r,i} - i_{r,o}}{i_{r,i} - i_{r,o,s}} \tag{4-4}$$

$$\dot{W}_{turb} = \dot{m}_r * (i_{r,i} - i_{r,o}) \tag{4-5}$$

Turbine power was directly transferred to the cooling cycle compressor using a common shaft in the turbocompressor. However, there are mechanical losses including bearing friction and windage losses which were accounted for in Equation 4-6. Here, η_{mech} is the mechanical shaft efficiency and $\dot{W}_{comp}$ is the compressor work. Equations 4-7 and 4-8 were used to model the pump, waste heat compressor, and electric compressor.

$$\dot{W}_{comp} = \dot{W}_{turb} * \eta_{mech} \tag{4-6}$$

$$\dot{W} = \dot{m}_r * (i_{r,o} - i_{r,i}) \tag{4-7}$$

$$\eta_{comp} = \frac{i_{r,o,s} - i_{r,i}}{i_{r,o} - i_{r,i}} \tag{4-8}$$

By simultaneously solving Equations 4-1 through 4-8 with the operating conditions and fixed inputs from Table 4-1, the performance of the system was calculated. Fluid state points, flow rates, power cycle efficiency, cooling cycle COP, thermal COP, and electrical COP were all calculated from this thermodynamic model solution. Thermal COP and electric COP were calculated independently for this analysis, as opposed to a combined total COP value. Equations 4-9 and 4-10 define these performance metrics,

$$COP_{th} = \frac{\dot{Q}_{evap}}{\dot{Q}_{boil}} \tag{4-9}$$

$$COP_{e} = \frac{\dot{Q}_{evap}}{\dot{W}_{pump} + \dot{W}_{ec}} \tag{4-10}$$

where $\dot{Q}_{\text{evap}}$ is the cooling power produced by the system, $\dot{Q}_{\text{boil}}$ is the thermal energy absorbed in the power cycle boiler, and $\dot{W}_{\text{pump}}$ and $\dot{W}_{\text{ec}}$ are the electrical power consumed by the power cycle pump and electric compressor, respectively. Calculating these values independently enables evaluation of the performance of the system with respect to each energy source. This is useful as these energy sources often have differing costs and associated emissions depending on the application. Independent performance metrics enable future analysis to capture these nuances. Separate COP metrics also enable comparison with purely electric or thermally driven chillers to evaluate the performance of the hybrid ORVC system against more traditional technologies with a single form of energy input. The two COP metrics along with the other parameters calculated from the thermodynamic model were passed to the turbomachinery model to complete the analysis.

4.3. Turbomachinery Model

4.3.1. Turbomachinery Analysis Background

Before discussing the details of the compressor models that were developed for this work, it is necessary to present some background on two topics that are important for understanding the operation and performance of turbomachinery. Surge and choke describe two phenomena that can occur during turbomachinery operation when the application conditions are poorly aligned with the design conditions of the machine. The performance map for the turbocompressor showing its operating region and the surge and choke region is shown in Figure 4-3.

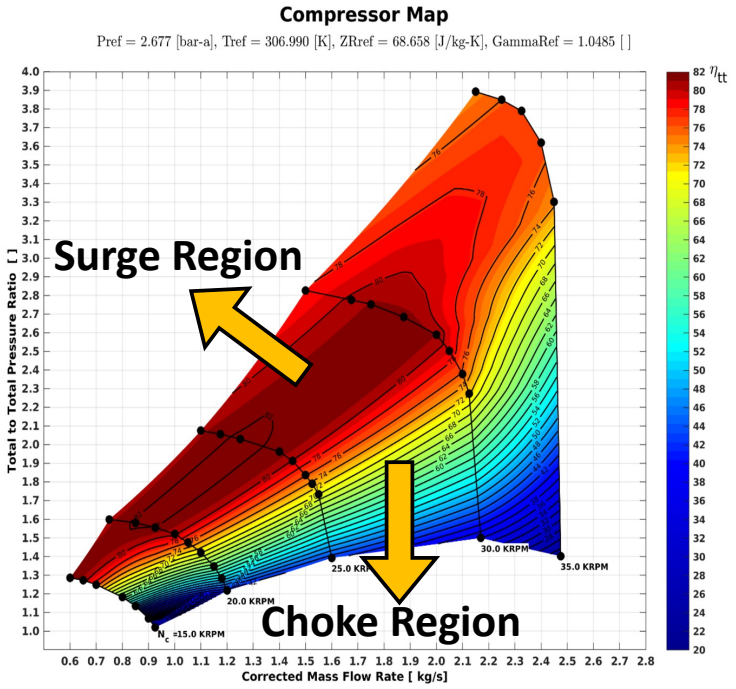

Figure 4-3: Performance map for the turbocompressor. Pressure ratio and corrected mass flow rate data bound the operating region of the device with colors representing islands of isentropic efficiency.

Corrected mass flow rate is plotted on the x-axis of the performance map and pressure ratio is plotted on the y-axis. The corrected mass flow rate is an equivalent value to the real mass flow rate that also accounts for variations in fluid properties and operating conditions. The correction process will be described in detail below. Different colors within the operating region represent the isentropic efficiency of the device when operating at that point. Lines of constant machine speed are also shown in black on the performance map. The surge region is located above and to the left of the operating region and the choke region is located below the operating map.

Surge is an unstable operating phenomenon that has been a focus for turbomachinery researchers for many years. This violent flow instability is a limiting factor for the operability of a device and is considered one of the most serious concerns in turbomachinery aerodynamics [60,61]. Surge can cause dangerous mechanical problems, reduced service life, and decreased

performance [62]. Surge is characterized by a reversal of flow from the high-pressure side of the device to the low-pressure side. Once the pressure on the outlet of the device has dropped due to this flow reversal, the compressor is able to recover and restore flow in the correct direction [63]. This process repeats in a cyclical fashion. An idealized surge cycle is shown in Figure 4-4.

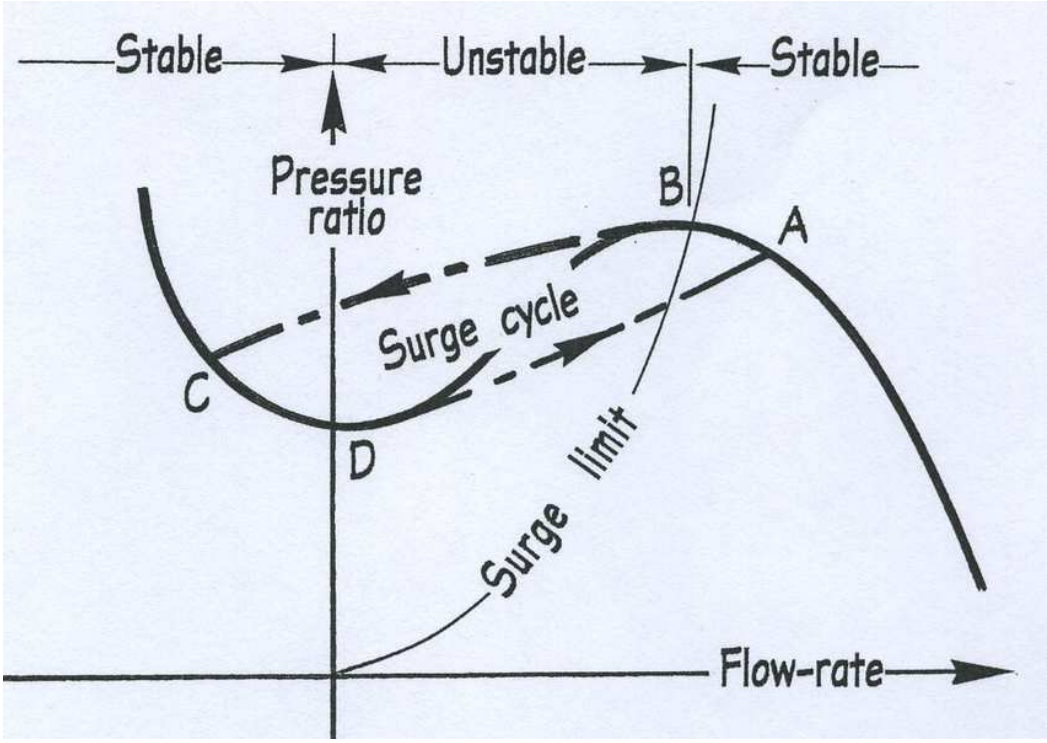

Figure 4-4: Typical surge cycle in a centrifugal compressor. When flow drops below the surge limit, flow reverses through the device until the pressure ratio drops enough for the compressor to restore flow in the correct direction. Sourced from [63].

The onset of surge in a turbomachine is linked to aerodynamic stall of the rotor blade [64]. Aerodynamic stall occurs when the loading of a blade becomes so great that flow separates from the blade causing turbulent flow in the blade passages [65]. Stall can propagate through a compressor or remain contained in localized stall cells. While linked, stall and surge are fundamentally different. Stall is a flow instability in the tangential direction of rotor travel while surge is an instability in the direction of flow. The flow rate through a device experiencing stall will remain steady while the flow rate through a surging device will pulse to the point of flow

reversal [61]. Stall, and especially surge, have negative impacts on the operation of a turbomachine and should be avoided.

The other constraint on the operating region of a turbomachine is choked operation. Choking happens when the flow through a device increases to the sonic limit and the flow rate reaches a maximum value [65]. This maximum flow rate provides an upper bound on the operating region of the turbomachine. While operating at or near choke is not considered as damaging as stall or surge, choked operation can produce thrust forces that can increase wear on shaft bearings. Apart from this, the main drawback of operating at or near choke is the loss of performance. Machine isentropic efficiency is typically highest near the surge limit, so operating on the opposite side of the map involves a decrease in performance [66].

4.3.2. Model Development

Turbomachinery models were developed for the turbine and compressors in the hybrid ORVC concept. These models evaluated the operational feasibility and performance of each device under certain operating conditions. Turbomachinery operating maps formed the basis for these models. Outputs ($\dot{m}$, pressure ratio) from the thermodynamic model were plotted on the operating maps to determine the isentropic efficiency of each machine and if the machines were in the surge or choke region. Operating maps for the turbine and thermally driven compressor have been developed using computation fluid dynamics and provided by the manufacturer of the device. The operating map for the Danfoss TT300 was generated experimentally with the device integrated into the test facility.

The operating map for the electric compressor was developed by performing a sweep test over a range of mass flow rates and pressure ratios. The sweep test consisted of a series of experiments with the compressor operating at pressure ratios ranging from 1.4 to 2.8. The mass

flow rate was varied from minimum to maximum at each respective pressure ratio. Minimum and maximum capacity were set by the internal control system of the TT300. Table 4-2 and Figure 4-5 show the data collected from the sweep test and the resulting operating map for the device.

Table 4-2: Experimental sweep test data for the Danfoss TT300 electric compressor

Pressure Ratio	$\dot{m}$ [kg/s]	$\eta_{measured}$	η_{avg}	$\eta_{curve\ fit}$
1.4	0.22 – 0.89	52.6% - 67.0%	58.5%	58.5%
1.6	0.42 – 0.89	61.2% - 73.3%	68.1%	68.0%
1.8	0.51 – 1.10	66.3% - 75.7%	71.2%	71.4%
2.0	0.53 – 1.19	67.6% - 76.5%	73.4%	73.1%
2.2	0.71 – 1.19	69.9% - 75.5%	74.3%	74.5%
2.4	0.51 – 1.28	70.0% - 78.3%	75.7%	75.5%
2.6	0.56 – 1.34	71.1% - 78.5%	76.2%	76.2%
2.8	0.51 – 1.44	71.7% - 78.9%	76.9%	76.8%

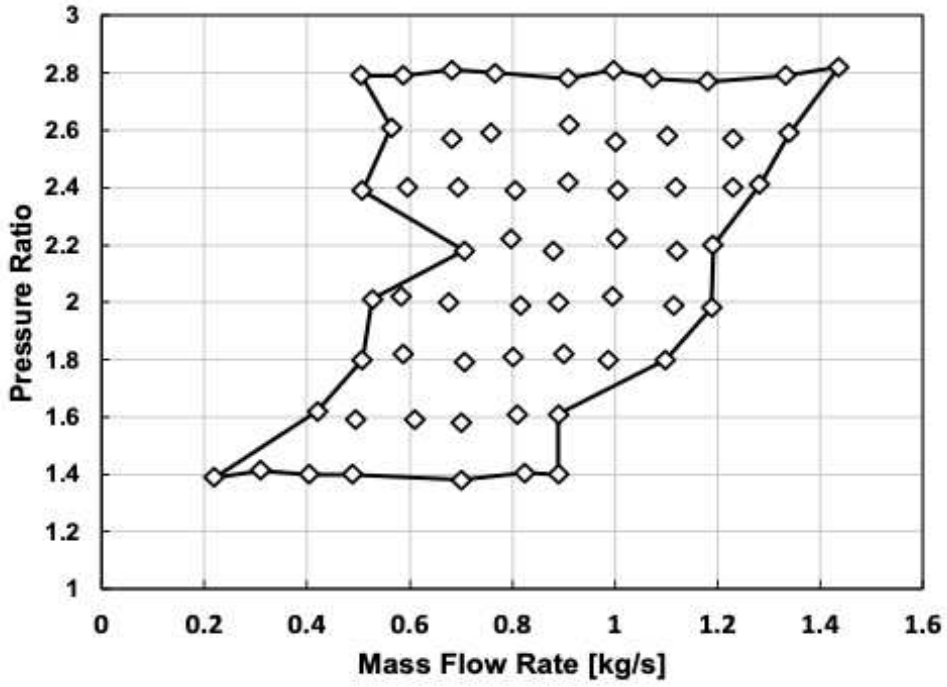

Figure 4-5: The operating region for the Danfoss TT300 compressor developed from sweep test data.

A curve fit of the isentropic efficiency of the electric compressor was developed using a sixth order polynomial curve fit of pressure ratio and average isentropic efficiency values collected during the compressor sweep test. This curve fit is presented in Equation 4-11, where $\eta_{s,ec}$ is the isentropic efficiency of the electric compressor and PR is the pressure ratio across the device. Values calculated from Equation 11 are shown in Table 4-2.

$$\eta_{s,ec} = -0.254 * PR^6 + 3.50 * PR^5 - 20.0 * PR^4 + 60.7 * PR^3 - 103 * PR^2 + 93.3 * PR - 34.4 \quad (4\text{-}11)$$

To enable comparison with the turbocompressor performance map, the flow rates from the electric compressor map were corrected to an equivalent mass flow rate. Correcting mass flow rates enabled the compressor performance to be compared across variable inlet conditions and different operating fluids, while ensuring aerodynamic similarity across these comparisons [67]. Equivalent mass flow rate, $\dot{m}_{eq}$, is defined in Equation 4-12,

$$\dot{m}_{eq} = \frac{\dot{m}_a \sqrt{\theta}}{\delta} \epsilon \quad (4\text{-}12)$$

where $\dot{m}_a$ is the actual mass flow rate in kg s^{-1}. The correction terms ϵ, θ, and δ are defined in Equations 4-13 – 4-15.

$$\epsilon \equiv \frac{\gamma_{ref}\left(\frac{2}{\gamma_{ref}+1}\right)^{\frac{\gamma_{ref}}{\gamma_{ref}-1}}}{\gamma_a\left(\frac{2}{\gamma_a+1}\right)^{\frac{\gamma_a}{\gamma_a-1}}} \quad (4\text{-}13)$$

$$\theta \equiv \left(\frac{V_{cr,a}}{V_{cr,ref}}\right)^2 \quad (4\text{-}14)$$

$$\delta \equiv \frac{p_{i,a}}{p_{i,ref}} \quad (4\text{-}15)$$

The ratio of specific heats, γ, is given as $\gamma = c_p/c_v$. Quantity p_i, is the inlet pressure in bar. Subscripts a and ref indicate actual or reference conditions respectively. V_{cr} is given in Equation 4-16.

$$V_{cr} = \sqrt{\frac{2\gamma}{\gamma + 1} g_c Z R T_i} \tag{4-16}$$

Z is the compressibility factor of the fluid, R is the specific gas constant of the fluid in J kg^{-1} K^{-1}, g_c is the gravitational constant in m s^{-2}, and T_i is the absolute inlet temperature of the fluid in K.

Equations 4-12 – 4-16 were solved to determine $\dot{m}_{eq}$ for each of the experimental cases in the compressor sweep test. Reference conditions were defined by the existing thermal compressor map and actual conditions were measured during each test. The points were plotted on the same compressor performance map to define an operating region for the electric compressor and enable its comparison with the operating region of the heat powered device. The resulting combined compressor map was utilized throughout the remainder of the turbomachinery analysis.

With operating maps created for the compressors, the thermodynamic model output data was plotted on the combined compressor map to identify a preliminary operating point for both devices. The electric compressor isentropic efficiency was calculated from the curve fit in Equation 11, and the thermal compressor isentropic efficiency was interpolated from the compressor map. Thermal compressor efficiency values interpolated from the map were constrained to between 40% and 90% (just beyond the minimum and maximum values on the compressor map). Both values were iterated into the thermodynamic model until there was less than a 1% difference between the values used in the thermodynamic model and the values predicted by the curve fit and compressor map. This iterative modeling process included both the thermodynamic and turbomachinery analysis to converge on a solution for both compressors.

The turbine was modeled once a solution for the compressor model had been reached. The performance map for the turbine in the ORC plotted the pressure ratio across the device on the y-

axis and the corrected mass flow rate through the device on the x-axis. Unlike the compressor maps, the corrected mass flow rate was normalized to the rotating speed of the device before being plotted on the map. To complete this part of the analysis, pressure ratio and flow rate information for the power cycle were output from the thermodynamic model. The turbocompressor speed was interpolated from the compressor map and used to normalize the flow rate to the machine speed. The resulting speed-normalized mass flow rate (in units of lbm/s/RPM to match the operating map from the manufacturer) was plotted on the turbine map against the power cycle pressure ratio. This yielded an operating point for the turbine, indicating the feasibility of the modeled conditions for the device.

At the conclusion of the modeling process, the simulation yielded thermodynamic operating conditions for the entire ORVC system, and performance map operating points for the turbine and both compressors. This provided insight into the operational feasibility and systemwide performance of the hybrid ORVC concept for the simulated conditions.

4.4. Simulation Results and Discussion

4.4.1. Compressor Configuration Comparison at Design Conditions

The combined compressor map was used to evaluate the results of the hybrid TCCS thermodynamic model. The first set of conditions simulated the system while operating with R1234ze(E) at AHRI standard rating conditions [56,57]. These conditions are an industry standard for the Heating, Ventilation, and Air-Conditioning (HVAC) industry.

Table 4-3 presents the AHRI conditions and the range of heat supply values simulated. The range of heat input duties represented fully thermal operation at modeling condition 1, hybrid operation at conditions 2-11, and fully electric operation at modeling condition 12. Each

compressor configuration (Parallel, EC1, TC1) was simulated across the full range of conditions in Table 4-3.

Table 4-3: Modeling conditions for design point compressor analysis based on standard parameters from AHRI Standards [56,57]. The range of heat supply values models the full range of operating conditions from fully thermal cooling to fully electric cooling.

Modeling Condition	Boiler Inlet Temperature [°C]	Heat Supply [kW]	Chiller Delivery Temperature [°C]	Chilling Duty [kW]	Condenser Inlet Temperature [°C]
1	91.0	450.0	6.7	263.8	30.0
2		409.1			
3		368.2			
4		327.3			
5		286.4			
6		245.5			
7		204.5			
8		163.6			
9		122.7			
10		81.8			
11		40.9			
12		0.0			

4.4.1.1. Parallel (PC) Configuration Results

Figure 4-6 shows the results for the parallel compressor configuration. Green numbers represent the operating point of the waste heat compressor at modeling conditions 1, 6, and 12. Yellow numbers represent the operating point of the electric compressor at the same modeling conditions. Point 1 represented fully thermal operation with 100% of the maximum available heat applied to the system. Point 6 represented operation when heat availability is approximately 50% of the full heat duty and Point 12 represented fully electric operation with 0% heat input.

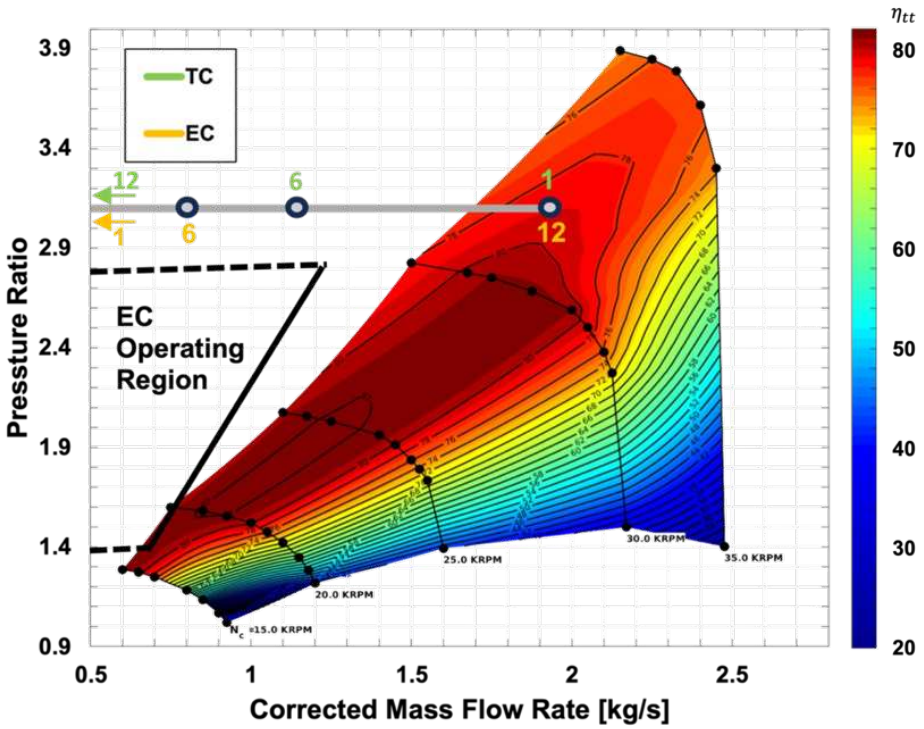

Figure 4-6: Compressor analysis results for design point conditions with both compressors in parallel. Point 1 for the electric compressor and Point 12 for the turbocompressor are off the figure to the left with corrected mass flow rates of 0 kg/s.

Figure 4-6 shows that the operating regions of the electric and thermal compressor had little to no overlap. This was caused by the different design operating fluids for the two devices (R134a and R1234ze(E)) and indicated that the corrected mass flow operating ranges for the devices were not similar. When operated in the parallel configuration, both compressors were required to deliver the full pressure ratio for all conditions. The turbocompressor (green) remained within the operating region at corrected mass flow rates above 1.7 kg s^{-1}, while waste heat supply was high, and the device provided most of the compression power. Once the corrected mass flow rate dropped below 1.7 kg s^{-1} (associated with decreased heat input), the device moved to the left of the operating map into the surge region. The electric compressor (yellow) remained above the operating map for all the modeled conditions, indicating that it was unable to deliver the required pressure ratio across the full heat input range. At medium heat input conditions (near Point 6,

~50% heat input), the electric compressor was closer to its operating region but at a higher pressure ratio than was experimentally verified. These results show that none of the modeled conditions yielded a solution that placed both compressors on the respective operating maps in the parallel configuration.

4.4.1.2. EC1 Configuration Results

Figure 4-7 shows the results of the compressor analysis with inputs from Table 4-3 and the electric compressor and turbocompressor in series (EC1). This configuration placed the electric compressor as stage one with the turbocompressor following as stage two. The operating points of the turbocompressor are shown in green and the electric compressor points are shown in yellow.

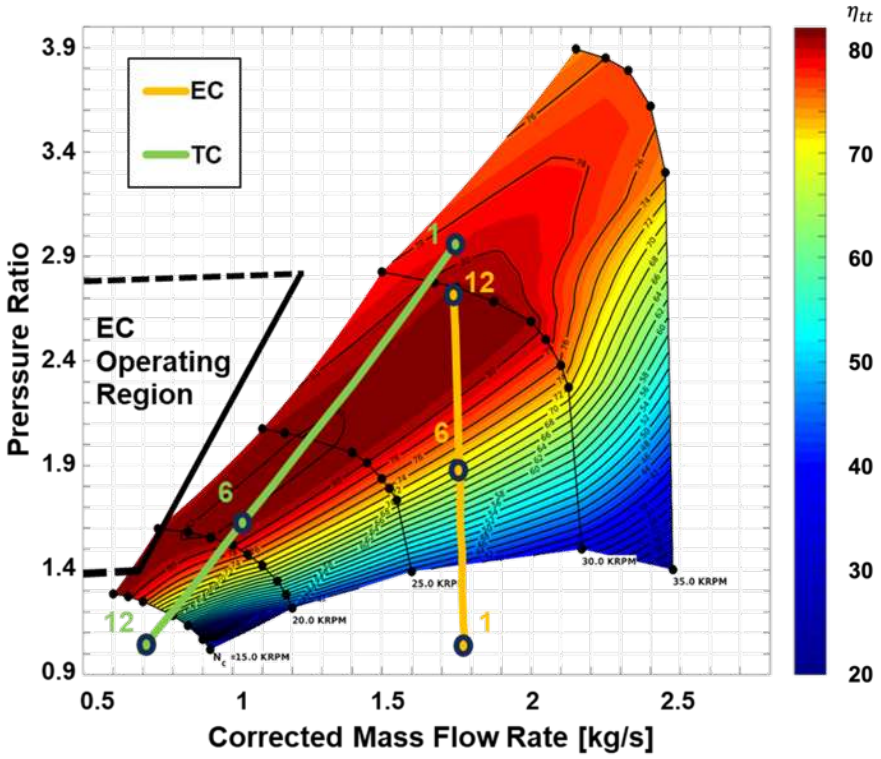

Figure 4-7: Compressor analysis results for design point conditions with the compressors in configuration EC1. In this series configuration, the corrected mass flow rate for the turbocompressor was altered due to variable electric compressor discharge pressure, which moved its operation left on the map.

In this configuration, the two compressors each provided a portion of the total pressure ratio while operating with the same mass flow rate. This caused the operating point of the first stage device to move in the y-direction on the map as the pressure ratio changed and the mass flow rate stayed the same. For example, at point 1 (100% heat input), the electric compressor provided very little of the compression lift, operating at a pressure ratio of 1.1. At point 12 (0% heat input), the electric compressor provided the full pressure lift with a pressure ratio of 2.7. Both points corresponded to a corrected mass flow rate of 1.75 kg s^{-1}, which yielded the vertical yellow line representing the electric compressor in Figure 4-7. However, the changing inlet conditions for the second stage compressor caused a variable corrected mass flow rate (from Equation 10) for the turbocompressor, adding the variability in the x-direction shown in Figure 4-7. The elevated pressure at the suction of the second stage compressor caused the fluid density to increase, which decreased the corrected mass flow. Therefore, as the first stage (the electric compressor in this case) increased power and delivered more of the compression load, the second stage (the turbocompressor in this case) moved down (due to a lower share of the total pressure ratio) and to the left (due to increased pressure and fluid density at the suction) on the map. At point 1 (100% heat input), the turbocompressor suction conditions we not impacted by the electric compressor (due to the low 1.1 pressure ratio across the electric compressor). This resulted in a minimal impact on the corrected mass flow rate, with the corrected value near 1.75 kg s^{-1}. However, at point 12 (0% heat input), the high pressure ratio across the electric compressor (2.7), had a significant impact on the suction conditions for the turbocompressor. The increased pressure and associated density caused the corrected mass flow rate for the turbocompressor to decrease to 0.7 kg s^{-1} despite no change in the uncorrected mass flow rate.

For this simulation, the turbocompressor remained within the operating map for all but the final, low heat availability, modeling condition (point 12, 0% heat input). However, the electric compressor was far to the right of the operating region for the entire set of conditions, meaning that the flow through the electric compressor was choked. In this configuration, again, none of the modeled conditions simultaneously placed both compressors within the operating regions.

4.4.1.3. TC1 Configuration Results

The final configuration, TC1, placed the compressors in series with the turbocompressor first in the flow path. Figure 4-8 shows the results of this analysis. Again, the operating points of the turbocompressor are shown in green and the points for the electric compressor are shown in yellow.

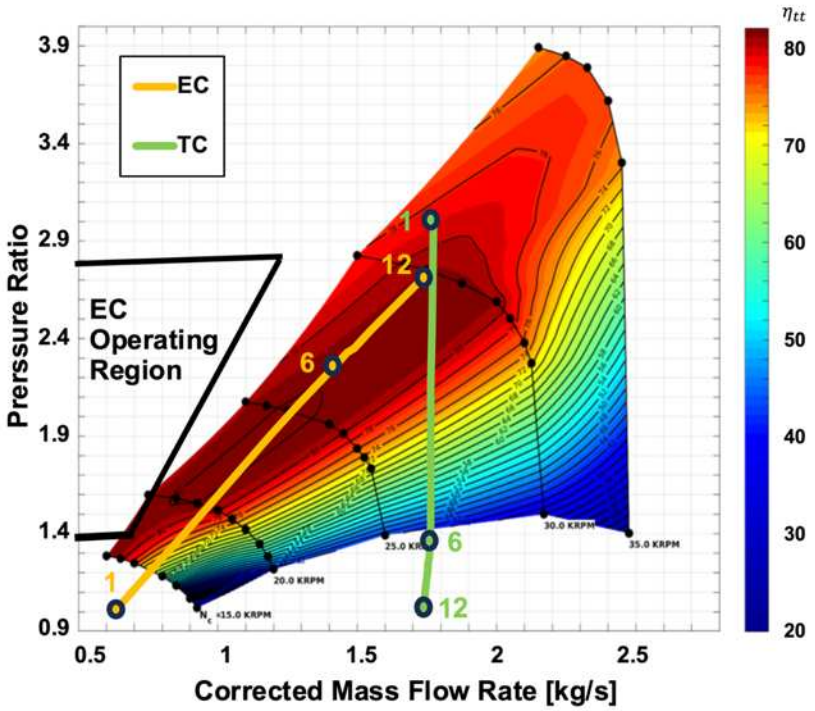

Figure 4-8: Compressor analysis results for design point conditions with the compressors in configuration TC1. This configuration placed the electric compressor closer to the operating map, but it still operated in the choke region for all the modeled conditions.

In this configuration, a similar trend was present as the one shown in Figure 4-7. However, for this configuration the turbocompressor operated as stage one and the electric compressor was stage two. In this case, the corrected mass flowrate stayed constant for the turbocompressor as the pressure ratio changed, yielding the vertical green line in Figure 4-8. The electric compressor experienced a variable corrected mass flow rate due to changing inlet pressure as discussed previously, which yielded the sloped yellow line shown in Figure 4-8. The slope change between Point 6 and Point 12 is a result of reaching the 40% isentropic efficiency interpolation constraint for the turbocompressor as the operating point moved off the bottom of the compressor map. As the first stage device in the TC1 configuration, the isentropic efficiency of the turbocompressor impacted the operation of both compressors, driving the slope shift observed in the results for both devices. This compressor configuration (TC1) placed the electric compressor closer to its operating region than the EC1 configuration. However, it was still outside of the operating region in the choke zone for all the modeled conditions. Therefore, this configuration, again, did not yield any solutions that placed both compressors on the operating maps simultaneously.

To move the electric compressor into its operating region, the operating points needed to be moved to the left on the map by reducing the mass flow rate through the compressors. This reduction was achieved by reducing the desired cooling capacity. A reduction in capacity from 264 kW to 175 kW brought the cooling cycle mass flow rate down to 1.05 kg s^{-1} from 1.58 kg s^{-1}. This reduced the corrected mass flow rate across all the modeled conditions for both compressors. The resulting effect on the operating points for both machines is shown in Figure 4-9. These results are for the compressors in the TC1 compressor configuration.

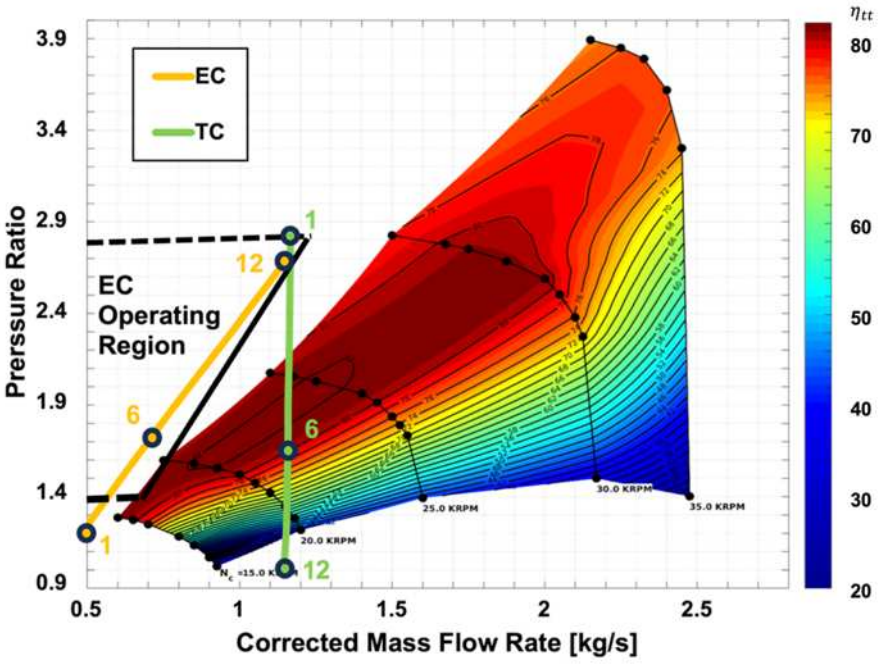

Figure 4-9: Compressor analysis results for 175 kW cooling capacity with the compressors in configuration TC1. At this capacity, both compressors were within the operating regions for many of the modeled conditions.

These new conditions placed the electric compressor on its choke line (i.e., the right edge of the operating region) at the highest electric compressor pressure ratio. Any further reduction in mass flow rate, and the turbocompressor operating region got smaller. At these conditions, the turbocompressor map extended from a pressure ratio of 1.2 up to a pressure ratio of 2.2. This range decreased with any further decrease in mass flow rate. At higher mass flow rates (farther right on the map), the higher pressure ratios were choked for the electric compressor. In these new, optimized operating conditions, the turbocompressor was on the operating map between pressure ratios 1.2 and 2.2. The electric compressor was within the operating region from pressure ratio 1.4 up to 2.8. This was the first compressor configuration and set of conditions that yielded operating points within the operating region for both compressors.

The analysis was extended to the turbine to confirm operability under reduced cooling load. Figure 4-10 shows these results plotted on the turbine performance map. Under conditions with

more heat available (points 1 – 6), the turbine was in the heart of its operating map. As heat availability dropped to zero (point 12), the turbine moved off the map due to low mass flow rate. This was consistent with the results for the thermal compressor with both devices placed off the operating map at low levels of heat input.

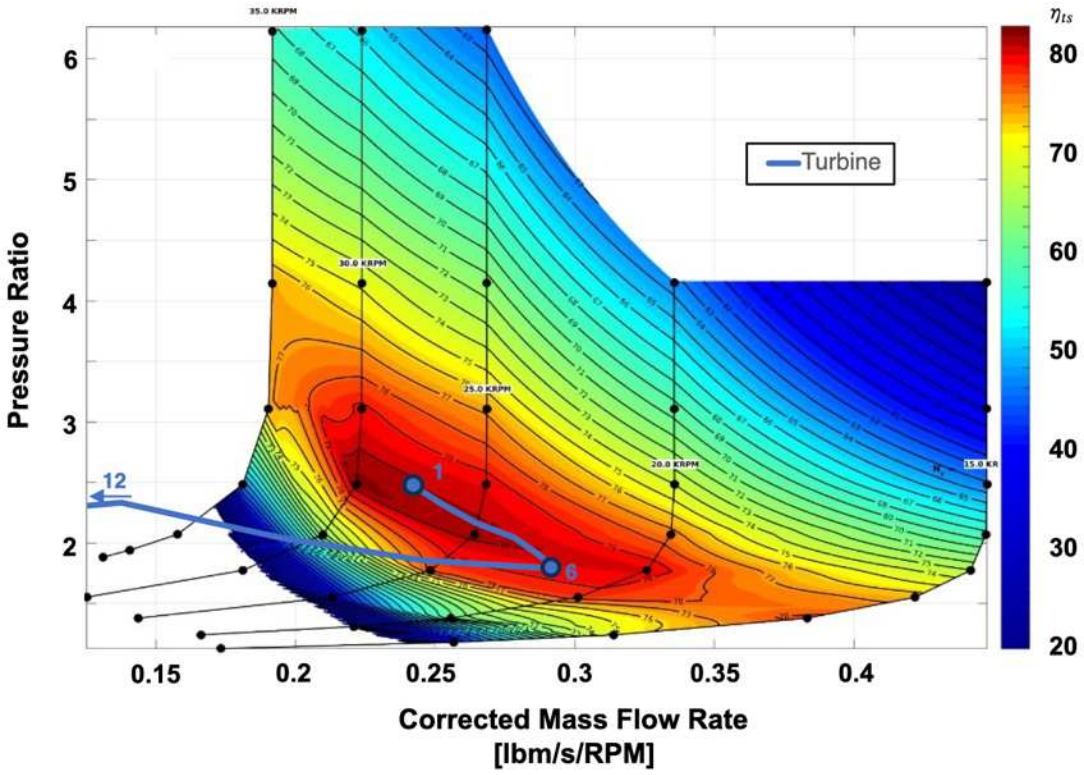

Figure 4-10: Turbine analysis results for 175 kW capacity with the compressors in configuration TC1. The turbine operated within the center of the map for all but the lowest heat input conditions.

Based on these simulation results, the system was unlikely to operate at the original design point conditions in any of the potential compressor configurations. This was due to the sizing/operating fluid mismatch between the two devices. However, with the operating capacity reduced from 264 kW to 175 kW, the model predicted that there was a configuration that would operate successfully under some of the modeled conditions. Modifying the operating capacity enabled system performance evaluation without moving away from industry standard rating conditions.

4.4.2. Design Point Performance Results with Variable Heat Supply

When modeled at 175 kW capacity in the TC1 compressor configuration, the model yielded solutions for a range of heat supply values that quantified the performance of the system under design point operating conditions. Figure 4-11 shows the electric and thermal COP of the system when modeled at design point operating conditions with heat input ranging from 0.0 kW to 409 kW. Thermal COP is plotted using circles, against the left axis and electric COP is plotted with diamonds, against the right axis. Points marked with an X represent conditions where one or more of the turbomachines operated outside of its operating region.

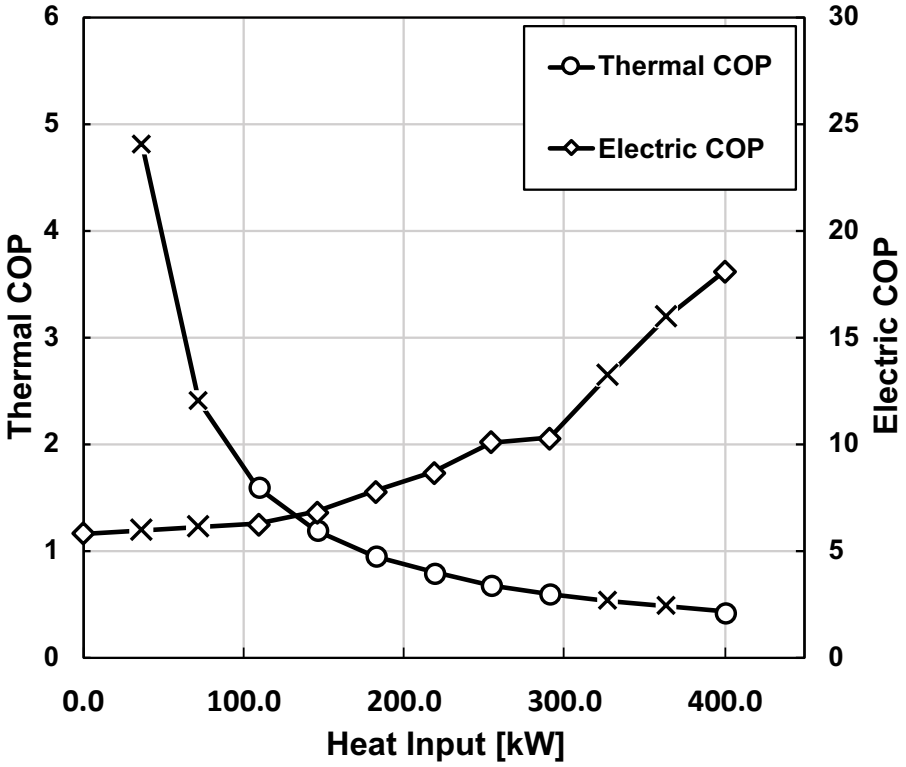

Figure 4-11: System performance at optimized design point conditions. Points marked with an X represent conditions where one or more of the turbomachines was outside of its operating region.

With no thermal input, the system operated in electric cooling mode with the electric compressor providing all the compression load. At this point, the electric COP was 5.86. Thermal COP was not calculated at this condition as there was no thermal input. As heat input rose, the

system shifted into hybrid operation with both compressors delivering a portion of the compression load. The thermally driven compressor was below the operating map, in the choke region, until the thermal input reached 100 kW. At 109 kW, the electric COP was 6.28 and the thermal COP was 1.60. As heat input continued to rise, the system operated with all three turbomachines within the operating maps until the thermal input reached 327 kW. Across this range, the electric COP steadily increased to 13.3 and the thermal COP decreased to 0.53. With heat input above 327 kW, the thermal compressor was above the operating map in the surge region. The electric compressor was off the bottom of the map, in the choke region, at this condition. Once thermal input reached 409 kW, the system shifted into thermal cooling mode and the electric compressor no longer provided any input to the system. The thermal compressor delivered all the necessary compression power, and the system operated with a thermal COP of 0.44 and an electric COP of 18.2.

The shifting of load between the electric and thermal compressors was visible in the temperature-entropy diagrams of the system when operating with different levels of heat input. Figure 4-12 shows two different temperature-entropy diagrams, one with 291 kW of heat input and one with 146 kW of heat input. The compression process delivered by the electric compressor is highlighted in grey on the right side of each map. The length of the electric compressor process relative to the length of the total compression process indicated the share of the load that the electrically powered device was contributing. With 291 kW of thermal input the electric compressor process was relatively short. At this condition, the electric compressor was providing 33% of the total compressor work. With heat input reduced to 146 kW, the electric compressor process was longer, representing 68% of the total compressor work.

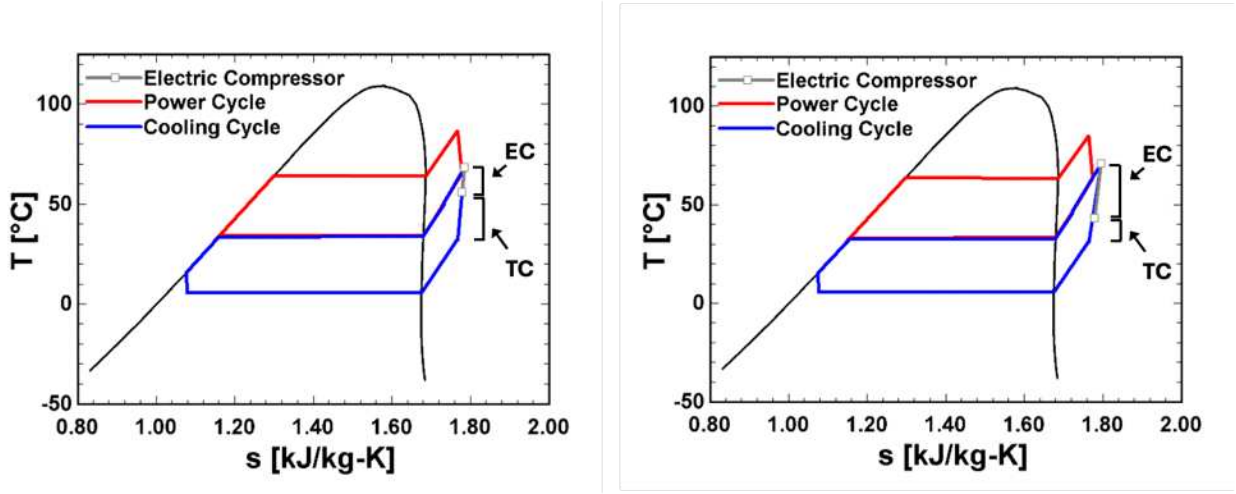

Figure 4-12: Temperature – entropy diagrams of the system at high heat input (291 kW – left) and low heat input (146 kW – right).

4.4.3. Parametric Model Results

The model was also used to perform three parametric studies on the hybrid ORVC system. The parametric analysis quantified the performance of the system as operating conditions moved away from design point conditions. Three heat source or sink temperatures were of critical importance on the operation of the ORVC system: heat input temperature, chilled water delivery temperature, and condenser water temperature. A parametric study was performed on each of these temperatures to understand their impact on the operation and performance of the hybrid ORVC concept.

For the boiler supply temperature parametric analysis, all inputs other than heat input temperature were set to the design point values in

Table **4-3**, with the chilling duty modified to 175 kW. The heat input temperature was varied from 85°C to 120°C. The quantity of heat input was set at 250 kW to maintain a balance between the electric and thermal compressor. Since heat input and cooling duty were defined for this study, thermal COP remained constant across the range of heat input temperatures. Electric

COP was therefore the metric used to evaluate system performance. Figure 4-13 plots the electric COP against the range of heat input temperatures evaluated.

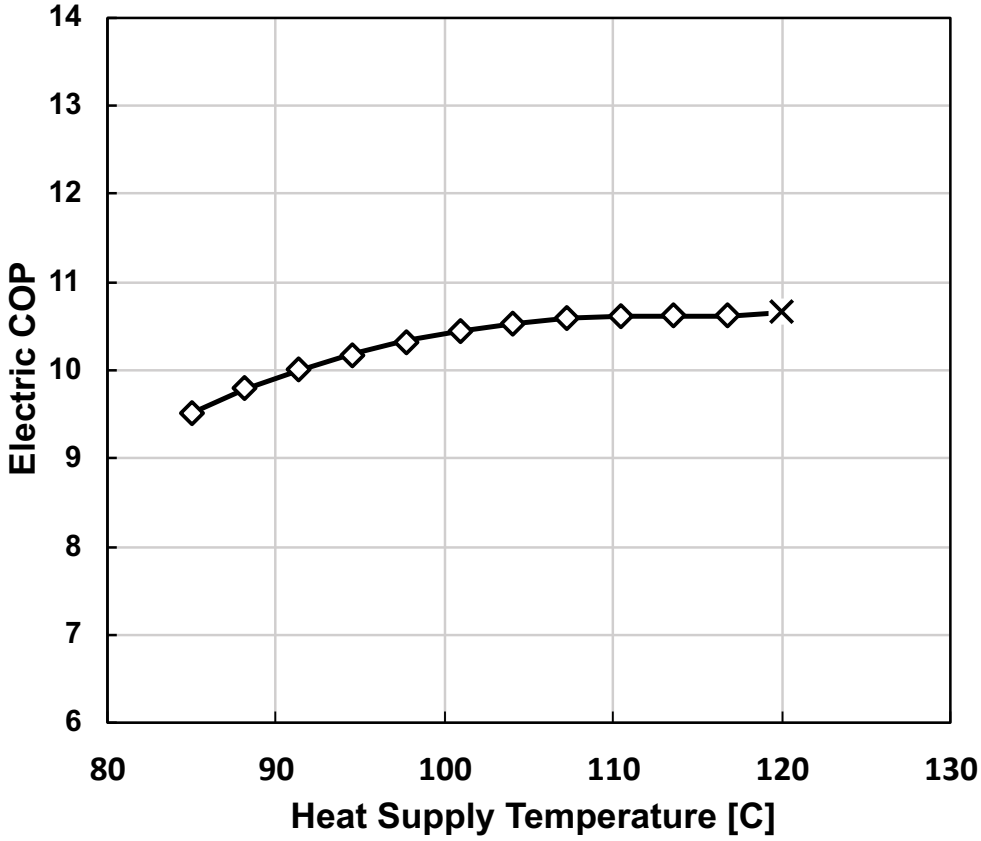

Figure 4-13: System performance with heat supply temperature ranging from 85°C to 120°C. Points marked with an X indicate conditions that placed one or more of the turbomachines outside of the operating region.

As heat input temperature rose, the performance of the system generally improved. At 85°C, the electric COP was 9.5. The electric COP increased steadily to 10.6 when the heat input temperature was 110°C. This was due to improved ORC performance. Increased heat input temperature increased the boiler saturation pressure and increased the pressure ratio across the turbine. This yielded more turbine power and greater ORC efficiency. At 85°C, the turbine power was 14.8 kW and the ORC efficiency was 4.8%. At 110°C, the turbine power was 19.9 kW and the ORC efficiency increased to 6.5%. Above 110°C, the electric COP changed very little. At this

point the isentropic efficiency of both compressors decreased, bringing the COP of the VCC down. At 110°C, the electric compressor isentropic efficiency decreased to 56% from 67% at 85°C. Similarly, the thermal compressor isentropic efficiency was down to 82% from 88% at 85°C. Below 110°C, the COP of the cooling cycle was between 5.5 and 5.8. Above 110°C, the COP of the vapor compression cycle dropped, decreasing to 5.1 at 120°C. The reduction in cooling cycle performance counteracted any increase in power cycle efficiency, leading to no change in system COP above 110°C. When the heat input temperature reached 120°C, the load on the electric compressor became low enough that the device moved off the bottom of the operating region due to low pressure rise across the compressor. Variations in heat input temperature did not have a large impact on the performance of the system. Across the entire range of heat input temperatures there was a COP change of only 12%.

The second parameter investigated was the temperature of the chilled water delivered by the system. In this parametric study, model inputs were held at design point values for all parameters except for the chilled water delivery temperature. The chilled water delivery temperature was varied from 2.1°C to 21.1°C. Heat input was held at 250 kW to maintain balanced, hybrid system operation. Thermal COP was fully fixed in this analysis, so electric COP was examined to understand system performance. Figure 4-14 presents system performance results from this simulation study.

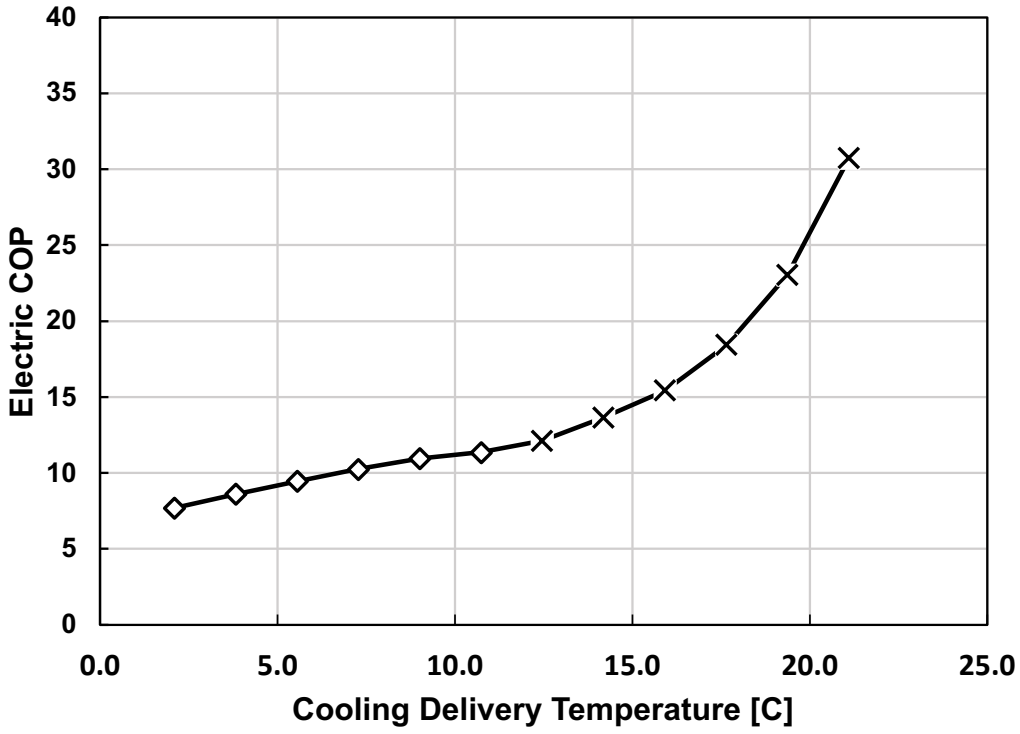

Figure 4-14: System performance with cooling delivery temperature ranging from 2.1°C to 21.1°C. Points marked with an X indicate conditions that would cause at least one of the turbomachines to be placed outside of their operating region.

The system operated with all the turbomachines on the operating maps when chilled water was delivered at 2.1°C. At this condition, the electric COP was 7.7. The electric COP steadily increased as chilled water delivery temperature increased. Electric COP reached 11.4 when the chilled water delivery temperature was 10.7°C. As chilled water delivery temperature increased, the saturation pressure in the evaporator increased. This reduced the pressure ratio across the compressors and reduced the amount of work that was required to compress the same flow rate of refrigerant. This effect was clear in the reduction of total compressor power required to achieve the specified cooling duty. When the chilled water delivery temperature was 2.1°C, the total compressor power required to deliver 175 kW of cooling was 36.6 kW. When the chilled water delivery temperature was 10.7°C, the total compressor power required decreased to 27.6 kW. Above 10.7°C, the load on the electric compressor decreased to the point where the device dropped

off the bottom of the operating region. This represents the choke region for the electric compressor and the device fails to operate under these conditions. At this point, the thermal compressor provided most of the compression load and operated with a pressure ratio of 1.79. The total pressure ratio across both compressors at this condition was just 2.42, due to the increased chilled water temperature and associated elevated evaporator saturation pressure. At this point, the electric compressor had a pressure ratio of 1.35. This was below the lower pressure ratio limit of 1.4 on the electric compressor operating region.

The operation of the power cycle was not significantly impacted by variation in chilled water delivery temperature. When the chilled water delivery temperature was 2.1°C, the ORC efficiency was 5.6%. At 10.7°C, the ORC efficiency was 4.9%. This slight reduction was due to reduced heat duty across the cross-cycle recuperative economizer. With lower compressor load at 10.7°C chilled water temperature, there was less excess superheat available for use in the power cycle. This reduced ORC performance, but the effect was not large enough to significantly impact overall system performance. Despite this, the impacts on the operation of the vapor compression cycle show that variations in chilled water temperature had a more significant impact on the operation of the system when compared with the variable heat input temperature simulations. Over the range of temperatures evaluated, the electric COP changed by nearly 300% and many of the conditions had enough impact to place turbomachines outside of their respective operating regions. The final parametric study examined the effect of heat rejection or condenser water temperature on the operation of the system. All model inputs were set to their design point values while the condenser water inlet temperature was varied from 21°C to 31°C. Heat input was held at 250 kW to balance the compression load between the electric compressor and the thermally driven device.

Figure 4-15 presents the system performance results for this variable heat rejection temperature study.

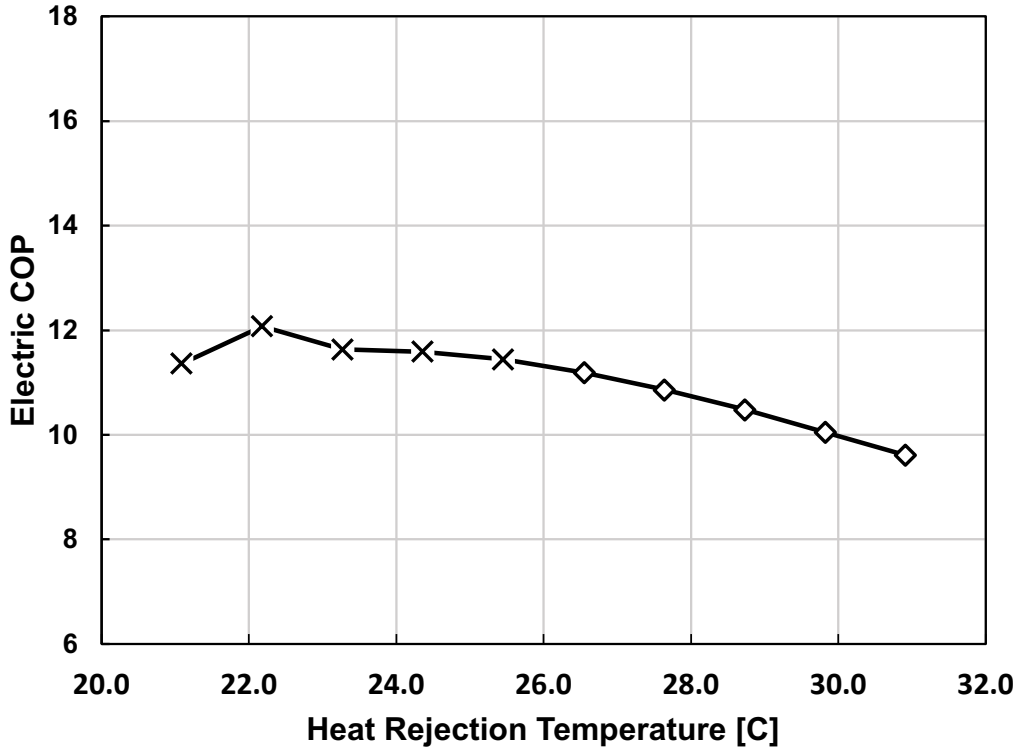

Figure 4-15: System performance with heat rejection temperature ranging from 21°C to 31°C. Points marked with an X indicate conditions that placed one or more of the turbomachines outside of the operating region.

At low condenser water temperatures, the pressure ratio was low because the evaporator saturation temp and the condenser saturation temperature were very close together (5.7°C and 31.9°C). Pressure ratios of below 1.4 occurred at these conditions, which placed the electric compressor off the bottom of the operating map into the choke region. When the condenser water temperature reached 26.6°C, the pressure ratio for the electric compressor increased above 1.4, which brought the device into the operating region. At this temperature the electric COP was 11.2. The system operated with all turbomachinery on the operating map as the condenser water

temperature increased to 30.9ºC. As the condenser water temperature increased from 26.6ºC to 30.9ºC, the electric COP steadily declined, falling to 9.61 when the condenser water was 30.9ºC.

These performance impacts are driven by changes in the operation of both cycles. As condenser water temperature increased, the pressure ratio across the turbine decreased. This reduced the power produced by the device and negatively impacted the efficiency of the ORC. When condenser water was 26.6ºC, the ORC efficiency was 5.5%. This dropped to 5.1% when the heat rejection temperature increased to 30.9ºC. The performance of the cooling cycle was also impacted. As condenser water temperature increased, the saturation pressure inside the condenser increased. This increased the total pressure ratio across both compressors, increasing the amount of power required to deliver the 175-kW cooling duty. However, the performance of the compressors also changed simultaneously. The isentropic efficiency of both compressors was higher when the heat rejection temperature was higher. When the condenser water was 26.6ºC, the electric compressor isentropic efficiency was 57% and the thermal compressor isentropic efficiency was 87%. When the heat rejection temperature was 30.9ºC, the isentropic efficiencies for the electric and thermal device were 70% and 88%, respectively. These competing effects led to an interesting result for the cycle performance. When the heat rejection temperature was 21.1ºC, the COP of the cooling cycle was 5.45. This metric increased to 5.99 when the condenser water was 26.6ºC and then decreased to 5.68 when the heat rejection temperature reached 30.9ºC.

Despite these effects, the impact of variable condenser water temperature was not as strong as that of variable chilled water delivery temperature. The total electric COP change across the range of condenser water temperatures was only 26%. However, there was enough impact from variability in this temperature to place turbomachines outside of their operating region for half of the modeled points.

4.4.4. Integrated Part Load Value Model Results

Since cooling equipment often operates at lower than rated load, the integrated part-load value (IPLV) is often used to calculate the average performance of a cooling device at relevant operating conditions. [56]. These conditions include design and off-design conditions with the chilled water heat duty and condenser glycol inlet temperature being adjusted to represent low-load conditions. The hybrid ORVC system was simulated at IPLV conditions to quantify this part-load performance. Heat supply for this simulation was varied from 300 kW down to 100 kW in equal increments. This maintained balanced, hybrid operation (the electric compressor provided 36%-37% of the total compressor work for all the successful simulations) while scaling linearly in a similar manner to the linear reduction in cooling duty. Table 4-4 shows the IPLV simulation parameters.

Table 4-4: Modeling conditions for the IPLV study.

Modeling Condition (% Load)	Boiler Inlet Temperature [°C]	Heat Supply [kW]	Chilled Water Temperature [°C]	Chilling Duty [kW]	Condenser Inlet Temperature [°C]
1 (100%)	91.0	300	6.7	175.0	30.0
2 (75%)		233		131.3	24.5
3 (50%)		167		87.5	19.0
4 (25%)		100		43.8	19.0

The model results for the IPLV simulations are shown in Figure 4-16. All three devices were within their operating regions for the 100% load point. However, as the load decreased, the cooling cycle flow rate dropped, which shifted the operating points of both compressors off the left side of the map. At the 75% loading condition, the thermal compressor operated with a pressure ratio of 1.98. At this pressure ratio, the lower corrected mass flow rate limit on the operating map was 1.05 kg/s. At the 75% IPLV condition, the corrected mass flow rate for the device was 0.85

kg/s. Similarly, for the 50% IPLV simulation, the lower limit on the operating map for the corrected mass flow rate was 0.90 kg/s. At 50% load, the corrected mass flow rate for the thermal compressor was 0.57 kg/s. This placed the operating points for the device well left of the operating map, into the surge region, for both the 75% and 50% load simulations. The electric compressor results showed a similar leftward shift as cooling duty decreased. However, the corrected mass flow rates for the 100%, 75%, and 50% IPLV simulations all remained within the acceptable range for the device. The low pressure ratio results from the simulations proved to be the parameter that shifted the operating point outside of the map for the device. The electric compressor had a lower pressure ratio limit of 1.4 that remained constant across the bottom of the map. The electric compressor pressure ratio for the 100%, 75%, and 50% IPLV conditions was 1.31, 1.28, and 1.44, respectively. This placed the operating point for the device off the bottom of the map, into the choke region, for both the 100% and 75% IPLV simulations. The operating points for the turbine remained within the turbine map for all three cases. The 25% IPLV case was unable to be successfully simulated. This set of conditions led to a series of errors that prevented a solution to the model from being reached. This was due to the extremely low mass flow rates required to deliver 25% cooling duty.

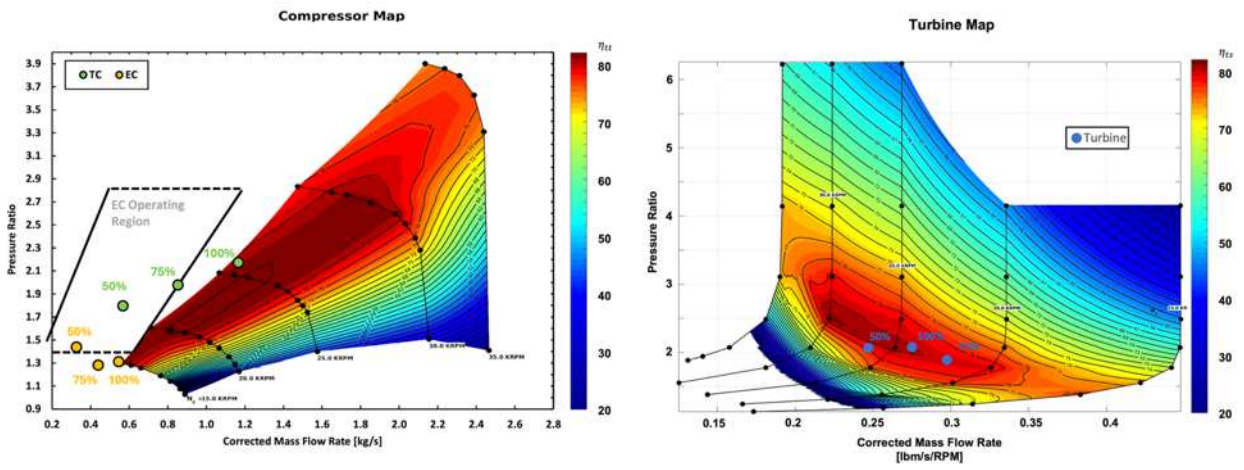

Figure 4-16: Compressor and turbine analysis results for IPLV modeling conditions. None of the IPLV operating conditions yielded solutions that placed all three turbomachines on the operating maps.

4.4.5. System Improvements

Throughout the design point and off-design results, the mismatch between the thermally driven compressor and the TT300 electric compressor had a negative impact on the operating range and performance of the system. These limitations can be remedied by selecting compressors that have more closely aligned design points and operating regions. Results from the experimentally based TT300 model discussed in previous sections were used to inform the selection of a hypothetical electric compressor for the hybrid ORVC system. The hypothetical electric compressor was chosen to be a device with higher mass flow rate capacity and an operating range that more closely matched the operating range of the thermally driven compressor examined in this work. Specifically, the acceptable mass flow rates of the electric compressor were increased by 1.0 kg s^{-1} from the values observed in the TT300 experiments. The full analysis was performed on the updated system to quantify the system-wide performance benefits of the improved compressor selection. Model results for the EC1 compressor configuration were applied to the larger-sized compressor, yielding the compressor map presented in Figure 4-17.

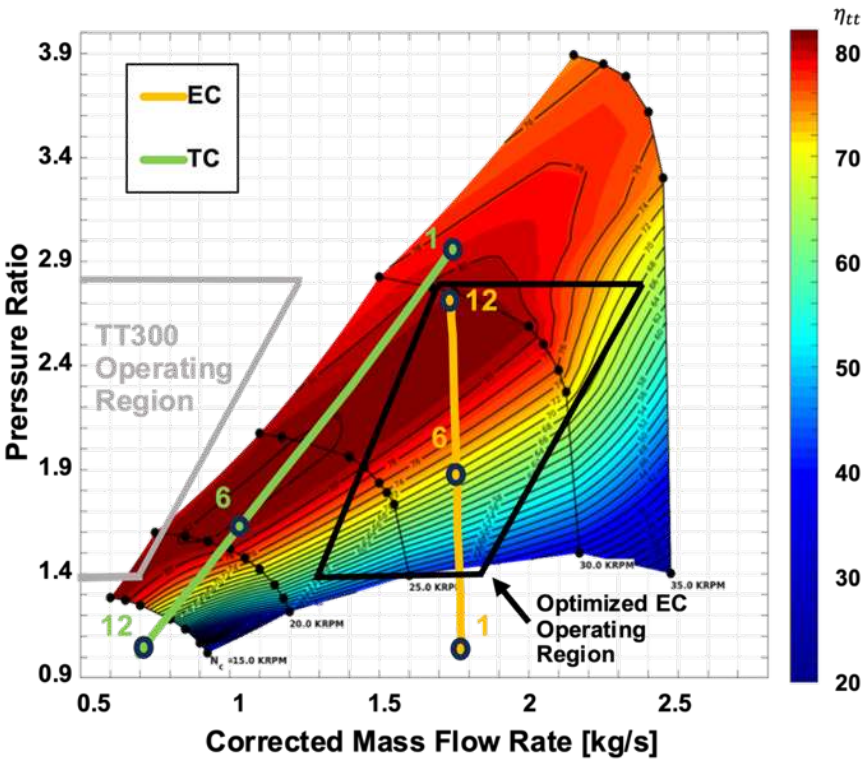

Figure 4-17: Turbomachinery model results for the EC1 configuration with an optimized electric compressor.

This configuration and operating conditions required the original TT300 compressor to operate in the choke region, and as a result the system was simulated at a reduced capacity of 175 kW (50 tons). However, the optimized electric compressor operated at the original design point capacity of 263.8 kW (75 tons) across the full range of heat input conditions, except when the electric compressor pressure ratio was less than 1.4. This low pressure ratio only occurred when heat input was above approximately 350 kW, and the thermally driven compressor was delivering the majority of the pressure rise. The turbocompressor operated at or near the highest efficiency region of the operating map for the full range of modeled conditions until the heat input decreased to 175 kW and the pressure ratio dropped below 1.4. The operating point for the thermally driven device only shifted entirely off the map when heat input dropped below 100 kW and the pressure ratio decreased below 1.2. Considering the operating regions of both devices, the new

configuration enabled the compressors to operate on the respective maps for 8 of the 12 sets of operating conditions.

The optimized electric compressor impacted the system performance as well as the operating range. By enabling operation at the design point capacity of the turbocompressor (263.8 kW, 75 tons), the performance of the system improved. Figure 4-18 shows the thermal and electric COP results for the system with the optimized electric compressor.

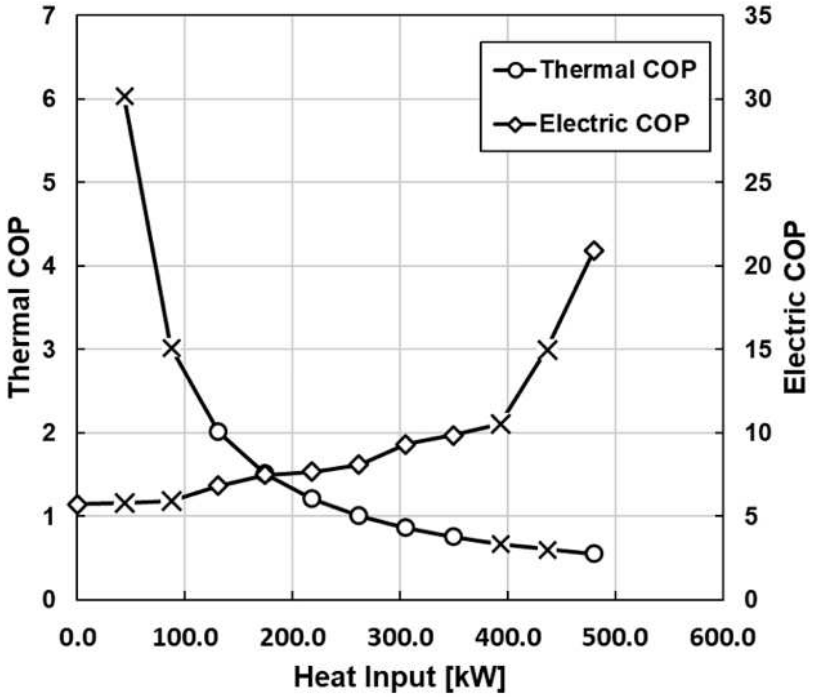

Figure 4-18: System performance with optimized electric compressor in the EC1 configuration at full capacity. Points marked with an X represent conditions that placed one or more turbomachines outside of the operating region.

Operating at full capacity improved the system performance compared with the reduced capacity results discussed in previous sections. In fully thermal operation with 480 kW of heat input, the system operated with a thermal COP of 0.55 and an electric COP of 21. As heat input decreased, the system shifted into hybrid operation but was unable to operate until the pressure ratio across the electric compressor reached 1.4. Below 1.4, the electric compressor was out of its

operating region. The electric compressor pressure ratio reached 1.4 when the heat input decreased to 350 kW. At this point, the thermal COP was 0.76 and the electric COP was 9.9. The system operated with both compressors on the operating maps until the heat input dropped to 100 kW. Across this range, the thermal COP increased to 2.0 and the electric COP decreased to 6.8. With heat input below 100 kW, the pressure ratio across the turbocompressor decreased below 1.2, which moved it off the bottom of the operating map. This prevented system operation until the heat input reduced to zero and the system operated on fully electric input. At this condition, the thermal COP was not calculated as there is no thermal input, and the electric COP was 5.7.

These results represented a notable improvement over results obtained with the Danfoss TT300 compressor. At fully thermal operation, thermal COP with the TT300 was 0.44. The optimized electric compressor yields an 25% performance improvement. In hybrid operation with 70% of the work coming from the electric compressor, the optimized compressor enabled a 13% improvement in electric COP with no change in thermal COP. The properly sized compressor enabled higher capacity operation for the system while improving the performance for a wide range of operating conditions. These performance improvements highlight the importance of appropriate compressor selection for this concept.

4.4.6. Comparative Analysis

Key performance results from this work were compared with the performance reported in previous literature to understand the comparative performance of the hybrid ORVC configuration presented in this work and provide a level of validation to the simulation results. Jiang et al. experimentally achieved a thermal COP of 0.70 and an electric COP of 6.07 while delivering 14.2 kW of cooling. Cooling was delivered at 19.4^{o}C and heat was supplied at 71.9^{o}C. The ORC condenser temperature was 30.2^{o}C and the VCC condenser temperature was 28.5^{o}C. While no

simulations in this work were performed at similar conditions, a similar thermal COP of 0.69 was achieved under design conditions when the heat input was 255 kW and the electric COP was 10.1. This result compares favorably to the results presented by Jiang et al. with the electric COP being significantly higher. However, the heat supply temperature used in this work was notably 18.1°C higher than the value presented by Jiang et al. and the cooling delivery temperature was 12.4°C lower for this work. These two differences have conflicting effects on the performance of the system: the higher heat supply temperature likely improved performance while the lower cooling delivery temperature likely reduced performance relative to the results achieved by Jiang et al. It is therefore difficult to make direct performance comparisons between the two works. However, the similarity of the results of each study provides some validation to the simulation results presented in this research.

4.5. Chapter Summary

In this chapter, simulation methods and results were presented for the hybrid ORVC system. The coupled thermodynamic and turbomachinery models were developed from experimental data collected from the ORVC test facility. The system was simulated in three different operating modes (thermal, electric, and hybrid), and with three different compressor configurations (PC, EC1, and TC1). Simulations were performed at design point conditions representative for the HVAC industry and at a series of off design conditions to fully capture the system performance.

Key findings indicated that the TC1 compressor configuration mitigated choke limitations by pre-compressing the working fluid with the thermally driven compressor, avoiding the operational constraints of the undersized electric compressor. The system efficiently operated across a wide range of conditions, with hybrid mode outperforming purely thermal or electric

operation. Thermal COP reached 1.6 at peak performance, improving from a baseline of 0.44, while electric COP in hybrid mode peaked at 18.2, significantly higher than the purely electric COP of 5.86. Operating range was also wide in off-design conditions, with large acceptable operating ranges for heat input temperature (85°C-117°C), cooling delivery temperature (2.1°C – 10.7°C), and heat rejection temperature (26.6°C – 30.9°C). The performance of the system was most sensitive to changes in the cooling delivery temperature, with the electric COP varying from 7.7 to 11.4 across the range of temperatures simulated. In the following chapter, the insights gained from the modelling effort presented in this chapter will be evaluated experimentally. The fully integrated test facility will be tested at design point operating conditions to experimentally evaluate system performance.

CHAPTER 5. Experimental Compressor Evaluation and Design Point Performance

This chapter presents experimental validation of the hybrid ORVC system at design point operating conditions. Experimental methodology is discussed to evaluate the three possible compressor configurations and characterize the performance of the system across the full range of heat input values from fully thermal to fully electric operation. Results from the compressor configuration comparison study are presented and discussed using turbomachinery analysis to understand the intricacies of each configuration. System performance results are presented across the range of heat inputs to characterize the potential of the technology at design-point conditions. The content of this chapter is currently under review by Applied Energy in Platt et al. [68].

5.1. Experimental Procedure

Experiments were performed on the test facility in all three of the system's operating modes. Baseline experiments were performed in electric cooling and thermal cooling modes. These tests served to benchmark the performance of the facility when operating as a traditional electric chiller or traditional ORVC system. Once the system performance was benchmarked in non-hybrid operating modes, two studies were performed to evaluate the facility in the novel hybrid cooling operating mode.

The first study was designed to evaluate the three possible compressor configurations: PC, EC1, and TC1. Design point operating temperatures and capacity were held constant for each of the three possible compressor configurations. Each test was conducted with 257 kW of heat input at 91°C. Heat input was set at a medium level to keep the compression load balanced between the two compressors. Cooling was delivered at 9°C with a target capacity of 175 kW. Condenser glycol

inlet temperature was maintained at 30°C. Each configuration was assessed for operability and system performance. The compressor configuration was the only difference between each of the three tests.

The second study performed on the facility was designed to understand how the hybrid configuration performed with variable levels of heat input. The facility was operated at the same design point operating temperatures with heat input at 91°C, condenser glycol inlet at 30°C, and cooling delivered at 9°C. Heat input was ranged from 0.00 kW to 409 kW across 13 different tests. This captured the operation of the facility from fully electric operation to fully thermal operation with 11 different levels of hybrid operation in between. This evaluated the operability and performance of the facility as compression load shifted from the thermally driven device to the electrically driven device. The TC1 compressor configuration was selected for this study. Table 5-1 presents the testing matrix for the variable heat input study.

Table 5-1: Testing matrix for the variable heat input study.

Experiment	*Heat Input [kW]*	*Compressor Configuration*
Test #1	-	Thermal Cooling
Test #2	400	TC1
Test #3	364	TC1
Test #4	331	TC1
Test #5	292	TC1
Test #6	257	TC1
Test #7	218	TC1
Test #8	180	TC1
Test #9	136	TC1
Test #10	113	TC1
Test #11	72.7	TC1
Test #12	36.4	TC1
Test #13	0.00	Electric Cooling

The test facility operating procedure varied for each test depending on the operating mode being evaluated. For electric cooling, as shown in Figure 5-1, flow was started in the auxiliary heat transfer streams for the cooling cycle condenser and the evaporator. After auxiliary flow was confirmed, the electric compressor was slowly ramped up to drive the cooling cycle. Operating temperatures were controlled by variable speed cooling tower fans for the condenser water inlet temperature and a variable flow rate on the simulated cooling load for the chilled water delivery temperature. Once operating temperatures and heat duties were stable at the testing targets, the facility was operated at steady state for ten minutes. Test results represent average values over the ten-minute steady-state operating point.

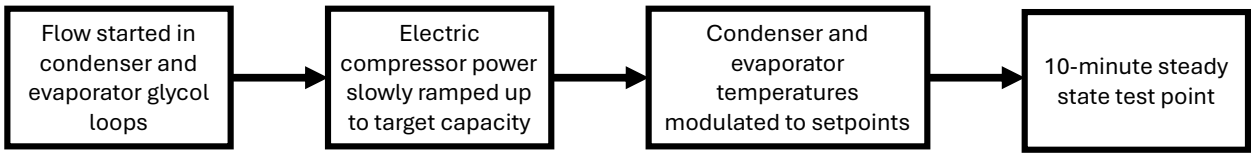

Figure 5-1: Testing procedure for electric cooling mode.

Figure 5-2 presents the more complex testing procedure necessary for operating in thermal cooling mode. In these tests, flow was started in the boiler and condenser auxiliary heat transfer loops first. The power cycle pump was then turned on to 70% speed using a Variable Frequency Drive (VFD) and the flow bypassed the turbine during startup until there was 5^{o}C degrees of superheat at the power cycle boiler outlet. At this point, the pump for the evaporator heat transfer loop was started to circulate fluid through the device. With all three external heat transfer loops operating and superheated vapor at the boiler outlet, flow was sent through the turbine. The mechanical work generated in the turbine spun the thermally driven compressor to drive the cooling cycle. Once temperatures and heat duties had stabilized at the testing targets, a ten-minute steady-state operating point was taken to quantify the performance of the facility.

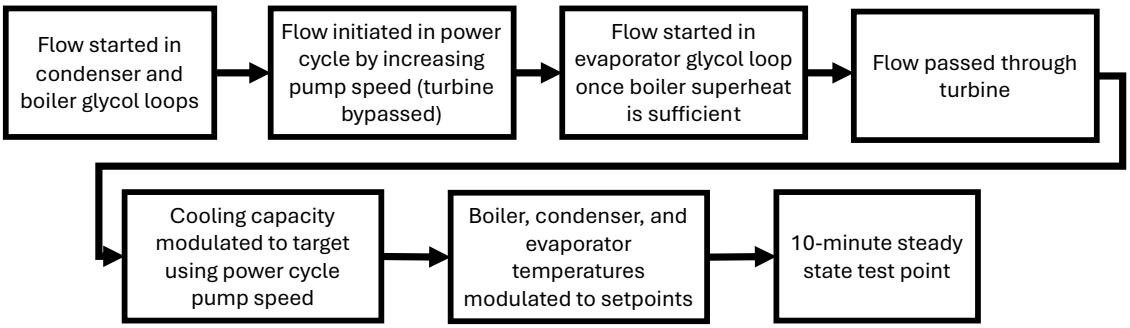

Figure 5-2: Testing procedure for experiments in thermal cooling mode.

Finally, as shown in Figure 5-3 for hybrid cooling mode, the ORC was started up using the same procedure as described for the thermal cooling operating mode. Once superheated vapor had been reached at the boiler outlet and all the external heat transfer loops had been started, the thermally and electrically driven turbomachinery was started simultaneously. Flow was passed through the turbine to spin up the turbocompressor, and at the same time, power was slowly increased to the electric compressor. The flowrate through the ORC was modulated to reach the target heat input level. Once this target was reached, the electric compressor power was manipulated until cooling duty reached the 175 kW design point target. Ten-minutes of time averaged data was collected once operating temperatures and heat duties had stabilized at the testing targets.

Tests were considered stable when criteria based on Air-Conditioning, Heating, and Refrigeration Institute (AHRI) performance rating standards were met [56]. Stability criteria included both flow rate and temperature requirements for the condenser and evaporator auxiliary flows. Temperatures were considered stable when the standard deviation across the ten-minute test was less than 0.25°C. Flow rates were considered stable when the standard deviation was less than 0.75% of the average flow for the test. Stability criteria were reached for all tests except for the test with 292 kW of heat input. In this test, the temperature stability criterium for the evaporator

was not met due to a control limitation of the simulated cooling load. For this test, the evaporator temperature standard deviation was 0.31°C.

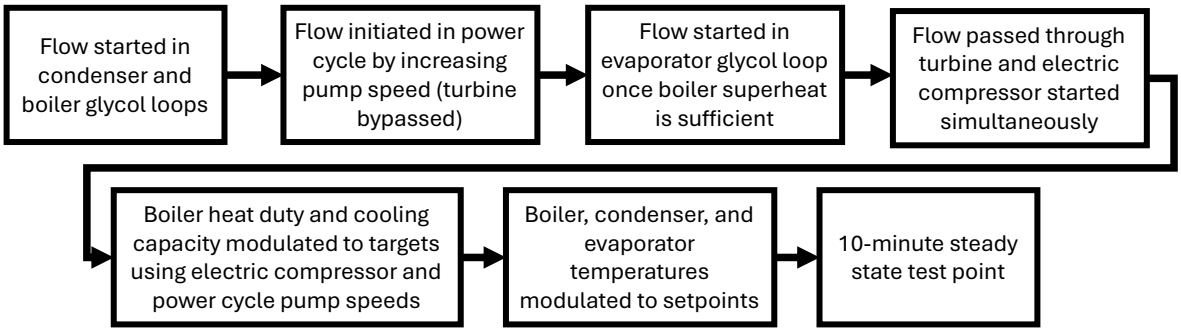

Figure 5-3: Operating procedure for the hybrid cooling mode experiments.

5.2. Data Processing

During each 10-mintue steady state experiment, temperature, pressure, flow rate, and power data were collected from the test facility. Average values were calculated across the steady state test and data processing operations were performed on these averages. Data processing included calculations for refrigerant fluid state points, component heat duties, power levels, and turbomachinery mapping.

Refrigerant fluid state points were constrained using temperature and pressure data from the test facility. In some instances, data from differential pressure transducers was used in conjunction with absolute pressure data to establish absolute pressure at additional locations throughout the system. This enabled the quantification of fluid state at the inlet and outlet of every major component in the facility. Enthalpy and entropy values for each location in the system were calculated from temperature and pressure data using the National Institute of Standards and Technology's REFPROP 10.0 [69,70].

Component heat duties were calculated from the specific heat and temperature change of the auxiliary heat transfer stream. Equation 5-1 defines this calculation.

$$\dot{Q} = \dot{m}_{\text{ext}} * c_{\text{p}} * \left(T_{\text{ext,o}} - T_{\text{ext,i}}\right) \quad (5\text{-}1)$$

$\dot{Q}$ is the heat duty of the heat exchanger, $\dot{m}_{\text{ext}}$ is the mass flow rate of the external fluid stream, c_{p} is the specific heat capacity of the external fluid, and $T_{\text{ext,i}}$ and $T_{\text{ext,o}}$ are the auxiliary fluid temperatures at the inlet and outlet to the heat exchanger, respectively. Equation 5-1 is formulated for heat exchangers that rejected heat to the auxiliary heat transfer streams. In the cases where heat was absorbed from the external loops, the quantity in the parentheses was formulated as $T_{\text{ext,i}} - T_{\text{ext,o}}$. Constant specific heat, evaluated at the average temperature between the inlet and outlet, was a reasonable assumption for the auxiliary fluid streams, as the specific heats do not change significantly in the relatively small operating temperature ranges of the fluids.

Turbomachinery power values were calculated using refrigerant flow rates and enthalpy values at the inlet and outlet of each device. Equations 5-2 and 5-3 present the formulation for work consuming devices (compressors and pump) and work producing devices (turbine), respectively.

$$\dot{W} = \dot{m}_{\text{r}} * \left(i_{\text{r,o}} - i_{\text{r,i}}\right) \quad (5\text{-}2)$$

$$\dot{W}_{\text{turb}} = \dot{m}_{\text{r}} * \left(i_{\text{r,i}} - i_{\text{r,o}}\right) \quad (5\text{-}3)$$

$\dot{m}_{\text{r}}$ is the mass flow rate of the refrigerant and $i_{\text{r,i}}$ and $i_{\text{r,o}}$ are the enthalpies at the inlet and outlet, respectively.

Compressor mapping analysis was performed using the procedure presented with Equations 4-12 – 4-16 in Chapter 4. Key parameters for this analysis include refrigerant mass flow rate, pressure ratio, and isentropic efficiency. The refrigerant mass flow rate in the cooling cycle was calculated from an energy balance on the cooling cycle condenser, given in Equation 5-4.

$$\dot{m}_{\text{r}} = \frac{\dot{Q}}{\left(i_{\text{r,i}} - i_{\text{r,o}}\right)} \quad (5\text{-}4)$$

Pressure ratio was calculated as the ratio of the pressure at the outlet of the compressor to the pressure at the suction of the device, as shown in Equation 5-5.

$$PR = \frac{p_{\mathrm{o}}}{p_{\mathrm{i}}} \tag{5-5}$$

Finally, the isentropic efficiency, η_{comp}, was calculated using Equation 5-6 where $i_{\mathrm{r,o,s}}$ is the isentropic enthalpy at the outlet of the device.

$$\eta_{\mathrm{comp}} = \frac{i_{\mathrm{r,o,s}} - i_{\mathrm{r,i}}}{i_{\mathrm{r,o}} - i_{\mathrm{r,i}}} \tag{5-6}$$

This data processing procedure provided synthesized results from the experimental data collected from this series of performance tests. The analysis provided insight into how the devices interacted and performed, yielding a greater understanding of the complexities of the hybrid ORVC system.

5.3. Compressor Configuration Comparison Results

5.3.1. PC and EC1 Configurations

Of the three tests in the compressor configuration comparison study, only one set of tests was successfully completed. When the test facility was operated with the compressors configured in parallel (PC) or in series with the electric compressor first in the flow path (EC1), it could not operate at the target conditions. Only the series configuration with the turbocompressor first in the flow path successfully reached the targeted operating conditions.

Figure 5-4 plots compressor results for the PC and EC1 compressor configurations. The operating location of each compressor is shown relative to the operating region for each respective device based on corrected mass flow rate and pressure ratio for each machine. The multicolored operating region is for the turbocompressor, with colors representing the predicted isentropic

efficiency for the device. The operating region for the electric compressor is shown on the left side of the plot, outlined in black lines.

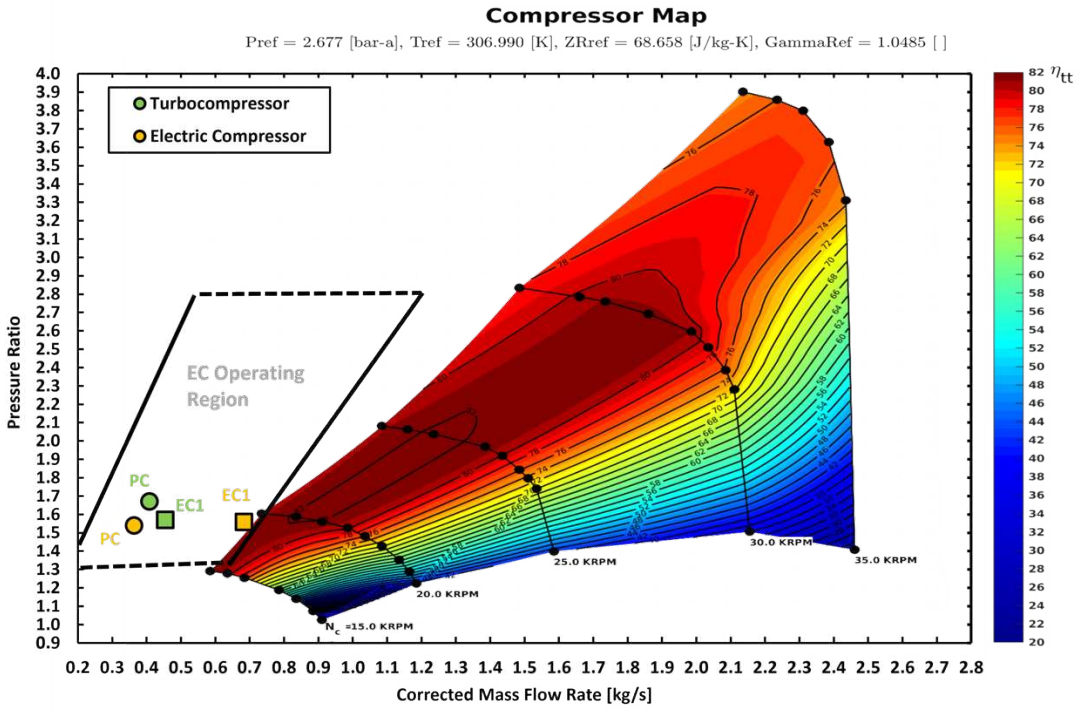

Figure 5-4: Compressor map results for the PC and EC1 compressor configuration tests. These experiments failed to reach target operating conditions due to compressor operating region limitations.

The chilled water delivery temperature posed a particular challenge for operation in the parallel configuration. As the chilled water delivery temperature was decreased towards the target of 9°C, the evaporator pressure dropped to the low suction pressure cutoff limit for the Danfoss TT300 electric compressor. This caused the device to shut down before the testing target could be reached. As a result, the only successful operating point in the parallel configuration was at a higher chilled water delivery temperature. With chilled water being delivered at 17°C, the electric compressor operated within its operating region with a pressure ratio of 1.54 and a corrected mass flow rate of 0.36 kg s^{-1} as shown in Figure 5-4. However, the turbocompressor operated with a pressure ratio of 1.67 and a corrected mass flow rate of 0.41 kg s^{-1} at these conditions. This placed

the turbocompressor outside its operating map and within the surge region. The low flow rate and high pressure rise across the turbocompressor during this test caused aerodynamic stall along the compressor blades, leading to the unstable flow reversal phenomenon known as surge. This was confirmed by audible pulsing from the compressor during testing.

The primary limitation that prevented operation in the parallel compressor configuration was the Danfoss TT300 low suction pressure safety control. This internal safety control provides compressor runaway control and evaporator freeze protection. The low suction pressure limit on the TT300 is set to 262 kPa which correlates to the saturation pressure of R134a at -3°C. This allows for the delivery of near freezing chilled water while allowing for pressure losses between the evaporator and compressor, as well as effectiveness losses within the evaporator. This effectively prevents evaporator freezing and uncontrolled increases in compressor power. However, R134a is a higher-pressure fluid than R1234ze(E). The saturation pressure of R134a at -3°C (262.5 kPa) correlates to a saturation temperature of 5.1°C for R1234ze(E). Therefore, the low suction pressure control that was designed to prevent delivery of chilled water below 0°C with R134a, prevented delivery of chilled water below approximately 8°C with R1234ze(E). The parallel compressor configuration further decreased the suction pressure, with the 262 kPa suction pressure limit being reached when chilled water was delivered at 10°C. As an important safety control, the suction pressure limit could not be adjusted to enable lower chilled water delivery temperatures with R1234ze(E). This was a recurring limitation of the test facility and will be discussed further.

While the suction pressure limitation was the primary driver preventing operation in the parallel configuration, it is a challenge that is easily remedied with improved compressor selection. The surge experienced in the turbocompressor provides experimental evidence of a limitation of

the parallel configuration that is more challenging to resolve. In this experiment, the mass flow through each compressor was relatively balanced, with 0.48 kg s^{-1} passed through the electric compressor and 0.54 kg s^{-1} compressed by the turbocompressor. However, depending on the balance of power between the two devices, the flow through each machine could vary from near 0 kg s^{-1} to near the full cycle flow rate of 1.02 kg s^{-1}. At the pressure ratios observed in this test, approximately 20% of this range is within the operating map for the turbocompressor (0.8 kg s^{-1}-1.02 kg s^{-1}) and about 50% is covered by the electric compressor operating map (0.25 kg s^{-1} – 0.75 kg s^{-1}). The wide range of flow rates that are possible in the parallel configuration pose a challenge to finding operating conditions that place both compressors within the operating maps, as evidenced by the surge conditions observed for the turbocompressor in this test.

In the second experiment, with the compressors configured in series with the electric compressor first in the flow path (EC1), the system was able to operate at the boundary temperature targets. However, the system was unable to deliver the targeted cooling duty of 175 kW. Figure 5-4 shows the compressor operating points for the highest cooling duty that was achieved while operating at the targeted boundary temperatures in the EC1 configuration. At this point, the electric compressor was operating with a pressure ratio of 1.56 and a corrected mass flow rate of 0.68 kg s^{-1}, placing it at the far right of its operating region (the limit of the map at this pressure ratio is 0.70 kg s^{-1}). This indicates a choke condition, at which the mass flow through the machine cannot be increased further due to geometric limitations of the device. On the contrary, the turbocompressor was operating with a pressure ratio of 1.57 and a corrected mass flow rate of 0.45 kg s^{-1}, this was below the minimum flow rate of 0.69 kg s^{-1} for this pressure ratio, placing the device left of the operating region. Similarly to the parallel configuration test, this placed the device in the surge region of the operating map, in which the flow rate was too low for the pressure

ratio across the device. Aerodynamic stall caused flow instability that was observed audibly during the test. The system only delivered 103.6 kW during the test due to the choked operating point of the electric compressor. Internal choke control limited the electric power of the TT300 to 18.2 kW during the test, preventing any further increase in cooling duty.

5.3.2. TC1 Configuration Results

Figure 5-5 shows the compressor map results for the third experiment in the compressor configuration comparison study. With the turbocompressor first in the series configuration (TC1), the facility reached the targeted operating capacity of 175 kW of cooling at 9°C with 257 kW of heat supplied at 91°C and condenser water inlet at 30°C. In this configuration, both devices operated within the bounds of the operating region at the desired operating conditions. The turbocompressor was within the highest isentropic efficiency region of the map, operating at 79.1%. This allowed the facility to deliver 176.0 kW of cooling, which was a higher capacity than what was achievable in the other two configurations. This configuration also avoids the choke limitation in the electric compressor by placing the device after the turbocompressor in the flow path. Partial compression through the turbocompressor increases the pressure of the vapor before it enters the electric compressor. The increased pressure reduced the corrected mass flow rate, $\dot{m}_{\mathrm{eq}}$, allowing the device to flow more mass before choke limitations are reached. This was primarily driven by the δ term defined in Equation 4-15. As $p_{\mathrm{in,a}}$ increased relative to $p_{\mathrm{in,ref}}$, the correction term δ increased. This increased the denominator of the ratio in Equation 4-12, decreasing $\dot{m}_{\mathrm{eq}}$ relative to the actual mass flow rate, $\dot{m}_{\mathrm{a}}$. Therefore, the higher inlet pressure for the electric compressor in the TC1 configuration shifted its operating point left on the compressor map, enabling the higher mass flow rate and cooling capacity observed in this experiment.

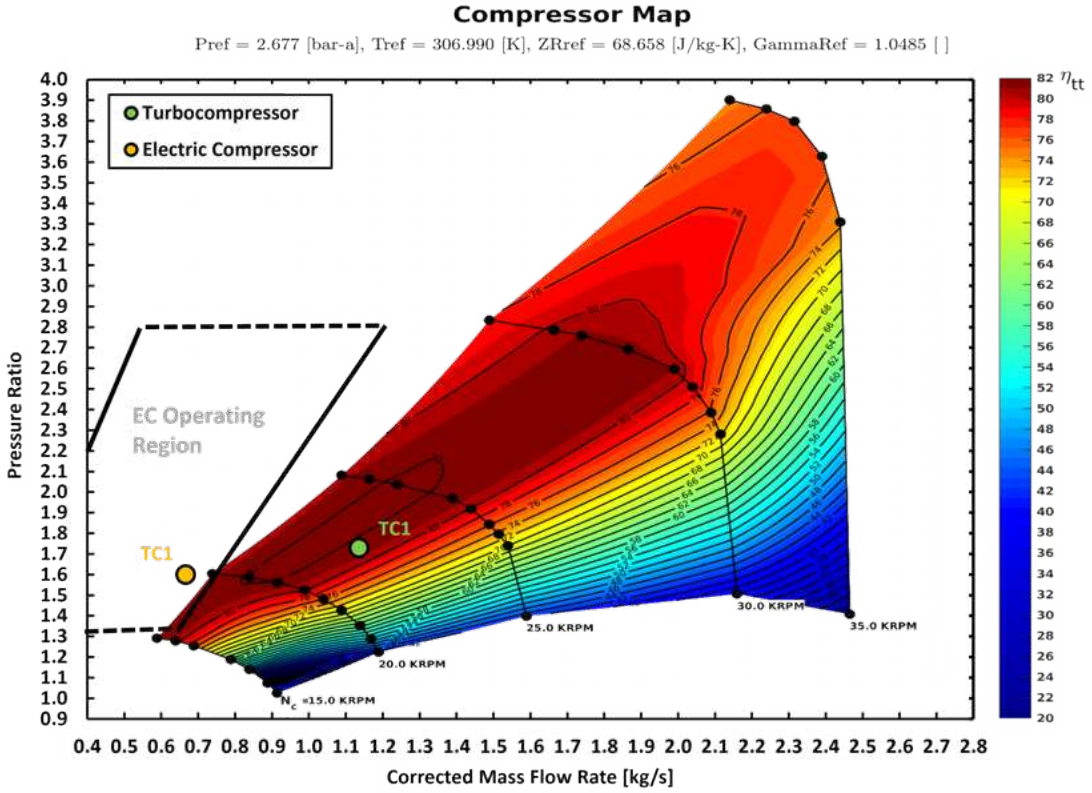

Figure 5-5: Compressor map results for the TC1 experiment. Both devices were operating within the operating region, and the system reached the target operating conditions.

With the test facility successfully reaching testing targets, a steady-state, ten-minute data point was collected to characterize the performance of the system while operating in the TC1 compressor configuration. Table 5-2 shows ten-minute averaged temperatures, pressures, and the associated enthalpies at each location in the power cycle and the cooling cycle throughout the TC1 test point. Figure 5-6 graphically represents these state points on a temperature-entropy diagram. The first stage, thermally driven compressor, pressurized the refrigerant vapor from 254.3 kPa to 440.3 kPa. The second stage electric compressor further pressurized the fluid from 440.3 to 703.5 kPa. These results show that the compression load was effectively shared between the thermally driven compressor and the electrically powered device. This can also be seen in the two-stage compression process shown on the right side of the T-s diagram in Figure 5-6.

Table 5-2: Average state points over the ten-minute steady state TC1 test point.

	Power Cycle			*Cooling Cycle*		
State Point	*Temperature [°C]*	*Pressure [kPa]*	*Enthalpy [kJ/kg]*	*Temperature [°C]*	*Pressure [kPa]*	*Enthalpy [kJ/kg]*
0	90.4	1360.5	453.9	34.4	262.0	414.4
1	89.9	1326.8	453.8	34.4	254.3	414.5
2	69.2	661.3	441.8	53.3	440.3	429.4
3	69.2	659.3	441.7	72.4	703.5	444.4
4	36.1	657.1	408.2	71.6	703.5	443.5
5	35.8	658.5	407.9	58.3	695.7	430.0
6	34.3	654.9	406.5	58.0	694.6	429.8
7	34.1	651.3	246.6	36.2	690.3	407.6
8	31.7	647.6	243.2	36.0	686.0	249.2
9	32.4	671.3	244.1	35.4	681.7	248.4
10	34.0	1460.0	246.5	34.7	678.1	247.5
11	34.0	1443.3	246.5	33.5	665.9	245.7
12	56.8	1440.4	279.8	33.1	669.6	245.2
13	56.8	1391.5	279.8	25.9	533.8	245.2
14	62.5	1388.4	288.7	6.0	268.4	245.2
15	62.4	1390.9	288.5	6.0	268.4	388.2
16	63.3	1380.8	289.9	6.5	268.4	388.7
17	63.0	1370.7	421.6	6.5	268.4	388.7
18	90.4	1360.5	453.9	34.4	262.0	414.4

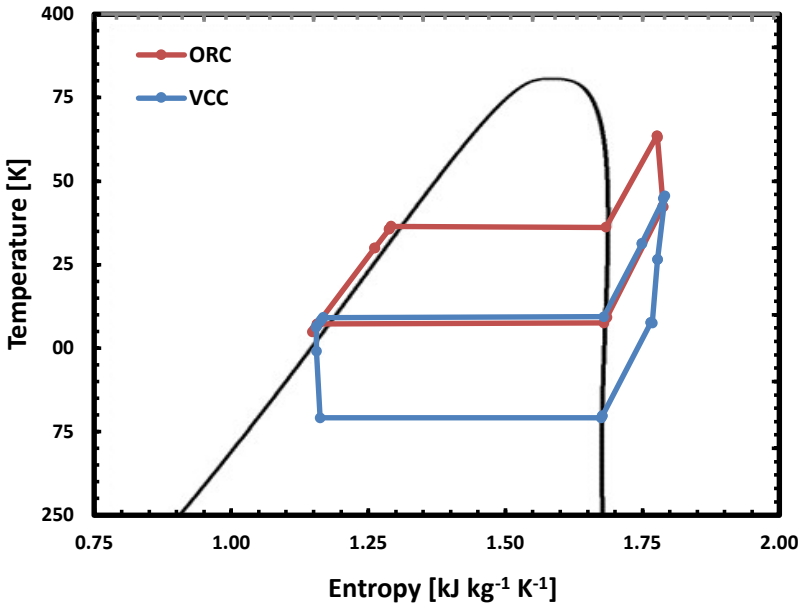

Figure 5-6: Temperature - entropy diagram for the TC1 steady state test.

Table 5-3 shows selected performance results from the steady-state TC1 test. The facility showed an improvement in performance over the system efficiency achieved in purely electric cooling mode and in purely thermal cooling mode when operating at the same conditions. The facility was operated in electric and thermal cooling modes with heat supplied at 91°C (thermal cooling only), heat rejected at 30°C, and cooling delivered at 9°C, to compare to the results of the TC1 hybrid cooling experiment. In electric cooling mode, the COP_e was 4.55. In hybrid cooling mode, the COP_e was 6.19. This was an expected improvement as electric input was no longer solely responsible for driving the system. In thermal cooling mode the COP_{th} was 0.42. In hybrid cooling mode the COP_{th} was 0.69. This was, again, an expected improvement, as the additional electric power in hybrid mode provided extra input for the system compared to thermal cooling mode.

COP_{vc} and η_{orc} represented the thermodynamic efficiencies of each individual cycle. The cooling cycle delivered 5.62 kW of cooling generated for every kW of compressor power used to drive the two compressors in the cycle. The ORC converted thermal energy into mechanical power at 6.98% efficiency. The three turbomachines operated efficiently during this test, contributing to the overall performance of the system. The isentropic efficiencies for the turbine, thermally driven compressor, and electrically driven compressor were 78.4%, 79.1%, and 68.6%, respectively. On average, throughout the ten-minute test, the experimental facility generated 176 kW of cooling from 257 kW of heat input and 28.4 kW of electric input.

Table 5-3: Performance results for the TC1 compressor configuration in hybrid cooling mode.

Performance Metric	*Value*
COP_{th} [-]	0.69 ± 0.035
COP_{e} [-]	6.19 ± 0.334
COP_{vc} [-]	5.62 ± 0.291
η_{orc} [%]	6.98 ± 0.129
η_{turb} [%]	78.4 ± 1.859
η_{tc} [%]	79.1 ± 1.888
η_{ec} [%]	68.6 ± 1.730
η_{shaft} [%]	74.3 ± 1.828
$\dot{W}_{\text{pump}}$ [kW]	2.74 ± 0.055
$\dot{W}_{\text{turb}}$ [kW]	20.7 ± 0.326
$\dot{W}_{\text{tc}}$ [kW]	15.9 ± 0.297
$\dot{W}_{\text{ec}}$ [kW]	16.3 ± 0.381
$\dot{Q}_{\text{boiler}}$ [kW]	256.6 ± 8.14
$\dot{Q}_{\text{condenser, orc}}$ [kW]	269.4 ± 7.74
$\dot{Q}_{\text{condenser, vc}}$ [kW]	193.6 ± 2.91
$\dot{Q}_{\text{evaporator}}$ [kW]	176.0 ± 8.94
$\dot{m}_{\text{orc}}$ [kg s^{-1}]	1.72 ± 0.002
$\dot{m}_{\text{vc}}$ [kg s^{-1}]	1.07 ± 0.016

5.4. Variable Heat Supply Performance Study

The results of the compressor configuration study showed that the TC1 compressor configuration offered the widest range of system operation. To quantify the limits and characterize the performance of the TC1 configuration, the facility was tested across the full range of heat inputs in tests 1-13 from Table 5-1. The facility operated in hybrid cooling mode with heat input

ranging from 113 kW to 313 kW (Tests 4-10). The facility also operated in thermal cooling mode, requiring 409 kW of heat input (Test #1), and in electric cooling mode with 0 kW of heat input (Test #13). Tests 2, 3, 11, and 12 failed to operate due to compressor limitations.

Figure 5-7 shows cooling duty and electric compressor power results across all the tests. A cooling duty of 175 kW was the target for all the experiments; however, this was not achieved at or below heat inputs of 218 kW (Tests 7-10). At 218 kW of heat input, electric compressor power was 23.4 kW, which was increased as heat input decreased, reaching 31.8 kW when the heat input was 136 kW to maintain the desired cooling duty target of 175 kW. However, increased electric compressor power was not enough to maintain the cooling duty target due to the rapidly dropping isentropic efficiency of the thermally driven compressor (from 80.6 % at 218 kW heat input to -4.0% at 136 kW heat input) at low heat input. This efficiency reduction prevented additional electric compressor power from boosting the cooling duty to meet the 175 kW target, limiting capacity to 125 kW when heat input was 136 kW. This efficiency limitation will be examined further in the analysis of turbomachinery results. At higher levels of heat input, electric compressor power successfully modulated the system capacity at the 175 kW cooling duty target. With 331 kW of heat input, the facility only required 16.9 kW of electric compressor power to deliver 178.7 kW of cooling power. When heat input dropped to 257 kW, the facility used 25.7 kW of electric compressor power to deliver a similar 176.1 kW of cooling duty. Figure 5-7 also shows that the system consumed 40.4 kW in the electric compressor to deliver 183.6 kW of cooling in electric cooling mode. The maximum total error for the cooling duty and compressor power data presented in Figure 5-7 was ± 9.15 kW and ± 0.64 kW, respectively. The inability of the facility to reach the 175 kW cooling capacity target for four of the test points was an unexpected result and highlights the importance of turbomachinery performance for the system.

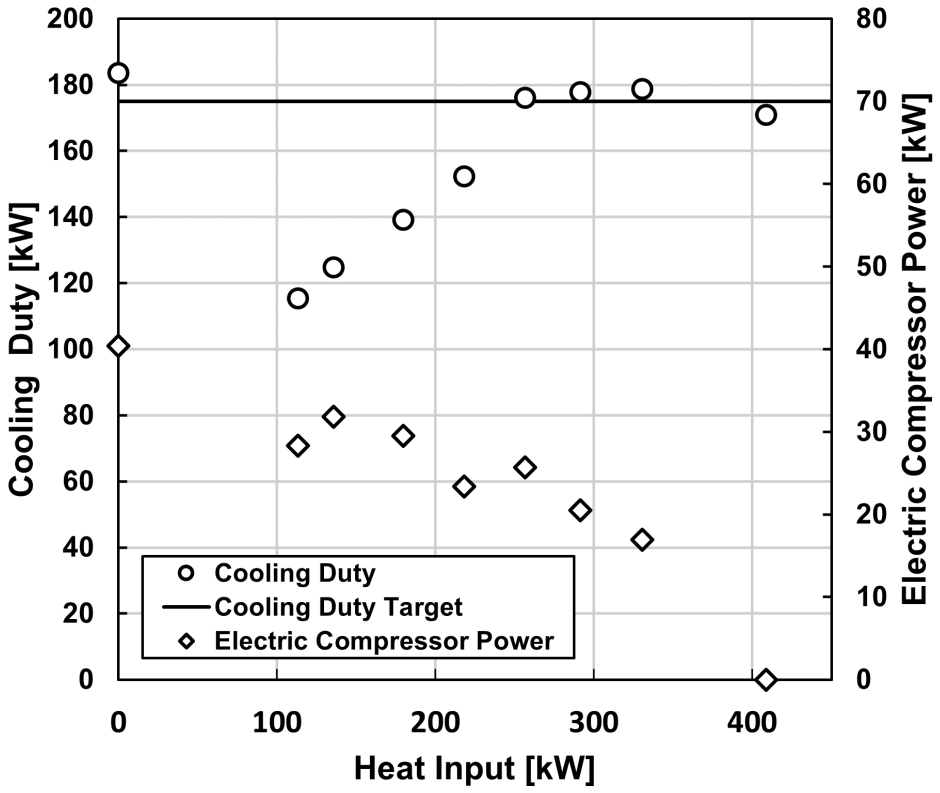

Figure 5-7: Cooling duty and electric compressor power results across the range of heat inputs tested.

Conversely from the electric compressor power presented in Figure 5-7, the power generated by the power cycle turbine increased with increasing heat input. With 113 kW of heat input, 5.2 kW of power was produced by the turbine. With 331 kW of heat input, the turbine power was 29.0 kW. With 113 kW of heat supply, the device operated at 15 kRPM with a pressure ratio of 1.36 and a power cycle mass flow rate of 0.89 kg s^{-1}, resulting in an isentropic efficiency of 81.4% for the test. At high heat input (331 kW), the turbine operated at 24 kRPM with a pressure ratio of 2.33 and a power cycle flow rate of 2.09 kg s^{-1}, yielding 77.4% isentropic efficiency for the test.

Another interesting result in the operation of the power cycle was the variation of boiler superheat and turbine pressure ratio across the different tests. At high heat input (331 kW), the

saturation temperature in the boiler was 70.3°C with 20.6°C of superheat at the outlet. This correlated to a turbine pressure ratio of 2.33. At low heat input (113 kW), the power cycle pump speed and cycle flow rate (0.89 kg s^{-1}) were reduced to reach the lower heat input target. This lowered the pressure in the boiler, reducing the saturation temperature to 45.7°C, and increased the superheat at the outlet to 45.1°C. With condenser pressure changing only 44 kPa across the range of tests, the reduced boiler pressure caused the turbine pressure ratio to drop to 1.36 as heat input was reduced to 113 kW. The lower pressure ratio contributed to the reduced performance of the cycle observed at low heat input, with the ORC efficiency dropping from 7.7% at high heat input (331 kW) to 2.8% at low heat input (113 kW).

The primary driver for many of the trends observed in this study was the performance of the two compressors. Figure 5-8 presents the compressor map results for the full range of experiments. Operating locations for the thermally driven compressor are plotted in reference to the colored map on the right using green points. Electric compressor operating points are plotted on the map outlined in black on the left side of the figure using yellow points. In general, the shift in pressure ratio between the two compressors is visualized on this plot. At high levels of heat input, the thermally driven compressor delivered most of the pressure rise, and vice versa at low levels of heat input. For example, when heat input was 331 kW, the pressure ratio across the thermally driven compressor was 2.38 and the electric compressor pressure ratio was 1.27. Conversely, when heat input was 113 kW, the turbocompressor pressure ratio was 0.97, and the electric compressor pressure ratio was 2.51. Figure 5-8 also shows operating points for thermal and electric cooling modes. While the thermal compressor was above the map in thermal cooling mode, surge was not observed and the system operated successfully.

Operating limits of the facility in hybrid cooling mode can also be explained by the operating points of the turbomachinery. At the high heat input operating limit (Test #4 – 331 kW), the electric compressor was at the minimum pressure ratio limit of the operating region. At this point, the pressure ratio across the device was 1.27, and operating at a lower pressure ratio was outside of the limits of the device. Despite operating at the lower limit of the map, the isentropic efficiency of the device was 56.1%. During this test, the pressure ratio across the turbocompressor was 2.38 and the isentropic efficiency for the device was 86.6%. This test indicated that the high input operating limit for the facility was a result of the pressure ratio minimum for the TT300 compressor. A device capable of lower lift operation could expand the operation of the system beyond this limit.

At the low heat input operating limit (Test #10 – 113 kW) the pressure ratio across the thermally driven compressor was 0.97. The suction pressure at the inlet of the electric compressor was therefore low, at 262.2 kPa, which triggered the low suction pressure warning on the device. Further reduction in heat input decreased this pressure, preventing the electric compressor device from operating at heat inputs lower than 113 kW. At this low heat input limit, the electric compressor operated in the upper portion of the map with a pressure ratio of 2.51 and an isentropic efficiency of 79.3%. These results indicate that the lower heat input operating limit is likely not a result of poor turbomachinery performance (i.e. operating at the edge of the compressor map) but was instead a result of the restrictive suction pressure safety limits caused by operating the TT300 with R1234ze(E) instead of R134a.

Figure 5-8 also shows the isentropic efficiency effect that prevented the facility from reaching the 175 kW cooling duty target across the full range of heat inputs. At higher heat input (257 kW and above), the turbocompressor operated in the highest efficiency region of the operating

map. This resulted in very little change in isentropic efficiency as the pressure ratio across the device changed. At 331 kW of heat input, when the pressure ratio across the turbocompressor was 2.38, the isentropic efficiency for the device was 86.6%. When the pressure ratio decreased to 1.73 with 257 kW of heat input, the isentropic efficiency for the device was 79.1%. This drop in pressure ratio by 0.65 resulted in an efficiency drop of just 7.5%. This enabled changes in pressure ratio caused by increased electric boost to have minimal effect on the performance of the turbocompressor. However, at lower levels of heat input (218 kW and below), the device operated in a region of the map where the isentropic efficiency was more sensitive to pressure ratio. For example, a small 0.2 drop in pressure ratio from the operating point of the 218 kW test point resulted in an efficiency drop to about 68%, a reduction of 11%. This represents a significantly larger efficiency impact over a pressure ratio change one third the size when compared to the high pressure ratio region of the operating map. The increased sensitivity of the turbocompressor to pressure ratio led to an unexpected result for the tests with heat input below 218 kW. An increase in electric compressor power resulted in reduced overall cooling capacity. At the operating locations associated with heat input below 218 kW on the turbocompressor map, a small drop in pressure ratio correlated with a large drop in the isentropic efficiency of the device. Increasing electric compressor power increased the electric compressor pressure ratio and decreased the turbocompressor pressure ratio. The large drop in the efficiency of the turbocompressor associated with the drop in pressure ratio had more impact on the cooling capacity than the increased electric compressor power. This isentropic efficiency impact becoming dominant at low levels of heat input led to the very low turbocompressor efficiencies observed (-4.0% at 113 kW) and prevented the facility from reaching the 175 kW capacity target with heat input of 218 kW or less.

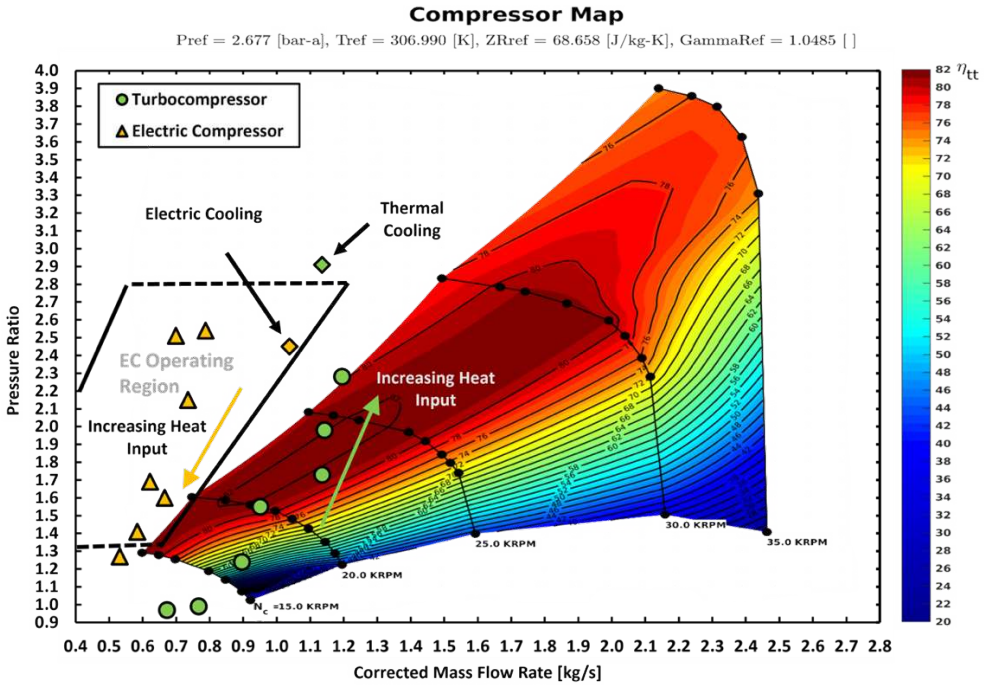

Figure 5-8: Compressor map results for the experimental facility across the range of heat inputs. The two points marked with diamonds represent purely thermal or purely electric operation.

Despite the complex efficiency effects, overall system performance results show an expected trend, presented in Figure 5-9. In fully electric cooling mode with 0 kW of heat input, the electric COP was 4.55. Thermal COP does not apply since there was no thermal energy input. In hybrid cooling mode with 113 kW of heat input, the electric COP was 3.80, and the thermal COP was 1.02. As heat input increased from 113 kW to 331 kW, the electric COP increased to 8.76 and thermal COP decreased to 0.54. In fully thermal cooling mode, thermal COP was 0.42 and electric COP was 22.6. Electric COP is reported in fully thermal mode due to the electricity consumed by the power cycle pump while operating the organic Rankine power cycle. Measurement error was propagated through the performance calculations to quantify the uncertainty of these results. The maximum total error for thermal COP was 0.081 and the maximum error for electric COP was 0.46 (when electric COP was 8.8). In general, full system COP was improved by running in hybrid mode when compared to full thermal or full electric mode

if waste heat input was greater than 136 kW. For example, with 257 kW of heat input, the thermal COP increased to 0.69 from the 0.42 thermal COP achieved in purely thermal cooling mode. Similarly, the electric COP with 257 kW of heat input was increased to 6.2 from the 4.6 electric COP achieved in the electric cooling test.

However, the electric COP was lower in hybrid mode compared to electric only mode at low levels of waste heat input. During these tests (Test 9 and 10 – 113 and 136 kW) the thermally driven compressor power was so low that the pressure ratio across the device dropped below 1 (0.97 and 0.99). In these cases, the refrigerant was being forced through the thermal compressor and required higher compressor lift than what was needed in purely electric operation. These tests were also limited by the back work associated with operating the power cycle pump. In both tests, the pump consumed over 1.8 kW of power that further impacted the electric COP. This reduced system performance and caused the electric COP to drop below the electric only baseline of 4.55 for these two tests.

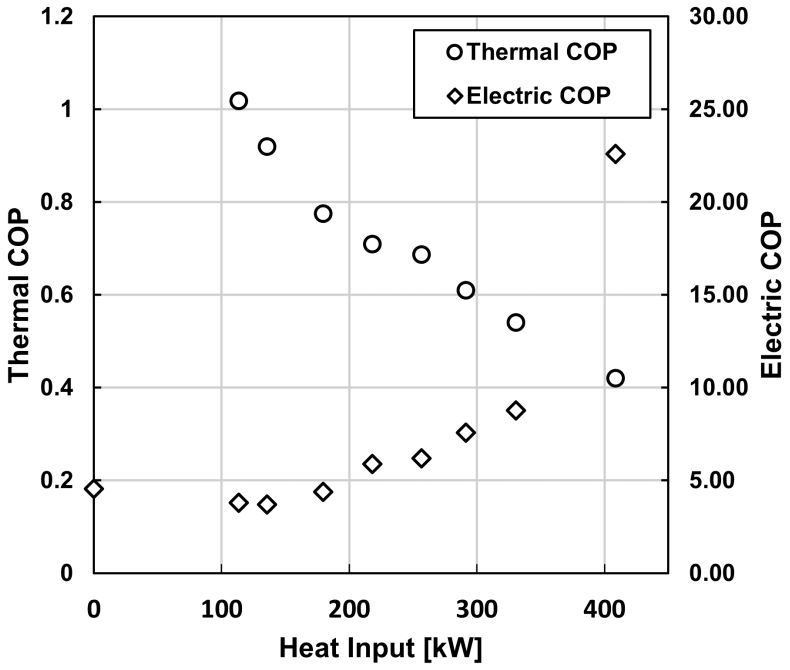

Figure 5-9: Hybrid mode system performance results across the tested range of heat inputs.

5.5. System Improvements

The experimental results presented in this work show the potential of the hybrid ORVC system for HVAC applications but also highlight some important limitations in the experimental facility. In the compressor configuration comparison study, only one of the three configurations successfully reached the testing targets (TC1). The other two configurations, PC and EC1, failed to reach the operating targets due to turbomachinery limitations. In the variable heat input study, four of the 13 test points failed to operate, again due to turbomachinery limitations. The turbomachines utilized in this work were designed for differing applications. The turbocompressor was designed to operate with R1234ze(E) and the electric compressor was designed around R134a. The two fluids have differing densities (14.4 kg m^{-3} for R134a and 5.93 kg m^{-3} for R1234ze(E) at 0^{o}C) which drives different mass flow rate designs for each compressor. The electric compressor operating region ranges from 0.17 kg s^{-1} to 1.24 kg s^{-1} on the equivalent mass flow rate axis while the turbocompressor operating region ranges from 0.59 kg s^{-1} to 2.47 kg s^{-1} on the same axis. This mass flow rate mismatch between the two devices required operation of the experimental facility at reduced capacity from its design point. The facility was originally designed to operate at 264 kW scale, but it was operated at 175 kW scale to alleviate the choke limitation that would be experienced in the electric compressor at the larger scale [54]. The reduction in cooling duty enabled a reduction in refrigerant mass flow rate (from 1.6 kg s^{-1} to 1.0 kg s^{-1}) to avoid choke in the electric compressor. This also impacted the maximum possible performance as the turbocompressor would not be able to operate at the highest efficiency point due to the reduced capacity.

The TT300 electric compressor used in this work also caused a smaller operating range of heat inputs for the test facility. At the high heat input operating limit (331 kW), the pressure ratio

across the electric compressor was at the lower pressure ratio limit of the operating region, forcing the device to shut down due to low load. The low heat input limit was a result of the differing design working fluids. Since the electric compressor was designed for R134a, which is a higher-pressure fluid than R1234ze(E), it was intended to operate at higher pressures. This put a limit on the low heat input tests as the lower limit for the suction pressure of the device was reached with low thermal input. This low-pressure limitation also prevented testing at the industry standard chilled water delivery temperature of 7°C due to inability to operate in electric only mode at that condition. The facility was instead operated with a 9°C chilled water delivery target for all the tests to maintain consistent operating conditions.

The mismatch between the two turbomachines also led to the failure of the PC and EC1 compressor configurations. In the PC configuration, the low suction pressure limitations associated with the R134a design fluid for the electric compressor prevented the system from reaching the targeted operating conditions using R1234ze(E). In the EC1 test, the turbocompressor was operating in the surge region left of the operating map and the electric compressor was operating at the choke limit on the right side of the map due to the mass flow rate mismatch between the two devices. The failure to reach the targeted operating conditions can also be attributed to the mismatch between the compressors in the EC1 configuration.

Improved compressor selection and matching would alleviate many of these challenges. While the TT300 provided for this work enabled valuable investigation of the hybrid ORVC concept, it was not carefully selected for this application. An electric compressor designed to operate with R1234ze(E) would allow the device to operate at lower pressures. This would eliminate the challenges stemming from the low suction pressure limitation that was experienced with the electric compressor in this work. Selecting an electric device with higher mass flow

capabilities would also better match the thermally driven compressor used in this work. This would enable operation of the facility at its higher, design capacity of 264 kW and boost efficiency by allowing both compressors to operate at the highest efficiency point. Improved compressor selection may also enable operation in the PC and EC1 compressor configurations as the surge and choke regions of the two operating maps would be more closely aligned.

5.6. Chapter Summary

In this chapter, experimental validation of the hybrid ORVC system was presented. Experimental parameters were discussed to evaluate the technology across the three compressor configurations: PC, EC1, and TC1. Experimental methodology was also described to quantify the performance of the system across a range of heat input quantities and characterize the performance of the system from fully thermal to fully electric operation. Test facility operating procedures were also discussed to describe the nuances of testing the facility in the three operating modes: electric cooling mode, thermal cooling mode, and hybrid cooling mode. Data processing methodology was also discussed to synthesize raw temperature, pressure, flow rate, and power data from the test facility into meaningful performance metrics.

In the compressor configuration comparison study, only one of the three tested configurations successfully met performance targets. The parallel configuration failed due to the electric compressor's suction pressure limitations, while the series configuration with the electric compressor first was limited by choke conditions. The most effective setup placed the turbocompressor first, enabling the system to achieve 176 kW of cooling from 257 kW of thermal input and 20.1 kW of electric input.

The variable heat supply study evaluated the performance of the system. The test facility operated successfully with heat input ranging from 113 kW to 331 kW. Below 113 kW, suction

pressure constraints hindered the electric compressor's operation, while at high heat input, low pressure ratio conditions restricted the device's operation. System efficiency varied, with thermal COP decreasing from 1.02 to 0.54 as heat input increased, while electric COP improved from 3.80 to 8.76. Hybrid operation outperformed purely thermal or electric modes, except at very low heat input levels where performance degradation occurred due to low pressure ratios across the turbocompressor. In the following chapter, experimental evaluation of the test facility will be expanded to off-design conditions to fully characterize the performance of the system for real world applications.

CHAPTER 6. Experimental Performance Assessment at Off-Design Conditions

Experimental evaluation of the hybrid ORVC test facility was extended to off-design operating conditions to develop a more complete characterization of the technology performance. Five off-design studies were performed to understand how various parameters impacted system performance. An investigation of electric compressor power level was conducted to quantify the effect of this key aspect of the hybrid ORVC system. Additionally, three studies were performed to characterize the impact of variable operating temperatures—heat input, heat rejection, and cooling delivery—on the operation of the system. Finally, experiments were conducted to quantify the integrated part-load value (IPLV) for the system. When taken together, these results provide critical understanding of the performance of the technology under realistic operating conditions.

6.1. Importance of Off-Design Performance

In many real-world applications, cooling equipment must operate in a range of conditions. This may include variable ambient temperatures that impact condenser operating temperatures, variable cooling delivery temperatures that impact the operating temperatures in the evaporator, or, in the case of thermally driven cooling technologies, variable temperatures of the driving heat source. These conditions are so variable in a realistic application that most cooling equipment operates away from its design point more often than not [71]. As a result, accurately understanding the performance of any cooling technology at off-design conditions is critically important [72].

The variable nature of cooling technology applications has led to the development of specialized performance metrics to capture and compare cooling equipment performance in realistic applications. The Integrated Part-Load Value (IPLV) has been standardized by AHRI to

quantify the performance of equipment across a range of operating conditions [56]. IPLV methodology and results will be discussed in detail later in this chapter.

6.2. Experimental Procedure

Five unique experimental studies were completed to characterize the off-design performance of the hybrid ORVC system. One study examined the effect of variable levels of electric compressor power on the system. Three parameter studies explored the impact of thermal reservoir temperatures on the system performance. These reservoir temperatures were represented by the boiler heat supply temperature, the condenser water supply temperature, and the temperature of the chilled water delivered by the system. The final study was a series of experiments based on the standard tests used to quantify the IPLV.

6.2.1. Electric Compressor Power Study

The first study evaluated the impact of electric input on the operation of the system. The facility was operated at design point conditions with 250 kW of heat input. Design point operating conditions for the facility are heat input at 91^{o}C, condenser water inlet at 30^{o}C, and chilled water delivered at 7^{o}C based on AHRI performance rating standards [56,57]. Three experiments were performed, each with a different level of electric compressor power: 19.2 kW, 23.2 kW, and 33.9 kW. For this study, the cooling duty of the facility was not fixed as it depended on the level of electric compressor input. The system was operated at steady state for each test and the impact of each level of electric input was examined.

6.2.2. Parametric Studies

The three parametric studies all utilized a similar experimental design. A series of experiments were performed with the parameter of interest varying across a temperature range based on AHRI performance rating standards [56,57]. All other operating conditions were held at

their design point values. The cooling duty target for all tests was 175 kW and the boiler heat duty was set to 250 kW or 300 kW for each series of experiments. The level of heat input was chosen to maintain an operating point where the compressor load was not skewed towards one device or the other. For the boiler temperature parameter study, the temperature of the heat supply fluid entering the boiler was manipulated using a combination of a variable capacity steam boiler and electric circulation heaters. For the variable condenser temperature study, the condenser water inlet temperature was manipulated using a variable capacity wet cooling tower. The cooling tower fan speed was controlled to set the condenser inlet temperature to the AHRI testing range. For the variable chilled water delivery temperature study, chilled water outlet temperature was controlled using a variable capacity cooling load. Temperature ranges for each study along with other important experimental design parameters are presented in Table 6-1.

Table 6-1: Temperature ranges and operating conditions for the three parametric studies.

Study	*Boiler Inlet Temperature [°C]*	*Heat Supply [kW]*	*Chiller Delivery Temperature [°C]*	*Chilling Duty [kW]*	*Condenser Inlet Temperature [°C]*
1	85 - 110	300	6.7	175	30.0
2	91.0	300	2.1 – 21.1	175	30.0
3	91.0	250	6.7	175	21 - 31

6.2.3. IPLV Study

The integrated part load value or IPLV is a performance metric for cooling equipment designed to give a more realistic indication of the performance of a cooling system when operating in real-world applications [56]. Since cooling systems rarely operate at their full capacity design point, IPLV testing also takes the performance of a system at reduced capacity and lower condenser

temperatures into account. In total, four experiments are required to quantify the IPLV, one test at 100%, 75%, 50%, and 25% of the designed cooling capacity. The boiler heat duty target was set to scale with the cooling duty target at a level that would maintain balance between the electric and thermally driven compressors. Table 6-2 presents the testing conditions for the series of IPLV experiments.

Table 6-2: Testing conditions for the IPLV study.

Test (% Capacity)	*Boiler Inlet Temperature [°C]*	*Chiller Delivery Temperature [°C]*	*Chilling Duty [kW]*	*Boiler Heat Duty [kW]*	*Condenser Inlet Temperature [°C]*
A (100%)	91	6.7	175.0	300.0	30.0
B (75%)	91	6.7	131.3	233.3	24.5
C (50%)	91	6.7	87.5	166.7	19.0
D (25%)	91	6.7	43.8	100.0	19.0

The results from the four IPLV tests are used in Equation 1 to calculate the integrated part load value,

$$IPLV = 0.01 * A + 0.42 * B + 0.45 * C + 0.12 * D \quad (1)$$

where A, B, C, and D represent the system COP for each of the corresponding tests [56].

6.2.4. Experimental Procedures

Procedures for completing the full series of off-design studies shared many of the methods that were utilized and described with the design point testing presented in Chapter 5. The startup and operating procedure for the test facility was consistent across all the experiments performed

for this research. To begin each experiment, flow was initiated in the auxiliary heat transfer loops for the boiler and the condensers. The power cycle pump was then started to drive flow through the ORC. Upon startup, refrigerant flow was bypassed around the turbine to allow the cycle to get up to operating temperatures before sending fluid through the turbine. Once there was sufficient superheat at the outlet of the boiler (approximately 5^{o}C), flow was started in the external heat transfer stream for the evaporator, and flow was passed through the turbine. As flow was initiated through the turbine, the electric compressor was started. This allowed both the turbocompressor and the electric compressor to ramp up simultaneously. The speed of the electric compressor was modulated to maintain balance with the turbocompressor within the limits of the parameters of the experiment. The cooling capacity of the facility was modulated by controlling the power sent to the electric compressor. If the cooling duty delivered was below the target, the electric compressor power was increased, and vice versa if the cooling duty was above the target capacity. The heat input duty was regulated by adjusting the power cycle pump speed. An increase in pump speed resulted in a higher refrigerant mass flow rate within the ORC, increasing heat transfer in the boiler. The power cycle pump speed was modulated to achieve the target heat input duty during each test.

Once steady operating conditions were reached, boiler inlet temperature, condenser inlet temperature, and evaporator outlet temperature were modulated to reach the parameters of each test. Boiler inlet temperature was modulated using two control parameters. Six electric immersion heaters were located in the auxiliary heat supply circuit. These heaters were incrementally and periodically turned on and off to maintain the boiler inlet setpoint. As an additional control parameter, a steam flow control valve was used to modulate the flow of steam to the steam heat exchanger on the heat supply loop. Modulating the steam flow rate controlled the heat duty from

the steam boiler into the heat supply circuit. This provided a secondary control over the heat supply temperature at the inlet of the boiler. Condenser inlet temperature was controlled using the variable speed fans on the evaporative cooling tower that rejected heat from the auxiliary condenser loop. Increased fan speed increased heat rejection to the atmosphere, reducing the temperature of the heat transfer fluid in the condenser loop. Cooling tower fan speeds were modulated to achieve the desired condenser inlet temperature using a PID controller. The evaporator outlet temperature was controlled via a flow control valve on the heat supply for the simulated cooling load. Increasing this flow rate provided more heat to the evaporator auxiliary heat transfer loop, effectively increasing the temperature at the outlet of the device. This flow control valve was also controlled using a PID controller tuned to maintain the evaporator outlet temperature at the experimental setpoint. Once the experimental parameters were reached throughout the test facility, a five-minute steady-state test was conducted. Temperature, pressure, flow rate, and other relevant data were averaged over the test duration to obtain the results for each experiment. Data processing methods, including turbomachinery analysis, remained consistent with the procedures presented in Sections 4.3.2 and 5.2.

6.3. Electric Compressor Power Study

One of the key novelties of the hybrid ORVC system is the addition of electric input in the form of an electric compressor integrated into the vapor compression cooling cycle. The first study examines the effect of different levels of electric input. The facility was operated at design point operating conditions with three levels of electric compressor power: 19.2 kW, 23.2 kW, and 33.9 kW. Table 6-3 and Figure 6-1 present facility performance and compressor map results for the three experiments.

Table 6-3: Facility performance results for the electric compressor power study.

Electric Compressor Power [kW]	*Cooling Duty [kW]*	*Electric Compressor Isentropic Efficiency [%]*	*Turbo-compressor Isentropic Efficiency [%]*	*Thermal COP [-]*	*Electric COP [-]*
19.2	155.6	69.2	87.5	0.603	7.04
23.2	162.1	71.4	83.0	0.620	6.20
33.9	170.4	74.7	57.1	0.682	4.63

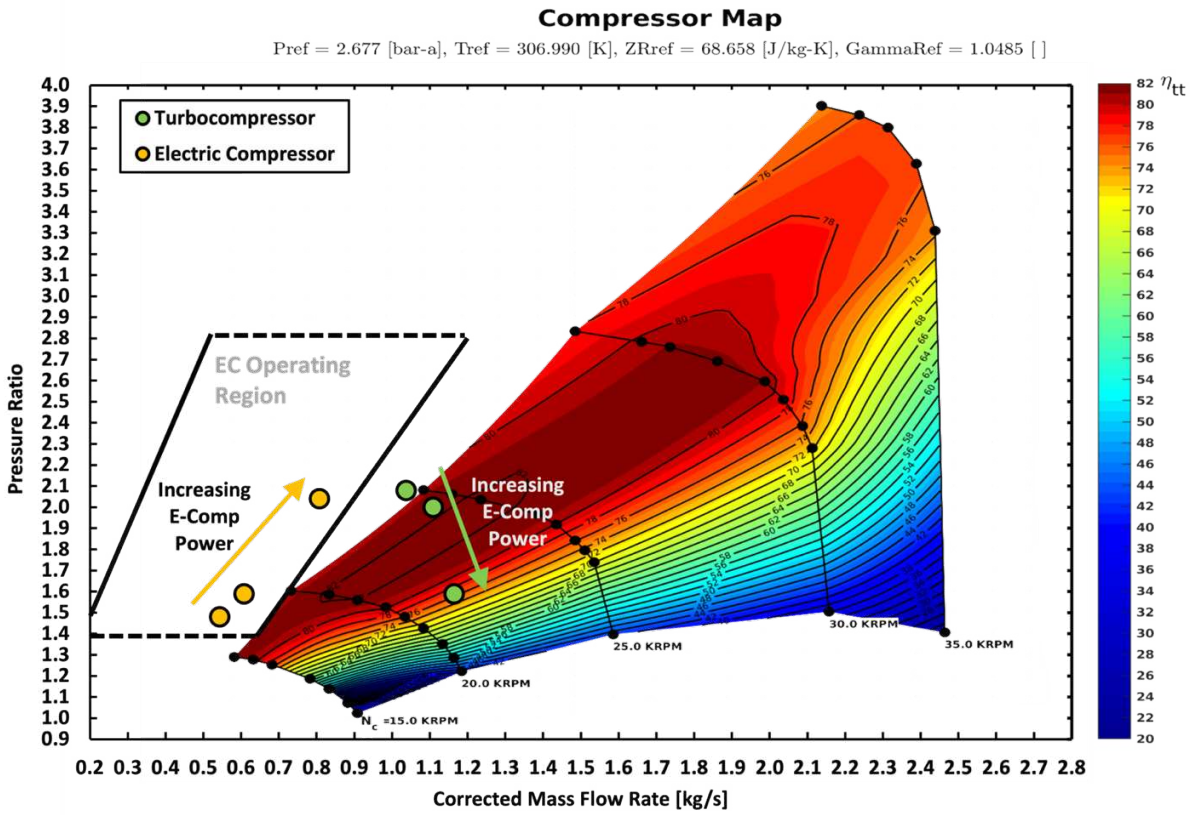

Figure 6-1: Compressor map results for the electric compressor power study.

It was observed that increased electric compressor power resulted in increased cooling duty. When electric compressor power was 19.2 kW, the facility produced 155.6 kW of cooling power. When the electric compressor power was increased to 33.9 kW, cooling duty increased to 170.4 kW. These results demonstrate that the cooling duty of an ORVC system can be boosted

through additional electric input into the vapor compression cycle. This is the key functionality of the hybrid ORVC concept, allowing the system to adapt to variable conditions through supplemental electric input.

However, it is also clear from these results that boosting the cooling capacity of the system with electric input had limited effectiveness due to the complex interactions between the thermally driven compressor and the electrically powered device. The capacity increment between each test indicates this. Between the 19.2 kW and 23.2 kW experiments, the electric compressor power increased by 4.0 kW. Cooling duty during the 19.2 kW test was 155.6 kW, but the 23.2 kW test had a cooling duty of 162.1 kW, an increase of 6.5 kW from the 19.2 kW experiment. This represents an increase of 1.63 kW of cooling power per kW of additional electric compressor power. Contrasting this with the increment between the medium and high compressor power tests, there was an increase in cooling duty of 8.3 kW with a power increase of 10.7 kW. This was an increase of 0.78 kW of cooling capacity per kW of additional electric compressor power, a significantly lower result than the incremental capacity increase between the low and medium power tests.

These results show that using additional electric compressor power to boost cooling capacity was more effective between the low and medium-power tests than between the medium and high-power tests. The mechanism that drives this phenomenon can be explained using the compressor map results presented in Figure 6-1. As the electric compressor power increased, the pressure ratio across the device increased, moving the operating point up on the map. The increased electric compressor pressure ratio reduced the pressure ratio across the thermally driven compressor as the compression load was shifted from one device to the other. This moved the operating point of the thermally driven compressor down on the map. The operating point also

moved to the right for both compressors as electric compressor power was increased. This was driven by a slight increase in flow rate (0.917 kg s^{-1} to 1.002 kg s^{-1}) as well as reduced pressure at the suction of the electric compressor that drove the electric compressor's equivalent mass flow rate up due to density effects.

The movements on the compressor maps explain the limited effect of additional electric compressor power on the capacity of the system. When the electric compressor power was 19.2 kW, the thermally driven compressor operated with a pressure ratio of 1.94 and a corrected mass flow rate of 1.04 kg s^{-1}. This placed the device near the highest efficiency operating point on the map, and the machine operated with an isentropic efficiency of 87.5% during the test. During the medium power test (23.2 kW), the thermally driven compressor operated in a similar region of the map (PR=1.85, $\dot{m}_{\mathrm{eq}}$=1.11 kg s^{-1}) and delivered an isentropic efficiency of 83.0%. As is visible in Figure 6-1, the lines of constant efficiency are relatively far apart surrounding the central, high efficiency of the map. As a result, the change in operating location had a minimal impact on the isentropic efficiency of the device. This allowed the additional electric compressor power to boost the capacity of the system.

However, during the high power experiment, when the electric compressor power was 33.9 kW, the thermally driven compressor operated with a pressure ratio of 1.47 and a corrected mass flow rate of 1.16 kg s^{-1}. This operating point was below the highest efficiency region of the map, and the device operated with a significantly lower isentropic efficiency of 57.1%. In this region of the map, the efficiency lines are much closer together, indicating that a small change in operating location results in a much more significant drop in efficiency (down to 57.1%). The reduction in turbocompressor efficiency prevented any significant increase in cooling capacity during the high-power experiment.

These results illustrate a concept that the use of electric compressor power was an effective strategy to improve the performance and operating range of the ORVC system, but the operating locations on the compressor maps were often the most important factor in determining the performance of the system under off-design conditions. This concept will be discussed further in the following sections.

6.4. Parametric Studies

6.4.1. Variable Boiler Temperature Study

The first of the three parametric studies examined the effect of boiler temperature on the operation of the hybrid ORVC system. The test facility was able to operate with the boiler heat supply fluid inlet temperature ranging from 85°C to 110°C. Six experiments were performed across this range. The condenser water inlet temperature was maintained at 30°C and chilled water was delivered at 7°C for all six experiments. The heat input duty target was 300 kW and the cooling duty target was 175 kW for the study. The power cycle pump speed and electric compressor speed were modulated to maintain these targets. Figure 6-2 presents key results from the six experiments. The turbine work was calculated as the thermodynamic work extracted from the power cycle working fluid. The electric compressor power was the electrical power consumed in the device. The cooling duty and associated target are also presented in Figure 6-2.

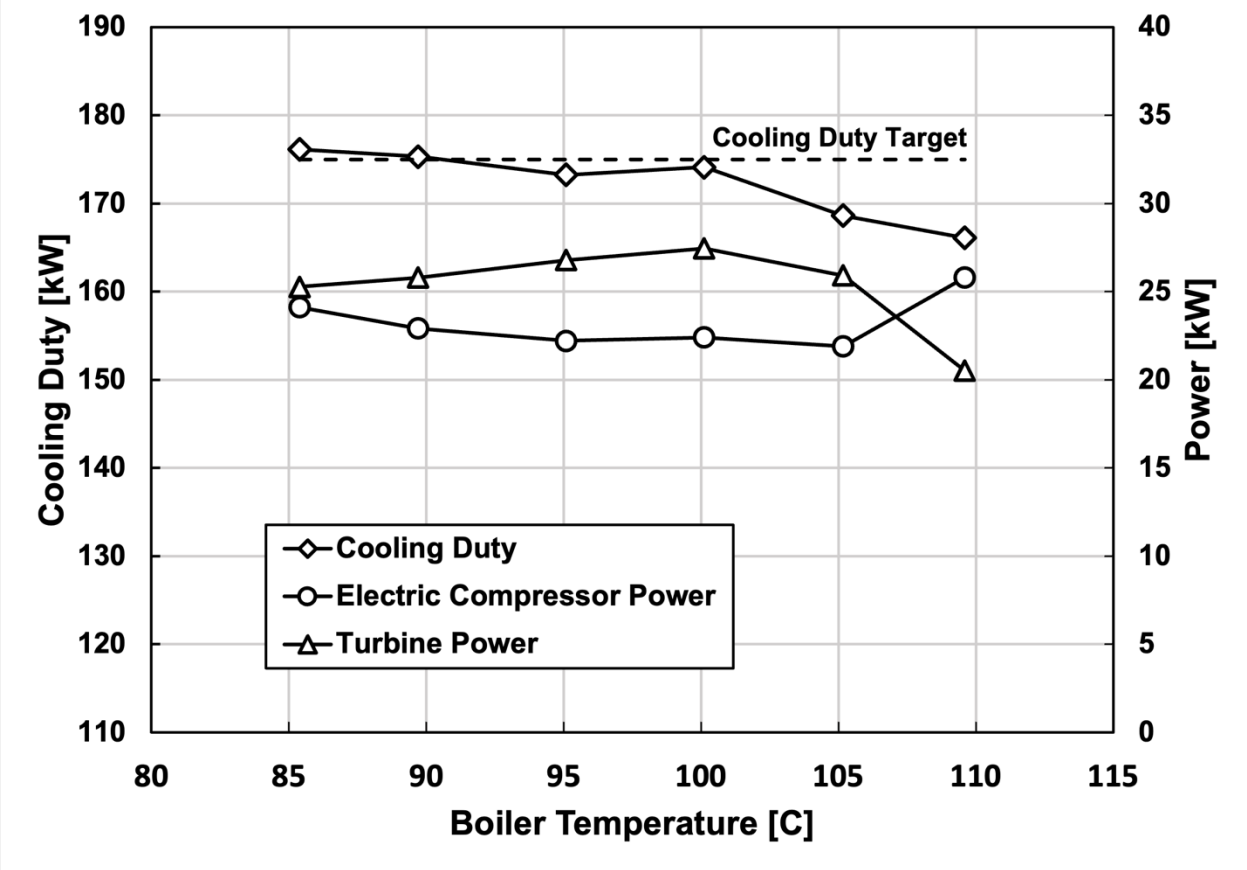

Figure 6-2: Cooling duty, electric compressor power, and turbine power results for the variable boiler temperature study.

Two distinctive trends were observed during this study. At boiler temperatures below 100°C, the impact on system performance caused by increasing boiler temperature was relatively simple. As boiler temperature increased, the pressure ratio across the turbine increased slightly, from 2.22 at 85°C to 2.24 at 100°C. This caused an increase in power generated by the turbine, increasing from 25.3 kW at 85°C to 27.5 kW at 100°C. The electric compressor power was reduced slightly from 24.1 kW at 85°C to 22.4 kW at 100°C. This successfully modulated the cooling duty of the system, which remained at the 175 kW target for the four experiments from 85°C to 100°C.

At boiler inlet temperatures above 100°C, the heat exchange performance in the boiler improved enough to increase the overall heat duty of the device above the 300 kW heat input target that was set for this study. In response to this, the power cycle refrigerant mass flow rate was

reduced by reducing the power cycle pump speed in order to maintain the heat input duty at the 300 kW target. The reduced flow rate and boiler pressure associated with the lower pump speed led to a decrease in turbine power, with the power developed by the power cycle dropping from 27.5 kW at 100°C to 20.5 kW at 110°C. Electric compressor power was increased from 22.4 kW at 100°C to 25.8 kW at 110°C in an effort to make up for the drop in turbine power. However, despite the increased electric power, the cooling duty target was not met at boiler temperatures above 100°C, with the facility only producing 166.1 kW of cooling power during the 110°C experiment. If heat input was not constrained to 300kW it is likely that this phenomenon would not have been observed. Instead, heat input would have increased above 300 kW, and the cooling duty target would likely have been met with reduced electric input as boiler temperature climbed above 100°C.

The limited effectiveness of supplemental electric compressor power at boiler temperatures can be explained by reduced compressor efficiency similar to the concept discussed in the previous section. Turbomachinery results provide the clearest insight into the interactions between the devices that caused this effect. Figure 6-3 presents the compressor map results for the six experiments in the study.

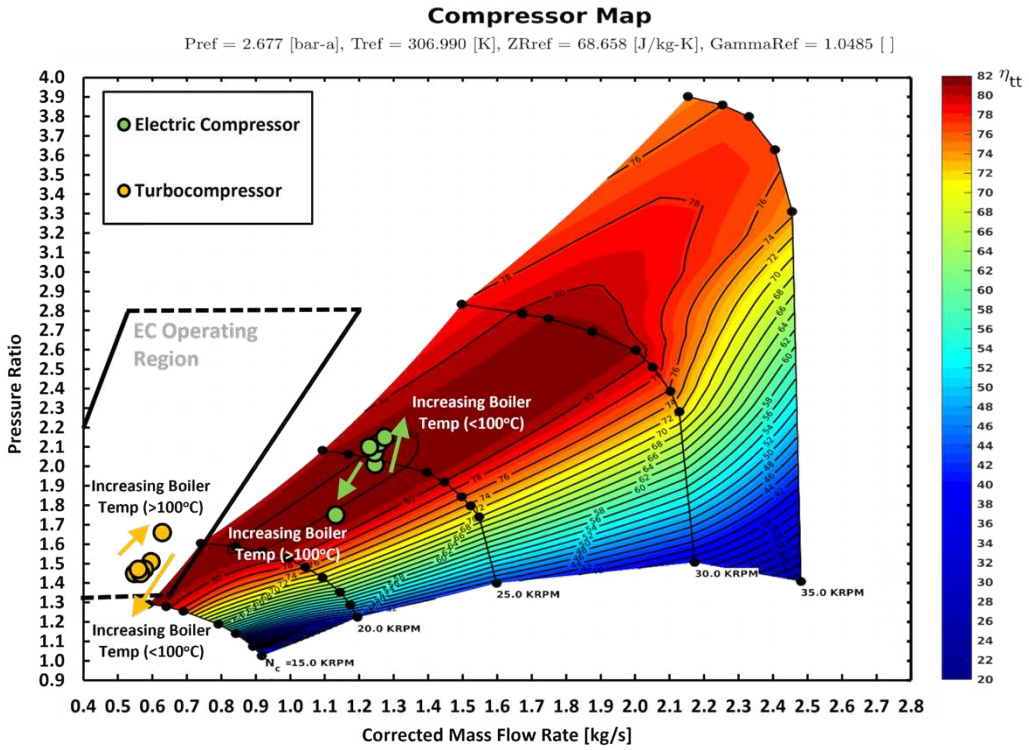

Figure 6-3: Compressor map results for the variable boiler temperature study. Trends are shown for above and below 100°C.

At boiler temperatures below 100°C, the thermally driven compressor moves up on the map and the electric compressor moves down on the map with increasing boiler temperature. The additional turbine power produced at higher boiler temperatures leads to more of the compression load being delivered by the thermally driven compressor. This results in an increased pressure ratio for the thermally driven device and a reduced pressure ratio for the electric compressor. This is reflected in the results as the pressure ratio across the thermally driven compressor increased from 2.01 at 85°C to 2.15 at 100°C and the pressure ratio across the electric compressor decreased from 1.51 at 85°C to 1.45 at 100°C.

At boiler temperatures above 100°C, the trend reversed, with the thermally driven compressor moving down on the map and the electric compressor moving up. The reduced power cycle pump speed and ORC flow rate led to a reduction in turbine power above 100°C. The reduced

power available to the turbocompressor led to a greater share of the compression load being delivered by the electric compressor. At 110°C, the electric compressor pressure ratio increased to 1.66 from 1.45 at 100°C. The thermally driven compressor pressure ratio dropped from 2.15 at 100°C to 1.75 at 110°C. At these operating conditions, the thermally driven compressor moved into a region of the operating map that resulted in lower isentropic efficiency. At 100°C, the device operated with an isentropic efficiency of 84.5%. With the reduced pressure ratio at 110°C, the isentropic efficiency decreased to 78.9%. The reduced efficiency of the turbocompressor, along with the reduced power cycle mass flow rate, prevented the system from reaching the 175 kW cooling duty target at boiler temperatures above 100°C. Any further increase in electric compressor power during these tests further decreased the isentropic efficiency of the thermal device, preventing any increase in system capacity.

Despite the limitations above 100°C, the thermal and electric COP of the system remained high across the series of experiments, as shown in Figure 6-4. At boiler temperatures below 105°C, the thermal COP generally decreased as boiler temperature increased, dropping from 0.59 at 85°C to 0.54 at 105°C. This trend was driven by the decrease in electric compressor power across this temperature and range and represents a subtle shift in compressor load from the electric compressor to the thermal device. This effect was similarly represented in the electric COP results with the metric slightly increasing from 6.50 at 85°C to 6.86 at 105°C. Above 105°C, both trends reversed due to the drop in turbine power and thermal compressor isentropic efficiency. The compression load was shifted back to the electric compressor to account for these changes and prevent a large drop in cooling capacity. This resulted in the thermal COP increasing from 0.54 at 105°C to 0.56 at 110°C and the electric COP decreasing from 6.86 at 105°C to 5.86 at 110°C.

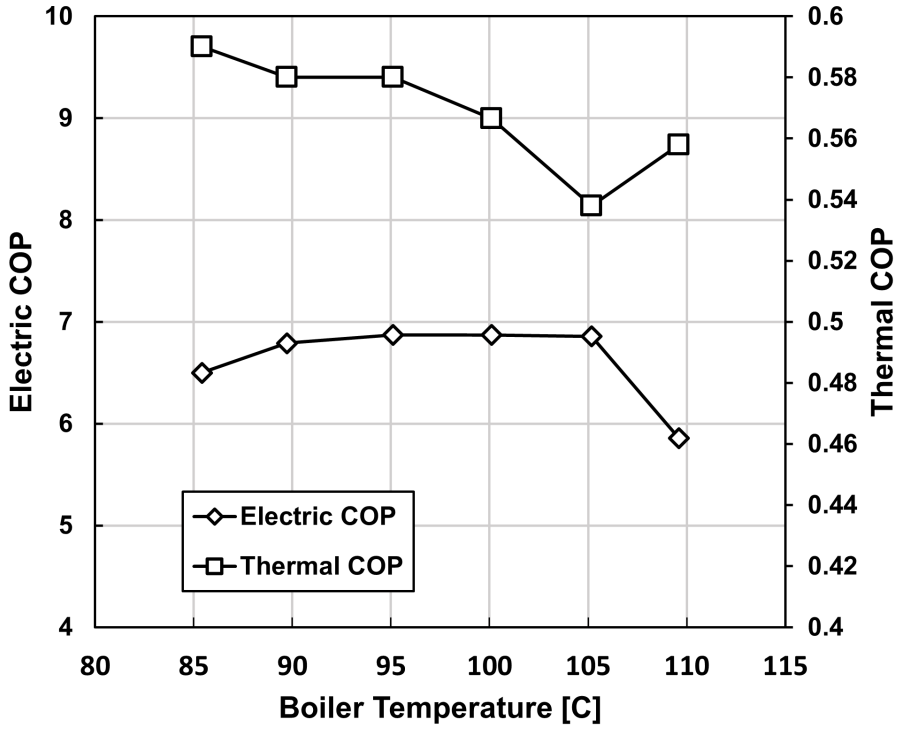

Figure 6-4: Thermal and electric COP system performance results for the variable boiler temperature study.

6.4.2. Variable Evaporator Temperature Study

The next parametric study examined the impact of variable evaporator temperatures on the operation of the hybrid ORVC system. The test facility was evaluated with the chilled water at the outlet of the evaporator ranging from 2°C to 21°C. At evaporator temperatures above 14°C, low load minimums in the internal controls of the Danfoss TT300 electric compressor prevented operation of the facility in the hybrid configuration. In realistic applications, the system would operate using just electric or thermal input in low-load operating conditions. However, this work is focused on the hybrid operation of the system, so this study was limited to the five experiments that successfully operated in the hybrid configuration with evaporator temperatures ranging from 2°C to 14°C. For these experiments, the boiler inlet temperature was maintained at 91°C, and the condenser water inlet temperature was set at 30°C. The boiler heat input duty target was 300 kW and the cooling duty target was 175 kW. The power cycle pump and electric compressor speeds

were again used to regulate the heat input and cooling duty of the system. Figure 6-5 shows cooling duty and electric compressor power results for the study.

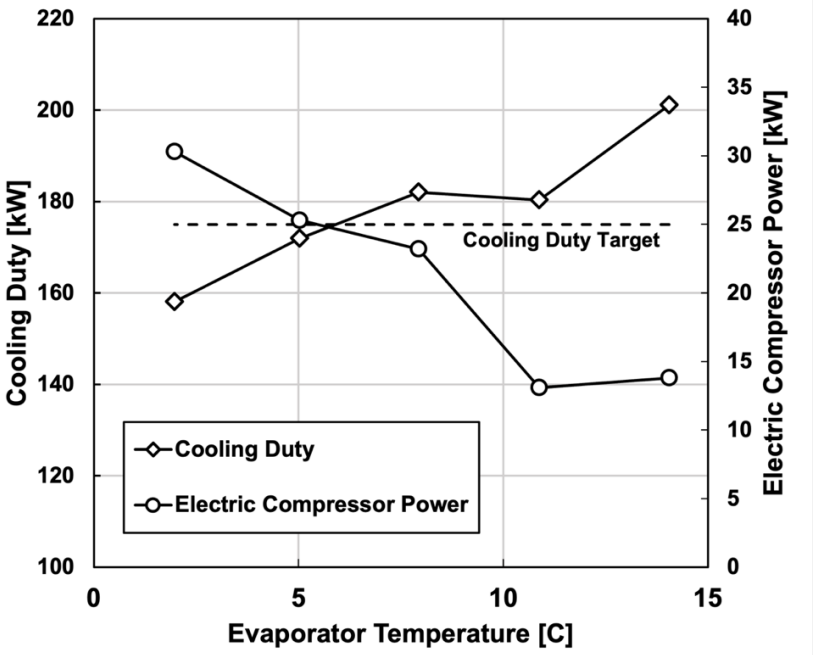

Figure 6-5: Cooling duty and electric compressor power results for the variable evaporator temperature study.

The primary observation from these results is that the cooling capacity generally increased as the evaporator temperature increased. Below 5°C, the system was unable to reach the cooling duty target, providing only 158 kW of capacity at 2°C despite operating with a relatively high level of electric compressor power (30.3 kW). Between 5°C and 12°C, the cooling duty was successfully modulated to within 4% of the 175 kW target by adjusting the electric compressor power. At 5°C, the facility produced 172 kW of cooling power with the electric compressor consuming 25.3 kW of electricity. At 12°C, the system delivered 180 kW of cooling despite the electric compressor power being reduced to 13.1 kW. Above 12°C, the electric compressor reached low load minimums and power to the device could not be reduced further. This resulted in the cooling duty increasing above the target, with the system delivering 201 kW at 15°C.

Unlike the variable boiler temperature study, the trends observed in the variable evaporator study remained consistent across the full temperature range. Similar consistency was observed in the turbomachinery results for the study. Flow rate and pressure rise data for each compressor from the five experiments was collected and corrected using the procedure described in Section 6.2.5. The results were plotted on the combined compressor map and are presented in Figure 6-6.

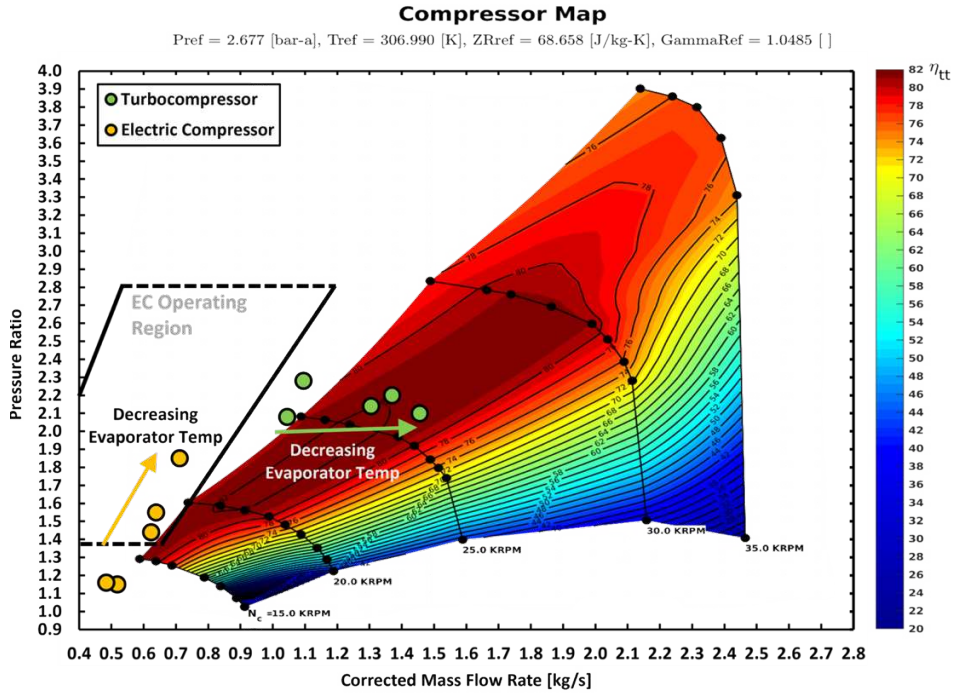

Figure 6-6: Compressor map results for the variable evaporator temperature study.

The operating limits experienced at evaporator temperatures above 14°C can be attributed to the operating locations of the electric compressor during these tests. During both the 11°C and 14°C experiments, the electric compressor operated with a pressure ratio of less than 1.2, just below the lower limit of the operating map at 1.4. While this is below the lower limit of the experimentally developed operating map, the device was able to operate at these conditions [54]. However, at evaporator temperatures above 14°C, the pressure ratio across the device was even lower which pushed the device beyond its operating limits resulting in a low load fault.

As the evaporator temperature decreased, the corrected mass flow rate for both compressors increased, shifting the operating point to the right. At 14°C, the corrected mass flow rates were 1.05 kg s^{-1} and 0.52 kg s^{-1} for the thermal and electric compressors, respectively. These values increased to 1.46 kg s^{-1} and 0.71 kg s^{-1} when the evaporator temperature decreased to 2°C. This is contrary to the actual flow rate in the cooling cycle, which was 1.21 kg s^{-1} at 14°C and decreased to 0.96 kg s^{-1} at 2°C. The change in corrected mass flow rate was driven by density changes. While the temperature at the inlet of the thermally driven compressor was consistent across the experiments due to the operation of the suction line heat exchanger, the suction pressure was influenced by the evaporator pressure which decreased as the evaporator temperature was lowered. This reduced the density at the suction of the device which increased the corrected mass flow rate. Since the turbocompressor operated with a consistent pressure ratio of about 2.2 across the five tests, the reduced evaporator pressure also influenced the electric compressor suction pressure, driving the increase in the corrected mass flow rate for the electric compressor through the same density effect.

Pressure ratio results showed different trends for the two compressors. The thermally driven compressor operated with a consistent pressure ratio of approximately 2.2 for the study. This was driven by the steady operation of the power cycle for each experiment. Since changes in the evaporator temperature have no direct impact on the power cycle, the turbine power developed during each test remained constant. The minimum turbine power was 28.1 kW, which occurred during the 8°C experiment, and the maximum power was 29.3 kW, occurring in the 14°C test. However, the total pressure ratio for the cooling cycle increased with decreasing evaporator temperature. Therefore, the increased pressure rise was delivered exclusively by the electric

compressor. The device operated with a pressure ratio of 1.15 when the evaporator temperature was 14°C. This increased to 1.85 when the evaporator temperature was 2°C.

Notably, the system was more sensitive to changes in the evaporator temperature than in the variable boiler temperature study. The impact of evaporator temperature on system performance is shown in Figure 6-7. In general, both the thermal COP and electric COP performance metrics increased with increasing evaporator temperature. At 2°C, the electric and thermal COP values were 4.71 and 0.55, respectively. At 14°C, these values increased to 11.9 and 0.69. This represents an increase of 153% for the electric COP metric and 25.5% for the thermal performance. In the variable boiler temperature study, the increase from the minimum to maximum electric COP was 17.2% and the same increase for the thermal COP was 9.2%. These results show that changes in the evaporator temperature had a more significant impact on the performance of the test facility than variations in the boiler temperature.

The slight decline in thermal performance observed between the 8°C and 11°C tests corresponded with a significant reduction in electric compressor power—from 23.2 kW down to 13.1 kW—that was executed to maintain the cooling duty target. This reduction shifted the compression load balance toward the thermally driven compressor, decreasing the thermal COP from 0.62 to 0.60. This shift also correlated with an increase in electric COP from 6.87 at 8°C to 11.0 at 11°C.

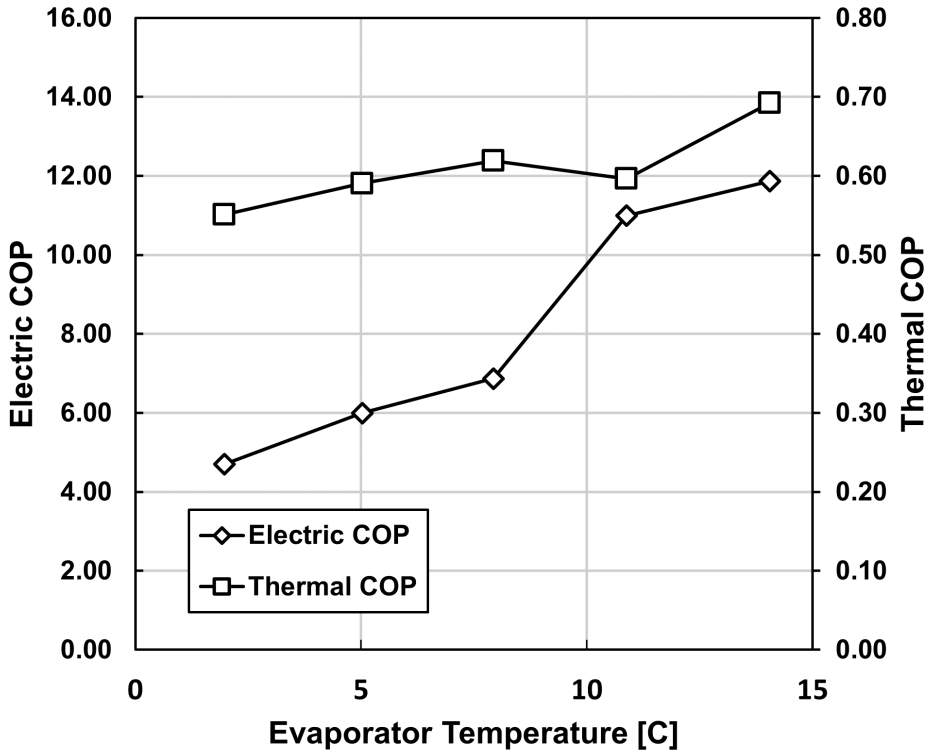

Figure 6-7: Thermal and electric COP performance results for the variable evaporator temperature study.

6.4.3. Variable Condenser Temperature Study

The final parametric study performed on the test facility investigated the impact of variable condenser temperature. The facility was tested with the temperature of the auxiliary fluid at the inlet of the condensers ranging from 21°C to 39°C. The mean of the inlet temperatures (power cycle condenser and cooling cycle condenser) was utilized for this study. While AHRI standards call for testing from 21°C to 31°C, the test facility was able to operate with condenser temperatures up to 39°C, and the limits of the study were expanded to include this range. The boiler inlet temperature was held at 91°C and the chilled water delivery temperature was set to 7°C. A heat input duty target of 250 kW was selected for this study to maintain balance between the thermal and electric compressors at lower condenser temperatures. The cooling duty target was 175 kW. At condenser temperatures below 25°C, the low load minimum for the electric compressor

prevented operation of the facility in hybrid mode. Figure **6-8** displays cooling duty, electric compressor power, and turbine power results for the study.

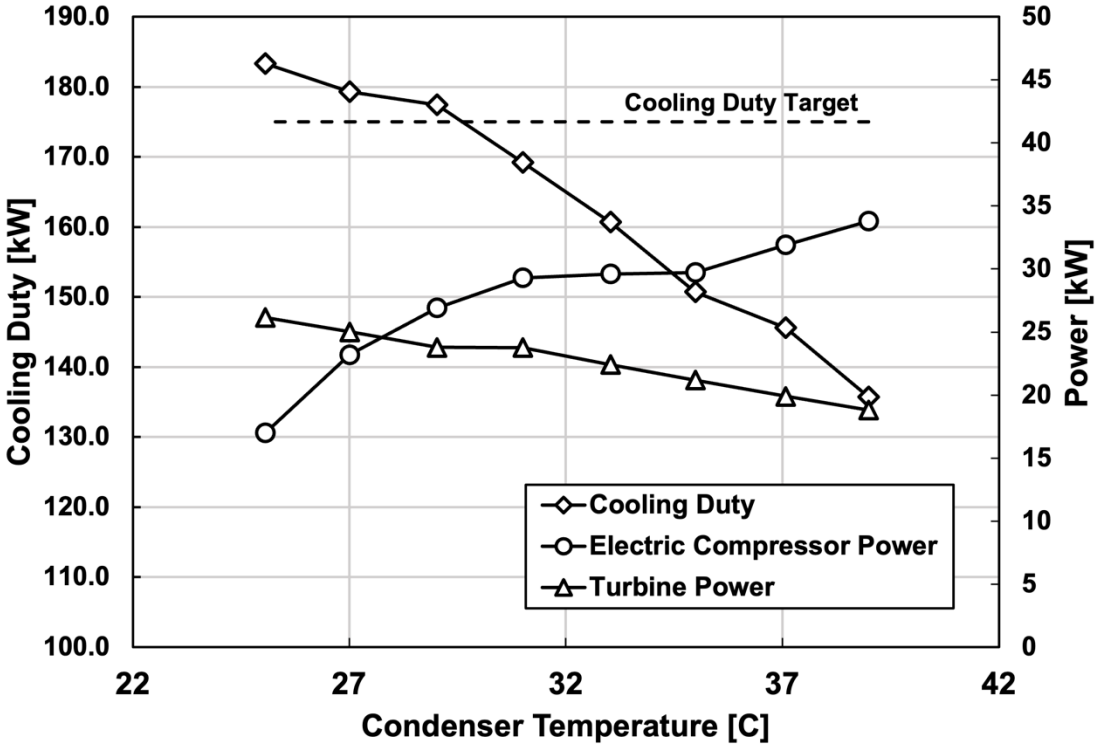

Figure 6-8: Cooling duty, electric compressor, and turbine power results for the variable condenser temperature study.

As condenser temperature increased, the test facility was unable to meet the cooling duty target. With a condenser inlet temperature of 25ºC, the facility delivered 183 kW of cooling power. Cooling duty was reduced significantly as condenser temperature increased, with just 136 kW produced when the condenser temperature reached 39ºC. Unlike the boiler inlet temperature or the chilled water deliverer temperature, changes in the condenser temperature impact both the power cycle and the cooling cycle. As condenser temperature increased, the pressure ratio across the power cycle decreased due to increased pressure in the condenser. This resulted in the reduction in turbine power shown in Figure 6-8. At 25ºC, the pressure ratio across the turbine was 2.36 and the device produced 26.2 kW of power. At 39ºC the turbine pressure ratio had decreased to 1.81 and the device produced 18.8 kW of power.

A similar effect occurred in the cooling cycle. As the condenser temperature increased, the performance of the cycle decreased. When the condenser temperature was 25°C, the total pressure ratio across the cooling cycle was 2.68 and the facility delivered 183 kW of cooling using 17.0 kW of electric compressor power. When the condenser temperature was 39°C, the higher condenser pressure had increased the cycle pressure ratio to 3.52. This contributed to the facility only producing 136 kW of cooling power, despite the electric compressor power being increased significantly to 33.8 kW.

The influence of condenser temperature on both cycles was compounded to have the significant impact on cooling duty observed in Figure 6-8 – a change of 47.6 kW over the course of the study. Turbomachinery analysis from the experiments provides some insight as to why the use of additional electric compressor input was only mildly successful in tempering not impactful enough to overcome the reduced cooling capacity decrease caused by the increased condenser temperature. Two specific experiments were performed at 39°C and analyzed in detail to illustrate this concept. One test was performed with 33.8 kW of electric compressor power as discussed above and a second experiment was performed with significantly increased electric compressor power – 43.4 kW. The results are presented in Table 6-4 and Figure 6-9.

Table 6-4: Low and high-power compressor results at 39°C condenser inlet temperature.

EC Power [kW]	*Cooling Duty [kW]*	*EC Pressure Ratio [-]*	*TC Pressure Ratio [-]*	*EC Efficiency [%]*	*TC Efficiency [%]*	*Thermal COP [-]*	*Electric COP [-]*
33.8	135.7	2.16	1.85	81.1	75.6	0.56	3.70
43.4	139.8	2.64	1.42	82.1	46.4	0.56	3.02

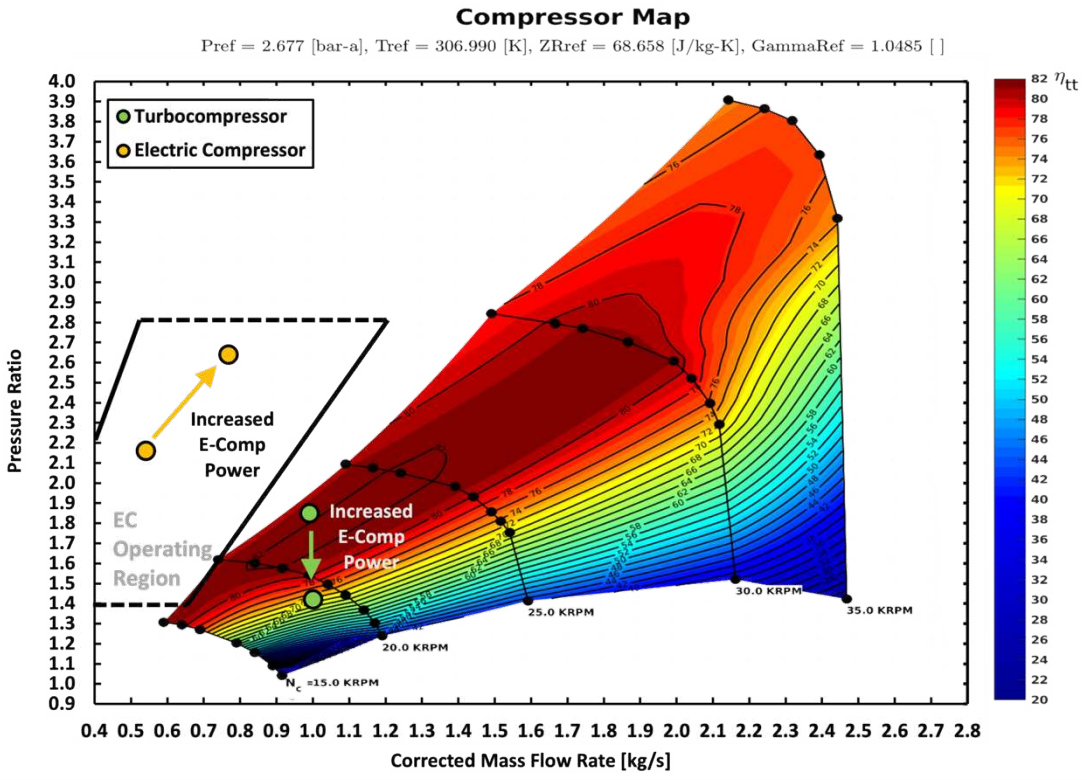

Figure 6-9: Compressor map results for low and high-power tests with condenser water inlet temperature at 39°C.

Despite the nearly 10 kW increase in electric compressor power the cooling duty produced by the system only increased by 4.1 kW. As the electric compressor power increased, the balance of compression load was shifted in favor of the electric device. This resulted in an increased pressure ratio for the electric compressor (from 2.16 to 2.64) and a decreased pressure ratio for the thermally driven compressor (from 1.85 to 1.42). As has been discussed in previous sections, the phenomenon limiting the cooling capacity is the isentropic efficiency of the thermally driven compressor. With 33.8 kW of electric compressor the thermal compressor operated with a pressure ratio of 1.85 and a corrected mass flow rate of 0.99 kg s^{-1}. This placed the device near the center of the operating map, with an isentropic efficiency of 75.6%. With 43.4 kW of electric compressor power, the pressure ratio across the thermal compressor decreased to 1.42, placing the device in the lower region of the operating map. In this region, the lines of constant efficiency are close

together, indicating that even a small decrease in pressure ratio will result in a significant decrease in efficiency. At this location, the thermally driven compressor operated with an isentropic efficiency of just 46.4%. The significant decrease in efficiency in the turbocompressor prevented an increase in cooling duty despite increased electric compressor power.

These results further highlight that operating with high electric compressor power and low thermal compressor efficiency negatively impacts the performance of the system. During the high-power test, the low turbocompressor efficiency resulted in more electric power being required to produce a similar cooling duty as the low-power test. This is evident in the electric COP results. When the electric compressor power was 33.8 kW, the electric COP was 3.70. This decreased to 3.02 when the electric compressor power increased to 43.4 kW. These results indicate that there is an optimal level of electric compressor power where the cooling capacity of the system is increased but the efficiency of the thermally driven compressor is not dramatically impacted.

Figure 6-10 displays the compressor map results from the full variable condenser temperature study. Both compressors operated within their respective operating regions except for the 25°C experiment. During this test, the pressure ratio across the electric compressor was 1.25, below the lower limit for the device. This low pressure ratio limit prevented the operation of the test facility with condenser temperatures below 25°C in the hybrid configuration. As the condenser inlet temperature increased, the operating point for the electric compressor moved up and the point for the thermally driven compressor moved down. The electric compressor ratio increased to 2.16 when the condenser temperature reached 39°C. This was driven by the increased pressure ratio across the cooling cycle and the increased power to the electric compressor at 39°C. The pressure ratio across the thermally driven compressor decreased from 2.14 when the condenser temperature

was 25°C to 1.63 at 39°C. The cause of the decreased turbocompressor pressure ratio was the reduced mechanical power produced in the turbine – 26.2 kW at 25°C and 18.8 at 39°C.

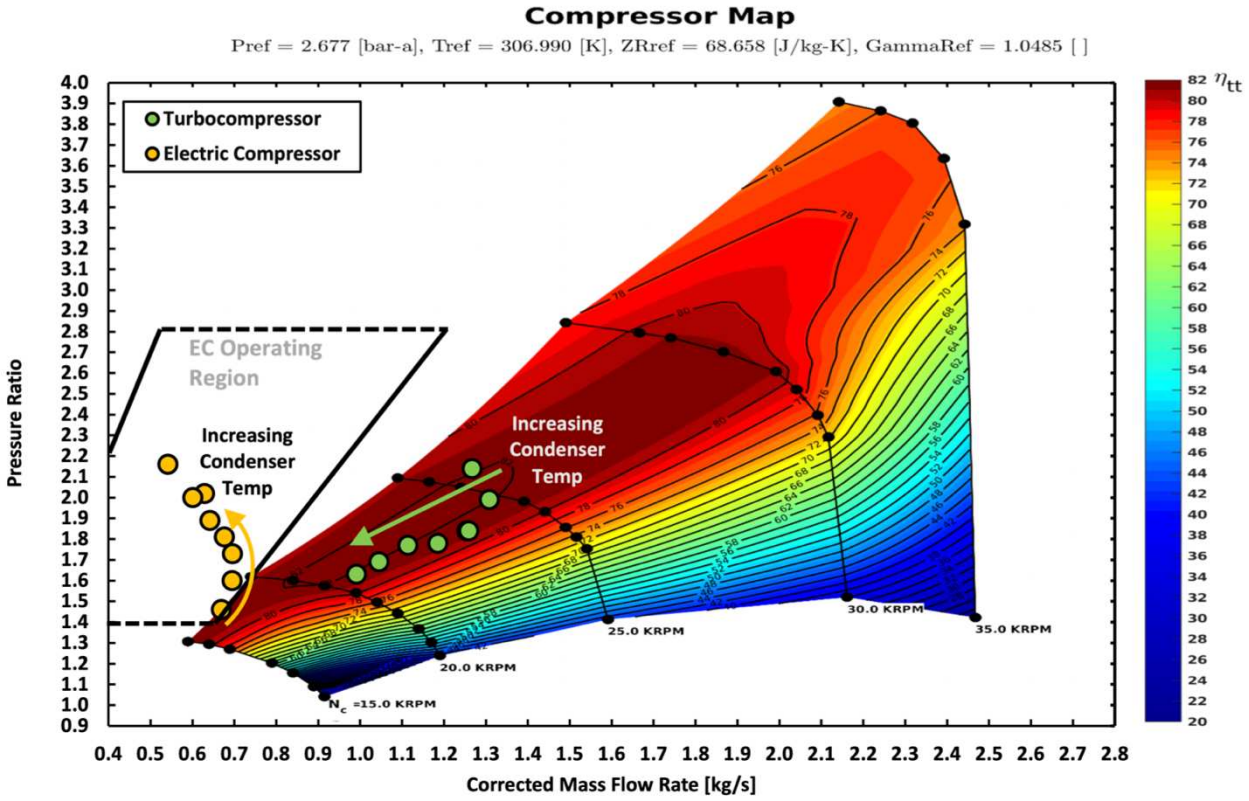

Figure 6-10: Compressor map results for the variable condenser temperature study.

The corrected mass flow rate followed similar trends for both compressors as condenser temperature increased. For the 25°C, 27°C, and 29°C tests, the corrected mass flow showed minimal changes. The thermally driven compressor operated with a corrected mass flow rate of 1.27 kg s^{-1} at 25°C and a flow rate of 1.26 kg s^{-1} at 29°C. Similarly, the corrected mass flow rate for the electric compressor was 0.60 kg s^{-1} at 25°C and 0.69 kg s^{-1} at 29°C. The slight increase for the electric compressor was a result of reduced fluid density. This was caused by the decreased pressure at the electric compressor suction associated with the decrease in pressure rise across the thermally driven compressor. Above condenser temperatures of 29°C, the trend changed for both devices. At this point, the electric compressor input was no longer able to maintain cooling duty

at the 175 kW target due to decreased turbocompressor efficiency. The actual mass flow rate decreased significantly, dropping from 1.08 kg s^{-1} at 29°C to 0.87 kg s^{-1} at 39°C. This caused decreases in the corrected mass flow rates for both devices. At 39°C, the corrected flow rate had decreased to 0.54 kg·s^{-1} for the electric compressor and 0.99 kg·s^{-1} for the thermally driven compressor.

Figure 6-11 displays the system performance metrics for the study. In general, the performance of the system decreased as the condenser inlet temperature increased. At 25°C, the thermal COP was 0.72 and the electric COP was 9.19. At 39°C the thermal COP had decreased to 0.56 and the electric COP had decreased to 3.70. This is a comparable system impact to what was observed in the variable evaporator temperature study. In this study, the electric COP changed by 148% over the range of experiments, which is comparable to the 153% change observed in the variable evaporator temperature study. Similarly, for the thermal COP metric, the 28.6% change observed in this study was similar to the 25.5% change observed in the variable evaporator study.

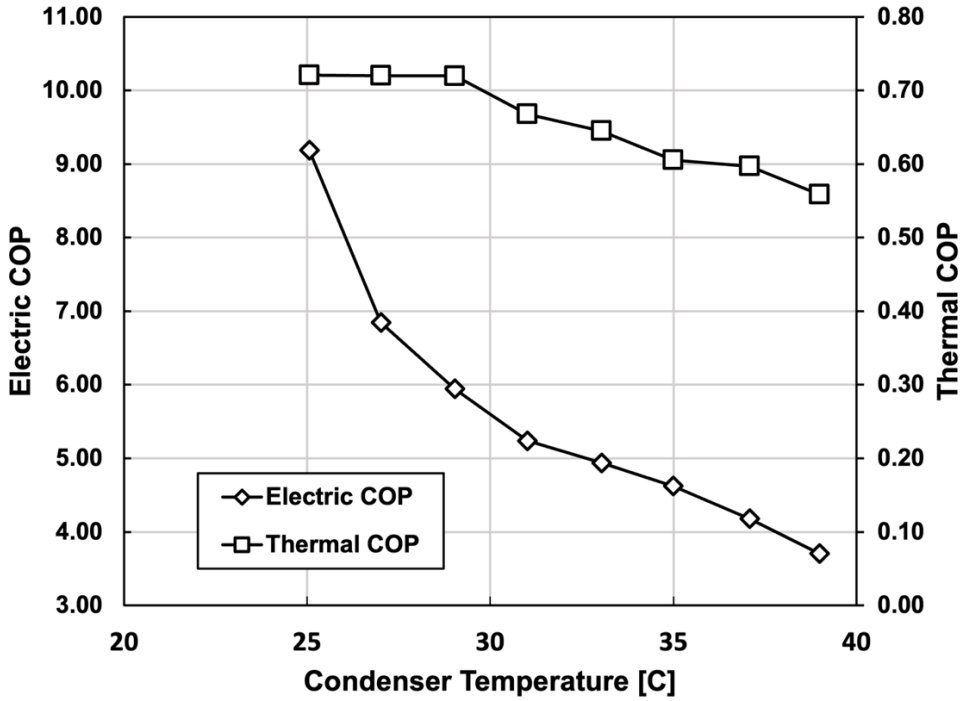

Figure 6-11: System performance results for the variable condenser temperature study.

6.5. Integrated Part Load Value Study

The final study performed on the test facility was a series of experiments designed to quantify the integrated part load value or IPLV. The four tests that make up the IPLV study were discussed in the methods section and were presented in Table 6-2. In general, each of the tests represents operation at 100%, 75%, 50%, and 25% of the design point operating capacity. The test facility failed to operate in hybrid mode for the 50% and 25% tests. At these conditions, the load on the electric compressor was low and the minimum load safety controls prevented the device from operating in the hybrid configuration. To enable completion of the study, the 50% and 25% load experiments were completed in thermal cooling mode using just the turbocompressor and in electric cooling mode using only the electric compressor. Compressor map data from the resulting six experiments is shown in Figure 6-12.

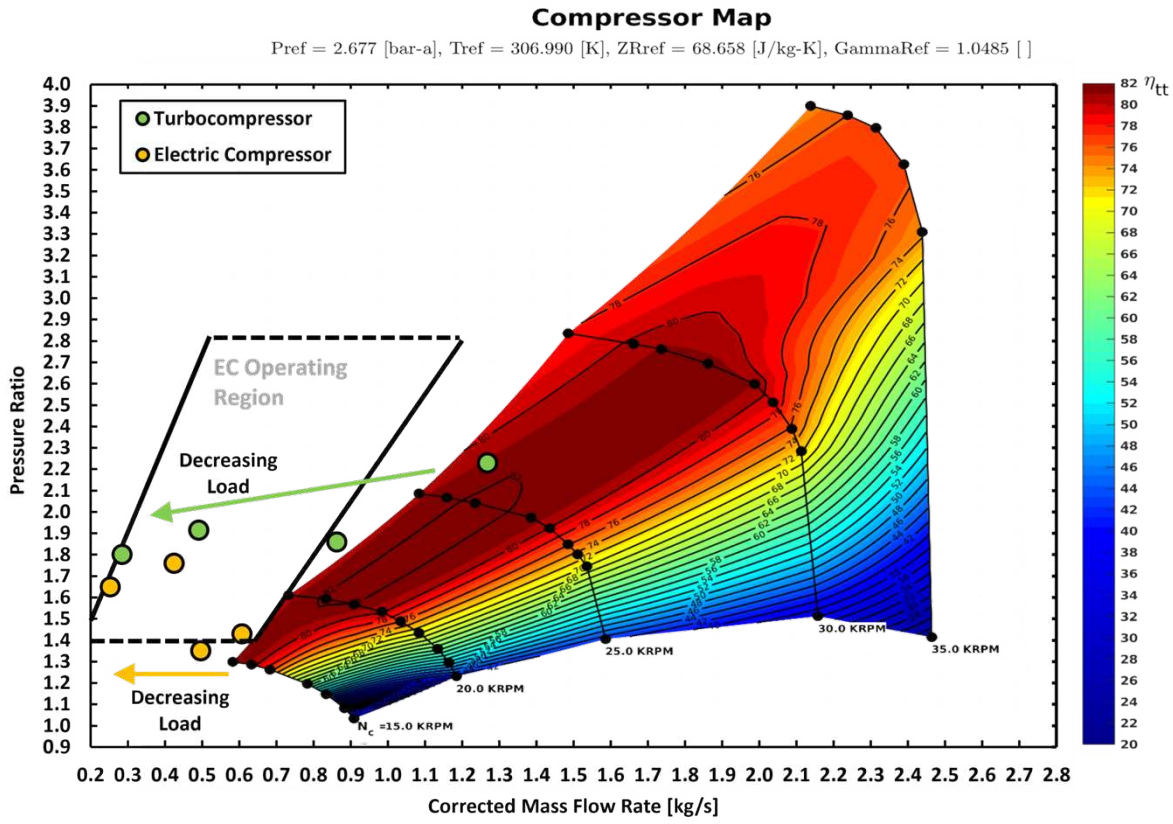

Figure 6-12: Compressor map results for the IPLV study.

At 100% load, both compressors operated within the compressor map. The thermal compressor operated with a pressure ratio of 2.12 and a corrected mass flow rate of 1.27 kg s^{-1}. At 75% load, these values decreased to 1.76 and 0.86 kg s^{-1}. The decrease was driven by a combination of reduced turbine power from the power cycle (due to decreased heat input), reduced cooling cycle pressure ratio caused by decreased condenser temperature, and lower cooling cycle mass flow rate/capacity. Similarly, the electric compressor operated with a pressure ratio of 1.43 and a corrected mass flow rate of 0.61 kg s^{-1} at 100% load. This decreased to 1.35 and 0.50 kg s^{-1} at 75% load. Less electric compressor power was required at 75% load, resulting in the reduced pressure ratio and corrected flow rate observed for the device. The low 1.35 pressure ratio observed in the 75% load test prevented operation below 75% load in hybrid cooling mode. Further load reduction would have reduced the pressure ratio further, well below the minimum pressure ratio of the operating region for the device.

For the 50% and 25% load experiments, the facility was operated with one compressor at a time. The increase in pressure ratio observed for both devices from the 75% load test to the 50% load test is a result of only one device delivering the whole cycle pressure rise in the 50% experiment. From the 50% load test to the 25% test, the pressure ratio and corrected mass flow rate decreased for both devices. The reduced capacity target resulted in lower mass flow rates in the cooling cycle. In thermal cooling mode the flow rate decreased by 0.20 kg s^{-1} and in electric cooling mode the decrease was 0.17 kg s^{-1}. The reduced flow rate reduced the corrected mass flow rate for each device and resulted in fewer pressure losses in the system, decreasing the pressure ratio across each compressor.

The operating points fell within the operating region of the electric compressor for all four experiments. However, the 25% and 50% load experiments resulted in operating locations that

were well into the surge region for the thermally driven compressor. Despite this, the device operated successfully, and no signs of audible surge were observed during the tests. The compressor map was developed by the manufacturer using computational fluid dynamics; therefore, the model may not have been evaluated at the low pressure ratios and corrected mass flow rates characteristic of low-load conditions like those in these experiments.

Table 6-5 displays the system performance for each of the IPLV tests. The 75% load test resulted in the highest system efficiency for both the electric COP and thermal COP metrics, with values reaching 8.58 and 0.73, respectively. At lower loads, the system performance was lower, as the compression load was not shared between the thermal and electric devices. The results from all the experiments were used in Equation 1 to calculate IPLV results based on both electric and thermal COP.

Table 6-5: Integrated part load value results for the hybrid ORVC test facility.

Test	*Electric COP*	*Thermal COP*
100% ($Hybrid\ Mode$)	7.04	0.63
75% ($Hybrid\ Mode$)	8.58	0.73
50% ($Electric\ Only$)	6.67	-
50% ($Thermal\ Only$)	-	0.43
25% ($Electric\ Only$)	6.04	-
25% ($Thermal\ Only$)	-	0.30
IPLV	**7.40**	**0.56**

6.6. System Improvements

The results presented throughout this section provide insight into the potential of the hybrid ORVC system. However, the results also identify some limitations of the test facility that constrained the operating range and performance of the prototype. Many of the limitations observed with the test facility stemmed from the compressors selected for the system. Utilizing two compressors that were designed for different fluids which was the cause of many of the operational challenges observed in this research.

Many of the operating range limitations identified in this research were associated with the low-load operating constraints of the Danfoss TT300 electric compressor. This includes operating at evaporator temperatures above 14°C, condenser temperatures below 25°C, and loads below 75% in the hybrid configuration. In all these cases, the pressure ratio across the electric compressor dropped below the lower limit of the operating range for the TT300 unit. Selecting a different compressor that was designed for low lift operation (below PR=1.4) could enable operation beyond the limits identified in this study.

Another implication of the improperly matched compressors was that the test facility had to be operated at a reduced capacity to enable the hybrid configuration. This was discussed in detail in Chapter 4. Selecting an electric compressor that enabled higher capacity operation could also improve performance in off-design operation. Increased design point capacity would increase the capacities for the IPLV experiments yielding improved efficiency and hybrid operation at lower turn-down ratios. Additionally, higher capacity operation could improve the performance of the thermally driven compressor. In this work, when operating with a capacity target of 175 kW, the highest efficiency region of the thermal compressor map extends from a pressure ratio of 1.8 to a pressure ratio of 2.1, a range of 0.3. At higher capacity, the high-efficiency region of the

compressor map expands slightly, covering a pressure range of 0.4. This would expand the operating range of the compressor before the isentropic efficiency effects identified in this study would begin to limit the electric compressor's ability to increase the system cooling capacity.

Alternative electric compressor selection could improve the performance and operating range of the system. An improved selection would more closely match the operating range of the thermally driven compressor. It would also be designed to operate with R1234ze(E) as a working fluid and at the lower pressures associated with the fluid. The device would also ideally be designed to operate at low lift conditions, with pressure ratios below 1.4. A more optimal compressor selection could yield similar performance while alleviating the operating range limitations discussed in this work.

6.7. Chapter Summary

This chapter assessed the hybrid ORVC test facility performance across off-design operating conditions through five independent studies. These studies examined the effects of electric compressor power, heat input, cooling delivery, and heat rejection temperatures, and quantified the integrated part load value (IPLV). Results showed that increasing electric compressor power improved cooling duty, but its effectiveness depended heavily on compressor isentropic efficiency, a key factor influencing overall system performance.

In tests varying boiler, evaporator, and condenser temperatures, system efficiency fluctuated as parameters changed. Higher boiler inlet temperatures generally reduced the required electric power, though ORC flow rate effects impacted this trend at temperatures above 100°C. The facility successfully operated with evaporator outlet temperatures from 2°C to 14°C, and efficiency decreased as the evaporator temperature was reduced. Similarly, higher condenser temperatures reduced efficiency and cooling capacity, despite increased electric input.

The IPLV study highlighted a significant limitation: at 25% and 50% load, low lift constraints prevented hybrid operation, requiring reliance on either the electric or thermal compressor alone. Performance at these lower loads was likely degraded, with IPLV results yielding an electric COP of 7.40 and a thermal COP of 0.56.

CHAPTER 7. Conclusions and Recommendations for Further Work

Over the course of this research effort, a thorough investigation into the potential of a novel cooling system, hybrid electric organic Rankine vapor compression technology, has been conducted. Hybrid ORVC technology has the potential to be a transformative cooling alternative that can realize the efficiency, economic, and emissions benefits of thermally driven cooling technologies. By integrating a pathway for on-demand electric input into the system, the hybrid ORVC concept can overcome the established challenges that face thermally driven chillers when operating in variable conditions. Utilizing electric input to overcome these variations allows the system to maximize the benefit of utilizing thermal input while still providing reliable, on-demand cooling power.

In this work, a new configuration of the hybrid ORVC concept has been presented that utilizes independent electric and thermally driven compressors. An experimentally based thermodynamic and turbomachinery model of the system was developed to evaluate three different compressor configurations and simulate the performance of the system across a wide range of design and off-design operating conditions. A large-scale prototype test facility was developed to evaluate and validate the concept experimentally. The test facility was configured to evaluate the different compressor arrangements and study the associated turbomachinery implications. Comprehensive experiments conducted at design point operating conditions revealed the facility performance characteristics across the entire spectrum of heat input scenarios, ranging from fully thermal to fully electric operation. The prototype was also tested at off-design conditions, which incorporated parametric studies examining system response to variations in heat supply, heat rejection, cooling delivery temperatures, and electric compressor power. Furthermore, the research

quantified the facility part-load performance through the estimation of the integrated part-load value (IPLV). Through these activities, a comprehensive series of insights was gained that improves understanding of the hybrid ORVC concept.

Beginning with the simulation effort, results yielded a few important findings. Firstly, for the system and equipment simulated, the TC1 compressor configuration was the optimal choice. Placing the electric compressor second in the flow path enabled operation across a wider range of heat inputs. This configuration mitigated the choke limitations of the electric compressor by partially compressing the fluid with the thermally driven compressor before it reached the electric compressor. The increased density of the partially compressed fluid allowed the device to flow more mass for the same volumetric flow rate, effectively moving the operating point away from the choke limit for the device.

When simulated in this configuration, the system delivered efficient performance over a wide range of conditions. The operating range was large at design point conditions, with the system able to operate in fully thermal and fully electric cooling modes, as well as hybrid cooling mode with heat inputs ranging from 100 kW to 327 kW. Performance remained high across the full range of design conditions. Thermal COP improved in hybrid operation over purely thermal operation ($COP_{\text{th}} = 0.44$), with the thermal COP reaching 1.6 at the highest point. The same was true for the electric COP performance metric, with values reaching 18.2 in hybrid cooling mode, higher than the purely electric baseline ($COP_{\text{e}} = 5.86$). The operating range was also wide in off-design conditions, with large acceptable operating ranges for heat input temperature (85°C-117°C), cooling delivery temperature (2.1°C – 10.7°C), and heat rejection temperature (26.6°C – 30.9°C). The performance of the system was most sensitive to changes in the cooling delivery temperature, with the electric COP varying from 7.7 to 11.4 across the range of temperatures simulated.

Additionally, these simulations highlighted the critical importance of properly matching the electric and thermally driven compression devices. Size and operating range differences between the electric and thermally driven devices impacted system efficiency and the total cooling capacity of the system. The performance reported in these simulations was only possible with the compression equipment arranged in the TC1 configuration. Due to the mismatch between the devices analyzed, the PC and EC1 configurations failed to yield solutions that feasibly operated at the conditions evaluated in these simulations. This highlighted the importance of turbomachinery analysis for the analysis of electrified ORVC systems.

Many of the insights gained from the simulation study were validated in the design point experimental study. In the compressor configuration comparison experiments, two of the three configurations failed to reach the testing targets. In the parallel configuration, the electric compressor was unable to reach the suction pressure required for operation at the targeted temperatures. This was due to the lower operating pressures of R1234ze(E) when compared with the original design fluid (R134a) for the TT300 compressor. In the series configuration with the electric compressor first in the flow path, the system was unable to reach the 175 kW capacity target due to choke limitations in the electric compressor. In the series configuration with the turbocompressor first, the mass flow limitations were avoided, and the facility successfully reached the testing targets. This confirmed the findings of the simulations. In this TC1 compressor configuration, the test facility delivered 176 kW of cooling from 257 kW of thermal input and 20.1 kW of electric input, with the electric and thermally driven compressors splitting the compression load.

In the variable heat supply experiments, the test facility operated in hybrid cooling mode with heat input ranging from 113 kW to 331 kW. At lower heat input, the suction pressure at the

electric compressor was below the operating limit, and at higher heat input, the pressure ratio for the electric compressor was below the operating map, preventing successful operation. The system performed with high thermal COP (1.02) and low electric COP (3.80) at 113 kW heat input. At higher heat input (331 kW), the facility had lower thermal COP (0.54) and higher electric COP (8.76). System performance was improved over purely thermal (COP_{th} = 0.42) and purely electric (COP_e = 4.55) operation, except for the electric COP at very low levels of heat input. At the two lowest levels of heat input (113 kW and 136 kW) the pressure ratio across the turbocompressor decreased below 1, resulting in higher load on the electric compressor and degraded system performance.

These results validated the technology experimentally and characterized the performance at standard conditions. However, the performance away from these conditions was still unknown. The series of five off-design and variable conditions studies provided some insight into the operation of the technology away from standard design point conditions.

In the electric compressor power study, the prototype was evaluated at design point operating conditions (heat input at 91°C, cooling delivered at 7°C, heat rejected at 30°C, and 175 kW cooling capacity) with the electric compressor power ranging from 19.2 kW to 33.9 kW. It was observed that increasing the electric input increased the system's cooling duty; however, the effectiveness of the additional electric power was largely dependent on the isentropic efficiency of the compressors. These efficiencies were a theme throughout this study as one of the most important factors impacting the performance of the system.

In the variable boiler inlet temperature study, the test facility operated with temperatures ranging from 85°C to 110°C. Performance was high (COP_e= 6.87 and COP_{th}=0.57 at 100°C) and the electric compressor power required to deliver the cooling duty target generally decreased as

boiler temperature increased. However, this trend reversed when the power cycle flow rate was reduced to constrain the increasing boiler heat duty. In the variable evaporator outlet temperature study, the facility successfully operated with chilled water delivered at temperatures from 2°C to 14°C. Above 14°C, low lift limitations of the electric compressor prevented operation. The electric compressor input helped to temper variations in cooling duty caused by the variable evaporator temperature, but the facility was unable to maintain the 175 kW target across the full testing range. The benefit of increased electric compressor power was limited by reduced isentropic efficiency in the turbocompressor. Performance was high but variable with COP_e increasing from 4.71 to 11.9 and COP_{th} increasing from 0.55 to 0.69 as the evaporator temperature increased from 2°C to 14°C. In the variable condenser inlet temperature study, the prototype operated with temperatures ranging from 25°C to 39°C. Low lift limitations again impacted the operating range, preventing operation below 25°C. Reductions in the isentropic efficiency of the thermally driven compressor at higher condenser temperatures limited cooling capacity to below the 175 kW target, despite increased electric compressor power. System efficiency was variable, with COP_e decreased from 9.19 to 3.70 and COP_{th} changing from 0.72 to 0.56 as the condenser temperature increased across the experimental range.

The IPLV experiments identified a limitation of the configuration. At low capacities (25% and 50% load) the facility was unable to operate in the hybrid configuration due to the low lift limitations of the electric compressor. The facility was instead operated with just the electric or thermal compressor at the low load points. The experiments yielded IPLV results based on electric COP and thermal COP of 7.40 and 0.56, respectively. However, performance was likely degraded at 25% and 50% due to the low-capacity operation and inability to operate in the hybrid configuration.

Through this series of research activities, the understanding of hybrid ORVC cooling technology has been expanded significantly. In summary, this investigation:

- Presented a new hybrid ORVC configuration based on independent electric and thermally driven compressors.
- Identified links between compressor operating ranges and optimal compressor arrangement based on the equipment evaluated.
- Simulated the performance possibilities associated with shifting compressor load between electric and thermal drivers.
- Experimentally validated the hybrid ORVC concept and demonstrated the performance of the system across a range of operating conditions.
- Demonstrated the expanded operational range enabled by the hybrid configuration.
- Discovered operating range and performance limitations caused by poorly matched compressor operating maps.
- Identified compressor efficiency as a key driver impacting both operating range and system performance.

7.1. Recommendations for Future Work

Findings from the current study identified some limitations that could not be investigated within the scope of the current work. The following proposed research could continue to expand the understanding of hybrid ORVC technology:

- The compression equipment utilized for this investigation was poorly matched for this application due to differing design working fluids. Careful selection of two well-matched compressors could yield further improved performance and operating

range. An experimental investigation with well-matched compressors should be completed to demonstrate the full potential of the hybrid ORVC configuration.

- Much of this study was limited to the evaluation of the TC1 series compressor configuration due to the choke constraints of the electric compressor used for this investigation. A future study with properly matched turbomachinery could investigate the performance and tradeoffs associated with the EC1 series compressor configuration or the parallel compressor configuration. These other configurations may have benefits or limitations that were not apparent with the TC1 configuration investigated in this study.
- Independent compressors were utilized for this investigation while previous research has evaluated an integrated expander-motor-compressor electrification strategy. It would be useful to evaluate that integrated configuration across the full range of design and off-design conditions for HVAC applications. Understanding the tradeoffs between the two configurations would help guide further research and development.
- Further investigation of potential applications should be performed to identify potential markets for the technology. Potential applications include industrial facilities that have available waste heat and a demand for process cooling, such as food and beverage manufacturing facilities or metal processing plants. Large scale commercial applications with large cooling loads such as data centers and hospitals could also be a beneficial application. This technology could be advantageous for marine applications with waste heat availability and footprint constraints.

- Turbomachinery analysis should also be applied to the integrated expander-motor-compressor concept. Advanced analysis methods like those used in this investigation could reveal some limitations of the concept. It is possible that introducing electric input in an integrated machine could have a detrimental impact on the aerodynamic performance of the device.
- Throughout the analysis presented in this work, the system efficiency was typically the final metric used to indicate performance. It would be beneficial to extend the analysis conducted in this work to energy savings, cost reduction, and decarbonization metrics. This could involve applying the technology in a case study or pilot demonstration. A study like this could provide a concrete quantification of the more tangible benefits of the technology.

REFERENCES

[1] Kalanki A, Winslow C, Campbell I. Global Cooling Prize: Solving the Cooling Dilemma. RMI 2021;April.

[2] International Energy Agency (IEA). The Future of Cooling - Opportunities for energy-efficient air conditioning 2018:92.

[3] Goetzler W, Guernsey M, Young J, Fuhrman J, Abdelaziz O. The Future of Air Conditioning for Buildings. 2016.

[4] Environmental Protection Agency - SNAP. TRANSITIONING TO LOW-GWP ALTERNATIVES in Residential and Commercial Air Conditioning and Chillers. n.d.

[5] Poulopoulos SG. Atmospheric Environment. Environment and Development 2016:45–136. https://doi.org/10.1016/B978-0-444-62733-9.00002-2.

[6] U.S. Energy Information Administration. Residential Energy Consumption Survey (RECS). 2015.

[7] U.S. Energy Information Administration. Commercial Buildings Energy Consumption Survey (CBECS). 2018.

[8] Shah N, Wei M, Letschert V, Phadke A. Benefits of Energy Efficient and Low-Global Warming Potential Refrigerant Cooling Equipment. E-Scholarship Repository, Berkeley, CA (United States): 2019. https://doi.org/10.2172/1559243.

[9] Lawrence Livermore National Lab, United States Department of Energy. Estimated U.S. Energy Consumption Flowchart. 2021.

[10] Gingerich DB, Mauter MS. Quantity, Quality, and Availability of Waste Heat from United States Thermal Power Generation. Environ Sci Technol 2015;49:8297–306. https://doi.org/10.1021/es5060989.

[11] United States Department of Energy. Waste Heat Recovery Basics n.d.

[12] Xu ZY, Wang RZ, Yang C. Perspectives for low-temperature waste heat recovery. Energy 2019;176:1037–43. https://doi.org/10.1016/J.ENERGY.2019.04.001.

[13] United States Department of Energy. Industrial Decarbonization Roadmap. 2022.

[14] U.S. Department of Energy. Combined Heat and Power (CHP) Technical Potential in the United States. 2016.

[15] Bagherian MA, Mehranzamir K. A comprehensive review on renewable energy integration for combined heat and power production. Energy Convers Manag 2020;224:113454. https://doi.org/10.1016/J.ENCONMAN.2020.113454.

[16] U.S. Department of Energy, ICF Inc. U.S. Department of Energy Combined Heat and Power and Microgrid Installation Databases. ENERGYGOV 2023. https://doe.icfwebservices.com/index (accessed November 28, 2023).

[17] Núñez T. THERMALLY DRIVEN COOLING: TECHNOLOGIES, DEVELOPMENTS AND APPLICATIONS. vol. 1. 2010.

[18] Garousi Farshi L, Seyed Mahmoudi SM, Rosen MA. Analysis of crystallization risk in double effect absorption refrigeration systems. Appl Therm Eng 2011;31:1712–7. https://doi.org/10.1016/J.APPLTHERMALENG.2011.02.013.

[19] Liao X, Radermacher R. Absorption chiller crystallization control strategies for integrated cooling heating and power systems. International Journal of Refrigeration 2007;30:904–11. https://doi.org/10.1016/J.IJREFRIG.2006.10.009.

[20] Wu W, Wang B, Shi W, Li X. An overview of ammonia-based absorption chillers and heat pumps. Renewable and Sustainable Energy Reviews 2014;31:681–707. https://doi.org/10.1016/J.RSER.2013.12.021.

[21] United States Department of Energy. Absorption Chillers for CHP Systems. Advanced Manufacturing Office 2017:3–6.

[22] US EIA. Updated Buildings Sector Appliance and Equipment Costs and Efficiencies 2018:740.

[23] Nasir MT, Kim KC. Working fluids selection and parametric optimization of an Organic Rankine Cycle coupled Vapor Compression Cycle (ORC-VCC) for air conditioning using low grade heat. Energy Build 2016;129:378–95. https://doi.org/10.1016/J.ENBUILD.2016.07.068.

[24] Tchanche BF, Lambrinos G, Frangoudakis A, Papadakis G. Low-grade heat conversion into power using organic Rankine cycles – A review of various applications. Renewable and Sustainable Energy Reviews 2011;15:3963–79. https://doi.org/10.1016/J.RSER.2011.07.024.

[25] Johnson Controls. York Model YMC2 Mod B Magnetic Bearing Centrifugal Liquid Chillers - Engineering Guide. 2024.

[26] Johnson Controls. York - Absorption Chillers n.d. https://www.york.com/commercial-equipment/chilled-water-systems/absorption-chillers (accessed March 5, 2023).

[27] Gibson SC, Young D, Bandhauer TM. Technoeconomic Optimization of Turbocompression Cooling Systems 2017. https://doi.org/10.1115/IMECE2017-70934.

[28] Young D, Gibson SC, Bandhauer TM. Working Fluid Selection and Technoeconomic Optimization of a Turbocompression Cooling System. J Therm Sci Eng Appl 2018;10. https://doi.org/10.1115/1.4041197.

[29] Garland SD, Noal J, Bandhauer TM. Experimentally validated modeling of a turbo-compression cooling system for power plant waste heat recovery. Energy 2018;156:32–44.

[30] Grauberger A, Young D, Bandhauer T. Off-design performance of an organic Rankine-vapor compression cooling cycle using R1234ze(E). Appl Energy 2022;321:119421. https://doi.org/10.1016/J.APENERGY.2022.119421.

[31] Grauberger A, Young D, Bandhauer T. Experimental validation of an organic rankine-vapor compression cooling cycle using low GWP refrigerant R1234ze(E). Appl Energy 2022;307:118242. https://doi.org/10.1016/J.APENERGY.2021.118242.

[32] Shirazi A, Taylor RA, Morrison GL, White SD. Solar-powered absorption chillers: A comprehensive and critical review. Energy Convers Manag 2018;171:59–81. https://doi.org/10.1016/j.enconman.2018.05.091.

[33] Porumb R, Porumb B, Balan M. Numerical Investigation on Solar Absorption Chiller with LiBr-H2O Operating Conditions and Performances. Energy Procedia, vol. 112, Elsevier Ltd; 2017, p. 108–17. https://doi.org/10.1016/j.egypro.2017.03.1071.

[34] Gomri R. Investigation of the potential of application of single effect and multiple effect absorption cooling systems. Energy Convers Manag 2010;51:1629–36. https://doi.org/10.1016/j.enconman.2009.12.039.

[35] Xia X, Liu Z, Wang Z, Sun T, Zhang H. Multi-layer performance optimization based on operation parameter-working fluid-heat source for the ORC-VCR system. Energy 2023;272. https://doi.org/10.1016/j.energy.2023.127103.

[36] Xiao X, Zhao W, Wang W, Zhang W, Bu X, Wang L, et al. Analysis of solar direct-driven organic rankine cycle powered vapor compression cooling system combined with electric motor for office building air-conditioning. Energy Engineering: Journal of the Association of Energy Engineering 2021;118:89–101. https://doi.org/10.32604/EE.2020.014016.

[37] Jiang H, Rong Y, Zhou X, Fang S, Wang K, Zhi X, et al. Performance assessment of an organic Rankine–Vapor compression cycle (ORC-VCR) for Low-Grade compression heat recovery. Energy Convers Manag 2023;275. https://doi.org/10.1016/j.enconman.2022.116492.

[38] Zhou X, Fang S, Zhang H, Xu Z, Jiang H, Rong Y, et al. Dynamic characteristics of a mechanically coupled organic Rankine-vapor compression system for heat-driven cooling. Energy 2023;280. https://doi.org/10.1016/j.energy.2023.128195.

[39] Prigmore D, Barber R. Cooling with the sun's heat Design considerations and test data for a Rankine Cycle prototype. Solar Energy 1975;17:185–92. https://doi.org/10.1016/0038-092X(75)90058-4.

[40] Demierre J, Favrat D, Schiffmann J, Wegele J. Experimental investigation of a Thermally Driven Heat Pump based on a double Organic Rankine Cycle and an oil-free Compressor-Turbine Unit. International Journal of Refrigeration 2014;44:91–100. https://doi.org/10.1016/J.IJREFRIG.2014.04.024.

[41] Liang Y, Mckeown A, Yu Z, Alshammari SFK. Experimental study on a heat driven refrigeration system based on combined organic Rankine and vapour compression cycles. Energy Convers Manag 2021;234:113953. https://doi.org/10.1016/J.ENCONMAN.2021.113953.

[42] Biancardi FR, Sitler JW, Melikian G. Development and test of solar Rankine cycle heating and cooling systems. International Journal of Refrigeration 1982;5:351–60. https://doi.org/10.1016/0140-7007(82)90057-3.

[43] Wang H, Peterson R, Harada K, Miller E, Ingram-Goble R, Fisher L, et al. Performance of a combined organic Rankine cycle and vapor compression cycle for heat activated cooling. Energy 2011;36:447–58. https://doi.org/10.1016/J.ENERGY.2010.10.020.

[44] Grauberger AM, Bandhauer T, Quinn J, Windom B, Sharvelle S. DISSERTATION EXPERIMENTAL INVESTIGATION OF AN ADVANCED ORGANIC RANKINE VAPOR COMPRESSION CHILLER Submitted by. 2022.

[45] Rankine cycle and variants. Power Generation Technologies for Low-Temperature and Distributed Heat, Elsevier; 2023, p. 49–161. https://doi.org/10.1016/B978-0-12-818022-8.00001-6.

[46] Dincer I, Rosen MA. EXERGY ANALYSIS OF STEAM POWER PLANTS. EXERGY, Elsevier; 2007, p. 229–56. https://doi.org/10.1016/B978-008044529-8.50014-8.

[47] Chen H, Goswami DY, Stefanakos EK. A review of thermodynamic cycles and working fluids for the conversion of low-grade heat. Renewable and Sustainable Energy Reviews 2010;14:3059–67. https://doi.org/10.1016/j.rser.2010.07.006.

[48] Mohammad ATh, Mat S Bin, Sulaiman MY, Sopian K, Al-abidi AA. Survey of liquid desiccant dehumidification system based on integrated vapor compression technology for building applications. Energy Build 2013;62:1–14. https://doi.org/10.1016/j.enbuild.2013.03.001.

[49] Klein SA, Reindl DT, Brownell K. Refrigeration system performance using liquid-suction heat exchangers. International Journal of Refrigeration 2000;23:588–96. https://doi.org/10.1016/S0140-7007(00)00008-6.

[50] Gardner JF. The Vapor Compression Cycle: A Review, 2021, p. 27–42. https://doi.org/10.1007/978-3-031-79705-7_3.

[51] Scotti Del Greco A, Tapinassi L. On the Combined Effect on Operating Range of Adjustable Inlet Guide Vanes and Variable Speed in Process Multistage Centrifugal Compressors. J Eng Gas Turbine Power 2014;136. https://doi.org/10.1115/1.4026621.

[52] SERO Pumps. SRZS Performance Curves. SeropumpsCom 2025.

[53] Goodrich M. A pump seal selection guideline complementing ISO 21049/API 682. Sealing Technology 2010;2010:8–12. https://doi.org/10.1016/S1350-4789(10)70350-0.

[54] Platt B, Young D, Bandhauer T. Thermodynamic and turbomachinery analysis of a hybrid electric organic Rankine vapor compression system. Appl Energy 2025;387:125554. https://doi.org/10.1016/j.apenergy.2025.125554.

[55] Klein SA. Engineering equation solver. F-Chart Software 2020.

[56] Air-Conditioning H& RI. Performance Rating of Water-chilling and Heat Pump Water-heating Packages Using the Vapor Compression Cycle. 2023.

[57] Air-Conditioning H& RI. 2000 Standard for Absorption Water Chilling and Water Heating Packages. 2000.

[58] Melinder A. Properties of Secondary Working Fluids (Secondary Refrigerants or Coolants, Heat Transfer Fluids) for Indirect Systems. 2nd ed. IIF-IIR - France; 2010.

[59] Akasaka R. New Fundamental Equations of State with a Common Functional Form for 2,3,3,3-Tetrafluoropropene (R-1234yf) and trans-1,3,3,3-Tetrafluoropropene (R1234ze(E)). Int J Thermophys 2011;32:1125–47.

[60] Semlitsch B, Mihăescu M. Flow phenomena leading to surge in a centrifugal compressor. Energy 2016;103:572–87. https://doi.org/10.1016/j.energy.2016.03.032.

[61] Day IJ. Stall, surge, and 75 years of research. J Turbomach 2016;138. https://doi.org/10.1115/1.4031473.

[62] Cravero C, Marsano D. Instability Phenomena in Centrifugal Compressors and Strategies to Extend the Operating Range: A Review. Energies (Basel) 2024;17. https://doi.org/10.3390/en17051069.

[63] Toussaint M, Boudfar M, Podevin P, Descombes *-Georges. Influence of the upstream circuit on the surge characteristics of centrifugal compressors. ACTA TECHNICA NAPOCENSIS INFLUENCE OF THE UPSTREAMS CIRCUIT ON THE SURGE CHARACTERISTICS OF CENTRIFUGAL COMPRESSORS. vol. 50. 2007.

[64] Tavakoli S, Griffin I, Fleming P. An Overview of Compressor Instabilities: Basic Concepts and Control. IFAC Proceedings Volumes 2004;37:523–8. https://doi.org/10.1016/S1474-6670(17)32228-0.

[65] Wright T, Gerhart PM. Fluid Machinery: Application, Selection, and Design. 2nd ed. Taylor & Francis Group; 2009.

[66] Kurz R, Marechale RK, Fowler EJ, Ji M, Cave MJ. OPERATION OF CENTRIFUGAL COMPRESSORS IN CHOKE CONDITIONS, Singapore: Asia Turbomachinery and Pump Symposium; 2016.

[67] Noall J, Forsha M. Off-Design Turbomachinery Performance Mapping. vol. 80002. 2008.

[68] Platt B, Young D, Bandhauer T. Experimental Validation of a Hybrid Electric Organic Rankine Vapor Compression Cooling System [Under Review]. Appl Energy 2025.

[69] Lemmon EW, Bell IH, Huber ML, McLinden MO. NIST Standard Reference Database 23: Reference Fluid Thermodynamic and Transport Properties-REFPROP 2018.

[70] Thol M, Lemmon EW. Equation of State for the Thermodynamic Properties of trans-1,3,3,3-Tetrafluoropropene [R-1234ze(E)]. Int J Thermophys 2016;37:28. https://doi.org/10.1007/s10765-016-2040-6.

[71] Ding Y, Li B, Yao R, Tan Y. Part load operation coefficient of air-conditioning system of public building. Energy Build 2010;42:1902–7. https://doi.org/10.1016/J.ENBUILD.2010.05.026.

[72] Zhou Z, Liu P, Li Z, Pistikopoulos EN, Georgiadis MC. Impacts of equipment off-design characteristics on the optimal design and operation of combined cooling, heating and power systems. Comput Chem Eng 2013;48:40–7. https://doi.org/10.1016/j.compchemeng.2012.08.007.

[73] American Society of Mechanical Engineers. PTC 19.1 - Test Uncertainty. ASME; 2018.

APPENDIX A. Heat Exchanger Performance Data

Table A-1 presents representative performance data for the heat exchange equipment in the hybrid ORVC test facility. Heat duty is calculated from external streams where possible and from the refrigerant stream if the device did not interface with an external stream. Pressure drop in the refrigerant stream is provided for each device (hot and cold refrigerant streams for the recuperative heat exchangers). Inlet and outlet temperatures on both sides of each device are also included. Pressure drop across the evaporator could not be measured independently of the spray nozzles due to the integrated design of the evaporator and is, therefore, not reported in Table A-1.

Table A-1: Representative heat exchanger performance data from design point testing with 257 kW of heat input.

Device	*Heat Duty [kW]*	*Working Fluid*	*Pressure Drop*	*Temperatures [C]*			
				Hot Side Inlet	*Hot Side Outlet*	*Cold Side Inlet*	*Cold Side Outlet*
Boiler	256.5	R1234ze(E) / EG	30.4	90.7	87.6	62.4	90.4
PC Condenser	269.0	R1234ze(E) / EG	10.9	35.8	31.7	29.9	33.4
Evaporator	176.1	R1234ze(E) / EG	-	14.2	9.0	6.0	6.5
CC Condenser	193.6	R1234ze(E) / EG	12.9	58.0	35.4	30.1	35.7
Recuperator	57.6	R1234ze(E) / R1234ze(E)	2.9 (cold) 2.2 (hot)	69.2	36.1	34.0	56.8
Economizer	15.2	R1234ze(E) / R1234ze(E)	3.1 (cold) 7.8 (hot)	71.6	58.3	56.8	62.5
SLHX	27.4	R1234ze(E) / R1234ze(E)	6.4 (cold) 12.2 (hot)	34.7	33.5	6.5	34.4

APPENDIX B. Instrumentation Details

The test facility was extensively instrumented to collect high fidelity performance data from the experiments performed in this research. Table B-1 presents instrument types, locations, units and bias errors for each measurement channel utilized for data acquisition. Bias errors are representative values from the design point experiment with 257 kW of heat input.

Table B-1: Details of the instrumentation used on the test facility including instrument type, location, units and bias error.

Channel	*Instrument Type*	*Location*	*Units*	*Bias Error*
CH 02-00	Pressure	Boiler Inlet (r)	kPa	8.25
CH 02-01	Pressure	Turbine Inlet	kPa	8.50
CH 02-02	Pressure	Turbine Outlet	kPa	2.70
CH 02-03	Pressure	PC Condenser Inlet (r)	kPa	2.54
CH 02-04	Pressure	Pump Inlet	kPa	2.95
CH 02-05	Pressure	Pump Outlet	kPa	7.97
CH 02-06	Pressure	TC Compressor Inlet	kPa	2.13
CH 02-07	Pressure	TC Compressor Outlet	kPa	2.61
CH 02-08	Pressure	CC Condenser Inlet (r)	kPa	2.78
CH 02-09	Pressure	EXP Valve Inlet	kPa	2.64
CH 02-10	Pressure	Evaporator Inlet (r)	kPa	1.97
CH 02-11	Pressure	Evaporator Outlet (r)	kPa	1.99
CH 02-12	Pressure	Boiler Inlet (eg)	kPa	1.97
CH 02-13	Pressure	PC Condenser Inlet (eg)	kPa	1.99
CH 02-14	Pressure	CC Condenser Inlet (eg)	kPa	1.92
CH 02-15	Pressure	Condenser Pump Inlet	kPa	1.92
CH 02-16	Pressure	Condenser Pump Outlet	kPa	1.89
CH 02-17	Pressure	Evaporator Inlet (eg)	kPa	1.96
CH 02-18	Pressure	Basement HX Inlet (eg)	kPa	2.04
CH 02-19	Pressure	Basement HX Inlet (pg)	kPa	1.98
CH 02-20	Pressure	XC Pump Outlet	kPa	7.64
CH 02-23	Pressure	XC Pump Inlet	kPa	2.81
CH 02-24	Pressure	Recuperator Inlet (liquid)	kPa	8.72
CH 02-25	Pressure	Economizer Outlet (liquid)	kPa	8.28
CH 02-26	Pressure	Recuperator Inlet (vapor)	kPa	2.99
CH 02-27	Pressure	SLHX Inlet (liquid)	kPa	2.69
Ch 03-01	Differential Pressure	PC Condenser (r)	kPa	0.12

CH 03-02	Differential Pressure	Economizer Vapor	kPa	0.12
CH 03-03	Differential Pressure	CC Condenser (r)	kPa	0.12
CH 03-04	Differential Pressure	Boiler (eg)	kPa	0.12
CH 03-05	Differential Pressure	PC Condenser (eg)	kPa	0.61
CH 03-06	Differential Pressure	Evaporator (eg)	kPa	0.61
CH 03-07	Pressure	CC Condenser Outlet (r)	kPa	10.3
CH 03-08	Volume Flow	CC Condenser (eg)	GPM	1.43
CH 03-09	Volume Flow	Condenser Loop (eg)	GPM	4.69
CH 03-10	Volume Flow	Boiler Loop (eg)	GPM	3.64
CH 03-11	Volume Flow	Evaporator Loop (eg)	GPM	1.32
CH 03-13	Volume Flow	XC Pump	GPM	0.00
CH 03-14	Mass Flow	Cooling Cycle	kg/s	0.00
CH 03-15	Mass Flow	Power Cycle	kg/s	0.00
CH 03-17	Volume Flow	TC Liquid Drain	GPM	0.04
CH 03-18	Volume Flow	Basement HX (pg)	GPM	0.19
CH 03-19	Differential Pressure	Recuperator Liquid	kPa	0.12
CH 03-20	Differential Pressure	Evaporator (r)	kPa	0.12
CH 03-21	Differential Pressure	SLHX Liquid	kPa	0.12
CH 03-22	Differential Pressure	Recuperator Vapor	kPa	0.12
CH 03-23	Differential Pressure	CC Condenser (eg)	kPa	0.61
CH 03-24	Differential Pressure	Boiler (r)	kPa	0.12
CH 03-25	Differential Pressure	Economizer Liquid	kPa	0.12
CH 03-27	Differential Pressure	SLHX Vapor	kPa	0.12
CH 03-28	Differential Pressure	Basement HX (eg)	kPa	0.61
CH 03-29	Differential Pressure	Basement HX (pg)	kPa	0.12
CH 03-31	Differential Pressure	Orifice Plate	kPa	0.17
CH 04-03	Pressure	Ambient Air	kPa	0.50
CH 04-04	Electric Power	PC Pump	kW	0.05
CH 04-05	Electric Power	XC Pump	kW	0.001
CH 04-11	Pressure	Electric Compressor Outlet	kPa	2.90
CH 04-12	Pressure	Electric Compressor Inlet	kPa	2.34
CH 04-13	Differential Pressure	CC Orifice Plate	kPa	13.8
TC 01-00	Temperature	Boiler Inlet (r)	C	0.18
TC 01-01	Temperature	Boiler Outlet (r)	C	0.15
TC 01-02	Temperature	Turbine Inlet	C	0.23
TC 01-03	Temperature	Turbine Outlet	C	0.13
TC 01-04	Temperature	PC Condenser Inlet (r)	C	0.20
TC 01-05	Temperature	PC Condenser Outlet (r)	C	0.21
TC 01-06	Temperature	PC Pump Inlet	C	0.23
TC 01-07	Temperature	PC Pump Outlet	C	0.23
TC 01-08	Temperature	TC Compressor Inlet	C	0.17
TC 01-09	Temperature	TC Compressor Outlet	C	0.20
TC 01-10	Temperature	CC Condenser Inlet (r)	C	0.21

TC 01-11	Temperature	XC Pump Outlet	C	0.19
TC 01-12	Temperature	Condenser Pump Inlet	C	0.06
TC 01-13	Temperature	EXP Valve Inlet	C	0.18
TC 01-14	Temperature	Evaporator Inlet (r)	C	0.15
TC 01-15	Temperature	Evaporator Outlet (r)	C	0.18
TC 02-00	Temperature	Boiler Inlet (eg)	C	0.07
TC 02-01	Temperature	Boiler Outlet (eg)	C	0.07
TC 02-02	Temperature	PC Pump Cavity	C	0.22
TC 02-03	Temperature	CC Condenser Outlet (eg)	C	0.04
TC 02-04	Temperature	Orifice Plate Inlet	C	0.23
TC 02-05	Temperature	CC Condenser Inlet (eg)	C	0.05
TC 02-06	Temperature	Evaporator Inlet (eg)	C	0.19
TC 02-07	Temperature	Evaporator Outlet (eg)	C	0.18
TC 02-08	Temperature	Basement HX Inlet (eg)	C	0.02
TC 02-09	Temperature	Basement HX Outlet (eg)	C	0.02
TC 02-10	Temperature	Basement HX Inlet (pg)	C	0.09
TC 02-11	Temperature	Basement HX Outlet (pg)	C	0.09
TC 02-12	Temperature	PC Condenser Inlet (eg)	C	0.06
TC 02-13	Temperature	PC Condenser Outlet (eg)	C	0.06
TC 02-14	Temperature	XC Pump Inlet	C	0.24
TC 02-15	Temperature	TC Cavity	C	0.06
TC 03-00	Temperature	Ambient Outdoor	C	1.00
TC 03-01	Temperature	Boiler Loop Heater Outlet	C	0.06
TC 03-02	Temperature	Recuperator Vapor Balance	C	0.17
TC 03-03	Temperature	Recuperator Inlet (vapor)	C	0.13
TC 03-04	Temperature	Recuperator Outlet (vapor)	C	0.16
TC 03-05	Temperature	Recuperator Inlet (liquid)	C	0.20
TC 03-06	Temperature	Condenser Pump Outlet	C	0.04
TC 03-07	Temperature	CC Condenser Outlet (r)	C	0.20
TC 03-08	Temperature	Economizer Outlet (vapor)	C	0.14
TC 03-09	Temperature	Economizer Outlet (liquid)	C	0.16
TC 03-10	Temperature	Recuperator Outlet (liquid)	C	0.16
TC 03-11	Temperature	Economizer Inlet (vapor)	C	0.14
TC 03-12	Temperature	SLHX Outlet (vapor)	C	0.16
TC 03-13	Temperature	SLHX Vapor Balance	C	0.17
TC 03-14	Temperature	SLHX Inlet (liquid)	C	0.17
TC 03-15	Temperature	SLHX Outlet (liquid)	C	0.32
TC 04-00	Temperature	Electric Compressor Inlet	C	0.15
TC 04-01	Temperature	Electric Compressor Outlet	C	0.21
EC 01-00	Electric Power	Electric Compressor	kW	0.51

Test data uncertainty was quantified using the standardized procedure in the 2018 American Society of Mechanical Engineers Performance Test Code 19.1 [73]. Instrument bias error and random error were utilized to quantify the total error for each measurement. Full uncertainty propagation was performed in Engineering Equation Solver to streamline the process across the significant amount of data collected for each test [55]. Full uncertainty propagation was conducted for each of the design point hybrid cooling experiments described in Chapter 5.